Master's Thesis

The Fabrication of High Energy Flexible Lithium-ion Batteries via Electrode Design

Yoonji Lee

Department of Energy Engineering

(Battery Science and Technology)

Graduate School of UNIST

2018

The Fabrication of High Energy Flexible Lithium-ion Batteries via Electrode Design

Yoonji Lee

Department of Energy Engineering
(Battery Science and Technology)

Graduate School of UNIST

The Fabrication of High Energy Flexible Lithium-ion Batteries via Electrode Design

A thesis
submitted to the Graduate School of UNIST
in partial fulfillment of the
requirements for the degree of
Master of Science

Yoonji Lee

12. 21. 2017
Approved by

조재필

Advisor
Jaephil Cho

The Fabrication of High Energy Flexible Lithium-ion Batteries via Electrode Design

Yoonji Lee

This certifies that the thesis of Yoonji Lee is approved.

12. 21. 2017

Advisor: Jaephil Cho

Kyeong-Min Jeong

Nam-Soon Choi

Abstract

With the advent of flexible electronics, lithium-ion batteries have become a key component of high performance energy storage systems. Thus, considerable effort has been made to keep pace with the development of flexible lithium-ion batteries. To date, many researchers have studied newly designed batteries with flexibility, however, there are several significant challenges needed to be overcome, such as degradation of electrodes under external load, poor battery performance and complicated cell preparation procedures. In addition, in-depth understanding of the current challenges for flexible batteries has been rarely addressed in systematical and practical way. Herein, we review recent progress and current issues for the flexible lithium-ion batteries in terms of battery materials and cell designs. We also provide a critical overview of important issues and challenges for the practical application of flexible lithium-ion batteries. Finally, we discuss the strategies to overcome current limitations towards the practical use of flexible lithium-based batteries, providing the future research directions.

Contents

List of Figures

deformability. (g) Schematic of a node-type LIB. (h) Cycle performance of full cells with LCO cathode and graphite anode at a current density of 1C under intermittent flexing 1000 times per 20 charge/discharge cycles, where the operating voltage ranged from 3.0 to 4.3 V. (i) Photograph of the node-type cell illuminating blue LEDs under the deformed state.

Figure 7. (a) A discharge voltage of a full cell with LTO anode and LFP cathode at a C-rate of C/5 when the cell was repeatedly folded. (b) Photograph of the LFP and LTO electrodes after in-situ folding test. (c) The SEM image of the cross-section for LFP electrode. (d) Schematic of bending state of conventional LIBs. Voltage profiles of the reassembled (e) non-bent and (f) bent site of the full cell after bending 5000 times, where the operating voltage is range was 3.0−4.3 V. SEM image of the (g) non-bent and (h) bent site of graphite electrodes.

Figure 8. (a) Schematic of fabricating electrodes using CNTs. (b) Cross-section SEM image of the LCO/CNT electrode. (c) Cycle performance of the full cell with LTO anode and LCO cathode at C-rate of C/2 under intermittent 100 flexing between 20 cycles, where the operating voltage ranged from 1.6 to 2.6 V.

Figure 9. SEM image of a) pristine nickel mesh (40-sized mesh), and b) flattened nickel mesh as a template.

Figure 10. a) SEM image of pre-patterned Al foil, and b) its surface morphology showing electrode materials coated onto pre-patterned Al foil. c) SEM image of pre-patterned Cu foil, and d) its surface morphology showing electrode materials coated onto pre-patterned Cu foil.

Figure 11. Digital photograph of a) post-patterned anode and cathode electrodes the size of 13 mm × 45 mm cathode and 15mm × 50mm anode, b) nickel strap welded with post-patterned anodes, c) aluminum strap welded with post-patterned cathodes. d−f) Prepared node-type cells with 1, 3, and 6 nodes.

Figure 12. Preparation of a) pre-patterned, showing digital photograph of pre-patterned Al- and Cu-foil, and b) post-patterned electrode, showing post-patterned cathode and anode electrodes.

Figure 13. Post-patterning process and microstructure of a graphite anode electrode. (a) Schematic of the fabrication process for the post-patterned electrode. After finishing a conventional electrode manufacturing process (slurry coating and pressing), an additional process is performed by patterning electrode using a 40-sized mesh template. (b) SEM image of a surface morphology of the post-patterned anode electrode, showing selectively-pressed grid pattern (indicating white arrow), and (c) its cross-section, where red arrows indicate the pressed region. (d) Magnified top-view of the post-patterned anode, showing a distinctive boundary of pressed graphite-anode materials.

Figure 14. a) SEM image of pristine Al foil, and it surface morphology showing $LiCoO_2$-cathode active materials with its magnified image. b) SEM image of pristine Cu foil, and it surface morphology showing natural graphite-anode active materials with its magnified image.

Figure 15. a) SEM image of a surface morphology of the post-patterned cathode electrode, showing

selectively-pressed grid pattern (indicating white arrow), and b) its cross-section, where red arrows indicate the pressed region. (c) Magnified top-view of the post-patterned cathode, showing a distinctive boundary of pressed active materials (LCO).

Figure 16. a) SEM image of a cross-section view showing a morphology of the post-patterned anode electrode. b) SEM image of a cross-section view showing a morphology of the post-patterned cathode electrode. c) Schematic of post-patterning process, explaining that active materials can be moved by post-patterning process.

Figure 17. Adhesion force measurements and electrochemical tests. Schematic of 180° peel test applied to (a) no pattern and (b) post-patterned electrodes at a rate of 50 mm min^{-1}. Adhesion force curves for (c) graphite anode and (d) LCO cathode without and with the post-patterning process. Cycle performance of (e) anode and (f) cathode without and with post-pattern, showing discharge capacity retentions reported from 1 to 50 cycles at 0.5C rate. Insets shows the rate capabilities at different C-rates from 0.2 to 2C.

Figure 18. Digital photograph showing adhesion test, where 3M tape was applied onto electrode surface, and it was pulled away from the electrode at 180° to the surface with a speed of 50 mm min^{-1}.

Figure 19. Adhesion force curves for a) pre-patterned graphite anode and (b) pre-patterned LCO cathode.

Figure 20. Digital photographs including no pattern, pre-patterned, and post-patterned a) anode and b) cathode electrodes after adhesion test, where a magnified image represents the peeled-off electrode with unique grid patterns remained on adhesive tape.

Figure 21. a) Ultimate tensile strength of no pattern, pre-patterned, and post-patterned anode and cathode electrodes, and digital photographs of b) anode and c) electrode after the test.

Figure 22. Voltage profiles of no pattern, pre-patterned, and post-patterned a) anode and b) cathode electrodes at a current rate of 0.5C.

Figure 23. Cycle performance of the pre-patterned (a) cathode and (b) anode, showing discharge capacity retentions reported from 1 to 50 cycles at 0.5C rate. Insets shows the rate capabilities at different C-rates from 0.2 to 2C.

Figure 24. Node-type cell assembly and full-cell performance. (a) Schematic of the node-type LIBs components, showing digital photographs of the post-patterned LCO and graphite electrodes, respectively, and (b) cell-assembly process, showing that each planar electrode can be wound and packaged as a node cell. (c, d) Voltage profiles of the node-type cell with and without post-patterned electrodes at different rates from 0.5 to 5C. (e) Rate capability of the node-type cell with and without post-patterned electrodes, showing charge capacity retention at different rates from 0.5C to 5C, and (f) their long-term stability test over 200 cycles at a rate of 1C.

Figure 25. . a) Voltage profiles of the node-type cell with and without post-patterned electrodes during the first cycle at 0.5C rate.

Figure 26. Plot of the voltage vs C-rate for no-pattern node a) before cycling and b) after 150 cycles. Plot of the voltage vs C-rate for post-patterned node a) before cycling and b) after 150 cycles. Pulse current was applied as increasing the current rate from 0.5C to 2.5C at state of charge (SOC) of 50 %, and pulse duration was10 seconds.

Figure 27. Node-type cell disassembly and finite element analysis (FEA). Schematic of the deformed electrodes of (a) no pattern and (b) post-patterned electrodes, showing their SEM image of the LCO and graphite coating layer after 200 cycles. Disassembled no-pattern node cell after fully charged to 4.35 V, showing (c) anode, (d) cathode, and (e) separator, respectively. Disassembled post-pattern node cell after fully charged to 4.35 V, showing (f) anode, (g) cathode, and (h) separator, respectively. (i, j) FEA results representing the deformation and von Mises stress distribution, where the photographs show the target symmetry without and with post-patterning, respectively.

Figure 28 Application of the node-type LIBs. (a) Voltage profiles of the node-type LIBs with the different number of node from 1 to 6. (b) Effect of the post-patterning on high loading level electrodes with cathode and anode loading level of ~18.0 and ~8.0 mg cm^{-2}, respectively, showing linear capacity and its Coulombic efficiency (CE) for 100 cycles. (c) Photographs of a flexing test with powering blue light-emitting diodes (LEDs). (d) Comparison of discharge capacity retention in unstressed and flexing conditions, where the cell was flexed 1,000 times per 20 cycles. Photograph of the flexible node-type LIBs under different deformable conditions, (e) lighting up a blue LED panel in zig-zag state, (f) wearing on the wrist maintaining open circuit voltage (OCV) of ca. 3.7 V, and (g) embedding it on each joint in the robotic hand.

Figure 29. Cycle performance of a) 3-nodes and b) 6-nodes battery, showing discharge capacity and Coulombic efficiency for 100 cycles at 1C rate.

Figure 30. a) Process of calculating a volume of node cell, where the node was simply divided into two sections of A and B. We assumed that height (H) and length (L) of node were 0.33 and 1.5 cm, respectively, and the width of section A was 0.6 cm. The rest of the parts, section B, was calculated by assuming an elliptical boundary. **b**) Cycle performance representing volumetric discharge capacity of the post-pattern node with cathode and anode loading level of ~18.0 and ~8.0 mg cm^{-2}, respectively.

Figure 31. Scanning electron microscopy (SEM) images of a) pristine nickel mesh (40-sized mesh), and b) a flattened nickel mesh as a template.

Figure 32. Schematic of the fabrication process for the *Lego-like* 3D block cell.

Figure 33. a) A conceptual illustration of the *Lego-like* 3D block battery showing the characteristics of their configuration. Digital photographs of the b) 3D block cell and c) its major components. The scanning electron microscopy (SEM) images of the selectively pressed d) cathode, e) anode and f) separator after patterning process. The graphite anode and LiCoO2 cathode showed oppositely pressed grid patterns.

Figure 34. SEM image of a surface morphology of a) non pressed cathode, b) intensively pressed

after 5000 flexing cycles with a flexing radius of 15 mm. d) Lighting up three white lighting-emitting diodes (LEDs) worn on the wrist. e-f) Voltage output of flexible 3D block battery under different flexing radius of 25, 15, 8 mm, flat conditions.

Figure 47. Requirements and considerations for practical application of flexible batteries.

List of Tables

Chapter 1

Introduction

1.1 Principle of lithium-ion batteries

Lithium-ion batteries were firstly developed and commercialized by Sony in 1991. Lithium-ion batteries (LIBs) have been widely accepted as power sources for their application in portable electronic devices, owing to their high energy density. The four major components of conventional LIBs are a positive (cathode) electrodes, negative (anode) electrodes, separator which only allows Li^+ ions but prevents direct contact between electrodes and inorganic electrolytes that allows ion transfer between electrodes. Intercalated lithium compounds used as cathode materials for LIBs such as lithium cobalt oxide ($LiCoO_2$) and lithium nickel manganese cobalt oxide ($LiNiCoMnO_2$ or NCM). Anode materials are commonly consist of carbonaceous material such as Graphite.

The working principle of LIBs involves oxidation-reduction reaction. As shown in Figure 1, lithium ions intercalate from the positive electrode (“cathode”) to the negative electrode (“anode”) during charge process and back when discharging.[1-2]

Cathode $\quad LiCoO_2 \leftrightharpoons Li_{1-x}CoO_2 + xLi^+ + xe^-$

Anode $\quad C_n + xLi^+ + xe^- \leftrightharpoons C_nLi_x$

Overall reaction $\quad LiCoO_2 + C_n \leftrightharpoons Li_{1-x}CoO_2 + C_nLi_x$

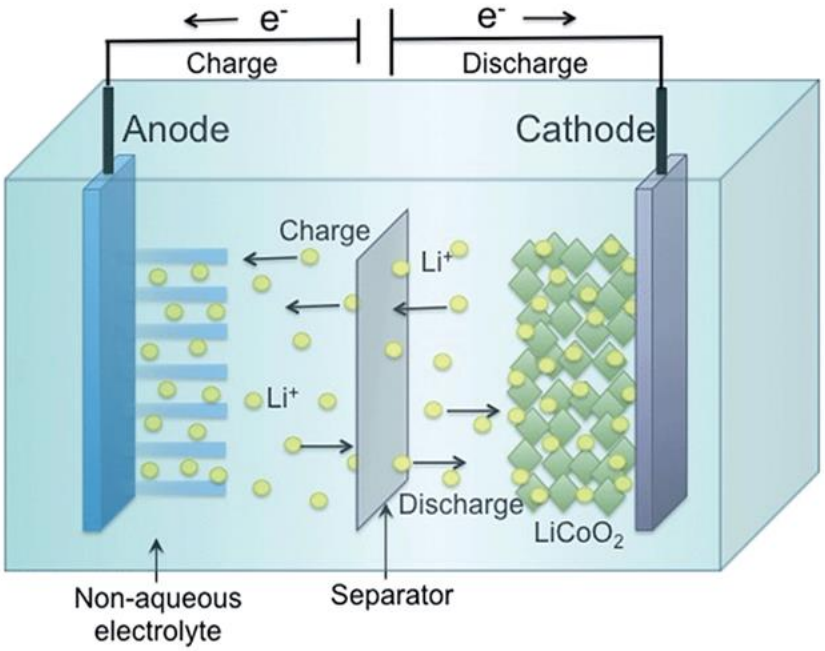

Figure 1. Schematic illustration of conventional lithium-ion batteries.[3]

1.2 Flexible lithium-ion batteries

An ever-growing interest and demand for flexible electronics have led to the development of flexible, light-weight energy storage systems.[4-6] Among them, rechargeable lithium-ion batteries (LIBs) have received great attention for flexible batteries because of their high volumetric energy density and long cycle life.[7-8] However, components of current LIBs such as active materials, metal foil current collector and cell packages, have several limitations for the flexible electronics because of their intrinsic rigid property. When a cell was flexed, traditional active materials such as LiCoO2 (LCO), LiFePO4 (LFP), graphite or Li4Ti5O12 (LTO) can be delaminated from the metal foil current collector, generating cracks on the electrode surface.[9] This eventually causes particle isolation and increases internal cell resistance.

Figure 2. Diverse applications of flexible energy storage systems. Reproduced with permission.[10] Copy right 2016, Wiley−VCH.

To overcome these problems, there are two distinct approaches for the development of flexible LIBs: the improvement of mechanical strength between electrode materials by new materials and the design of novel cell configurations. With respect to the first approach, many researchers have investigated flexible electrode materials for the replacement of the rigid cell components.[11] Accordingly, the conductive materials, such as carbon nanotubes (CNTs),[12] carbon textiles[10] or graphene derivatives,[13] have been used as current collectors because of their superior electronic conductivity and high flexibility. In addition, polymeric substrates including polydimethylsiloxane (PDMS) or cellulose showed enhanced binding property with electrode materials, resulting in high elastic property of the electrodes.[14] Recently, significant improvement has been achieved in the field of free-standing electrodes by using abovementioned materials.[15-17] This structure has accomplished high flexibility without showing contact loss between current collector and electrode coating. Furthermore, the stress concentration on the electrode upon flexing can be mitigated by designing new cell structures. For example, there are a wide range of flexible cell configurations, such as coplanar,[18] cable [19-21]or node-type.[22] These unique architectures can accommodate high deformable states, maintaining their electrochemical performance.

However, many challenges still remain towards practical application of the flexible LIBs as follows: the degradation of the cell under deformation, limited battery performance compared with commercial standards of LIBs and complex cell manufacturing process. To date, there have been many review articles providing the excellent summaries of research trends for the LIBs. However, most previous published review articles have mainly focused on the structural deformability or novel designs of active materials or cells.[23-25] Thus, the critical review of the flexible LIBs is urgently needed in terms of the practical application.

In this Review, we discuss recent progress in the development of flexible LIBs with respect to the material and cell structure designs. Furthermore, we highlight the issues associated with the practical application for the flexible lithium-based batteries regarding the performance and fabrication process. In the final section, we provide the strategies to realize the practical use of flexible lithium-based batteries, presenting a realistic outlook.

1.2.1 Design of flexible electrode materials

In general, the electrodes of the LIBs are composed of active materials, current collectors, conducting agents and polymer binders. Among them, the amount of conducting agents and polymer binder are negligible; thus, the research approaches for flexible LIBs have mainly been focusing on the development of flexible active materials and current collectors. With respect to volumetric energy density, spherical micron-sized active materials are commonly used in the conventional LIBs because they have high electrode packing density. However, when the cells were twisted, stretched or bent, the

contact between electrode materials can be deteriorated with poor electrochemical performance. Thus, several modifications of the active materials have been developed to mitigate the contact loss of electrode materials.

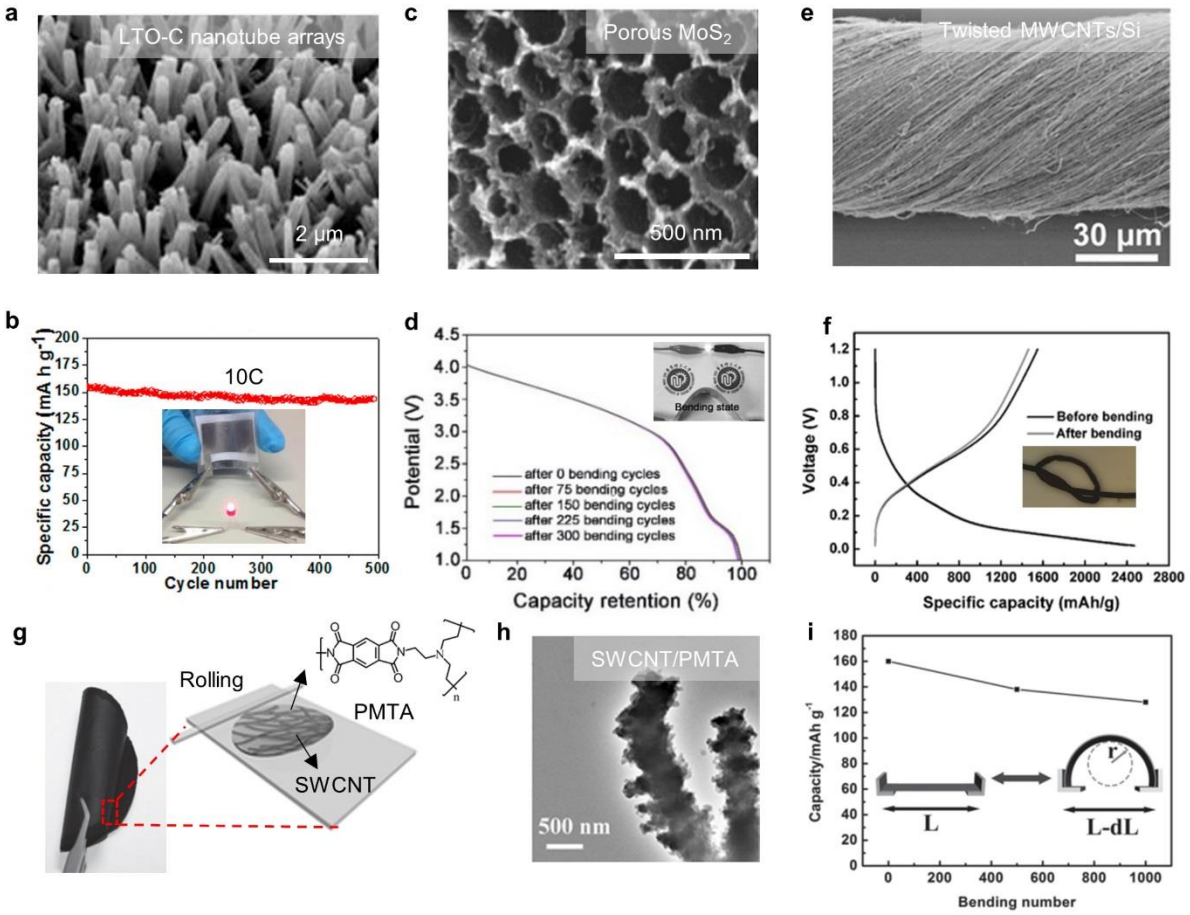

Figure 3. (a) SEM image of the LTO-C nanotube arrays. (b) Cycle performance of the nanostructure LTO-C anode at a discharge rate of 10C, where the operating voltage range was 1.0−3.0 V. Part a and b are reproduced with permission.[26] Copy right 2014, American Chemical Society. (c) SEM image of the porous MoS2. (d) Capacity retention of full cell with porous MoS2 anode and LCO cathode after bending 0 to 300 cycles, where the operating voltage ranged from 1.0 to 4.2 V. Part c and d are reproduced with permission.[27] Copy right 2017, Wiley−VCH. (e) SEM image of the twisted MWCNTs/Si electrode. (f) Voltage profiles of MWCNT/Si composite before and after 100 cycles bending at a current density of 2 A g^{-1}, where the operating voltage range was 0.02−1.2 V. Part e and f are reproduced with permission.[21] Copy right 2014, Wiley−VCH. (g) Schematic of fabrication process of PMTA/SWCNT electrode on the SWCNT film and the photograph of the electrode. (h) TEM image of the PMTA/SWCNT composite. (i) Capacity retention of the PMTA/SWCNT electrode at a discharge rate of 0.1C after bent 500 and 1000 times. Part g and i are reproduced with permission.[28] Copy right 2015, Wiley−VCH.

Recently, a variety of electrode morphologies such as nanostructure,[29-30] porous structure,[14, 27, 31] and twisted structure[20-21, 32] have been reported to reduce the stress of cells upon flexing. Yu et al. reported self-supported LTO nanotube arrays as anode materials.[26] It was synthesized by the growth of LTO nanotube arrays on a Ti foil, followed by a carbon layer coating. Scanning electron microscopy (SEM) image shows the well-aligned LTO-C nanotube arrays (Figure 3a). The highly conductive LTO nanotube array with hollow structure could facilitate the transportation of lithium ions, demonstrating capacity retention of ~93% after 500 cycles, at high C-rate of 10C with LCO cathode (Figure 3b). The assembled full cell illuminated LEDs under the bent states. In comparison to the traditional spherical particles, the morphology of long nanotube arrays efficiently dispersed the strain under the external load without contact loss of active materials.

The other approach for flexible LIBs is to design three dimensional (3D) ordered porous structure of active materials. Li et al. reported the porous MoS2 (3DOM MoS_2) electrode by introducing polystyrene nanospheres as a pore formation template.[27] The prepared MoS_2 electrode showed a pore size of ~200 nm (Figure 3c). The interconnected porous structure increased mechanical strength, illuminating LEDs after 300 flexing cycles. For comparison, they prepared the 3DOM MoS2 electrode and MoS2 electrode with conventional electrode coating process, and the cells were placed on 300 bending cycles. The 3DOM MoS_2 electrode retained ~100% of the initial discharge capacity, and the electrode was well-maintained after bending test (Figure 3d). However, the pristine MoS_2 electrode could not endure the stress from flexing, resulting in the detachment of the active material from the current collector with severe capacity fading. These results were ascribed to the increased adhesion force between macroporous MoS2 active materials and current collectors, providing high mechanical strength of the electrode. In addition, the twisted morphology of active materials could enhance the flexibility of the LIBs due to its unique deformable construction. Peng et al. fabricated the twisted electrode by the deposition of silicon particles on the individual multiwalled carbon nanotubes (MWCNTs), followed by a twisting treatment (Figure 3e).[21] The well aligned MWCNTs/silicon electrode could form different knot structure, and maintained discharge capacity of ~1460 mAh g^{-1} after 100 flexing cycles (Figure 3f).

The polymer derivatives can be good alternative active materials for flexible batteries because of their intrinsic flexible property. Recently, the composite of polymers with conducting agents as an active material has been developed as a flexible polymer cathode.[28, 33] Figure 3g shows the composite of polyimide derivatives (PMTA) as an active material and single-walled carbon nanotube (SWCNT) as a conductive agent, which was synthesized by a simple rolling method.[28] The transmission electron microscopy (TEM) image of the PMTA/SWCNT composite shows that PMTA particles are adhered to the SWCNT bundles (Figure 3h). The initial discharge capacity was ~160 mAh g^{-1} and the flexibility of the electrode was demonstrated for 1000 flexing cycles (Figure 3i). Notably, the polymer electrode

retained ~80% of initial discharge capacity upon flexing. The polymeric property of the PMTA could increase the flexibility of the electrodes and the SWCNT network enhanced the mechanical strengths.

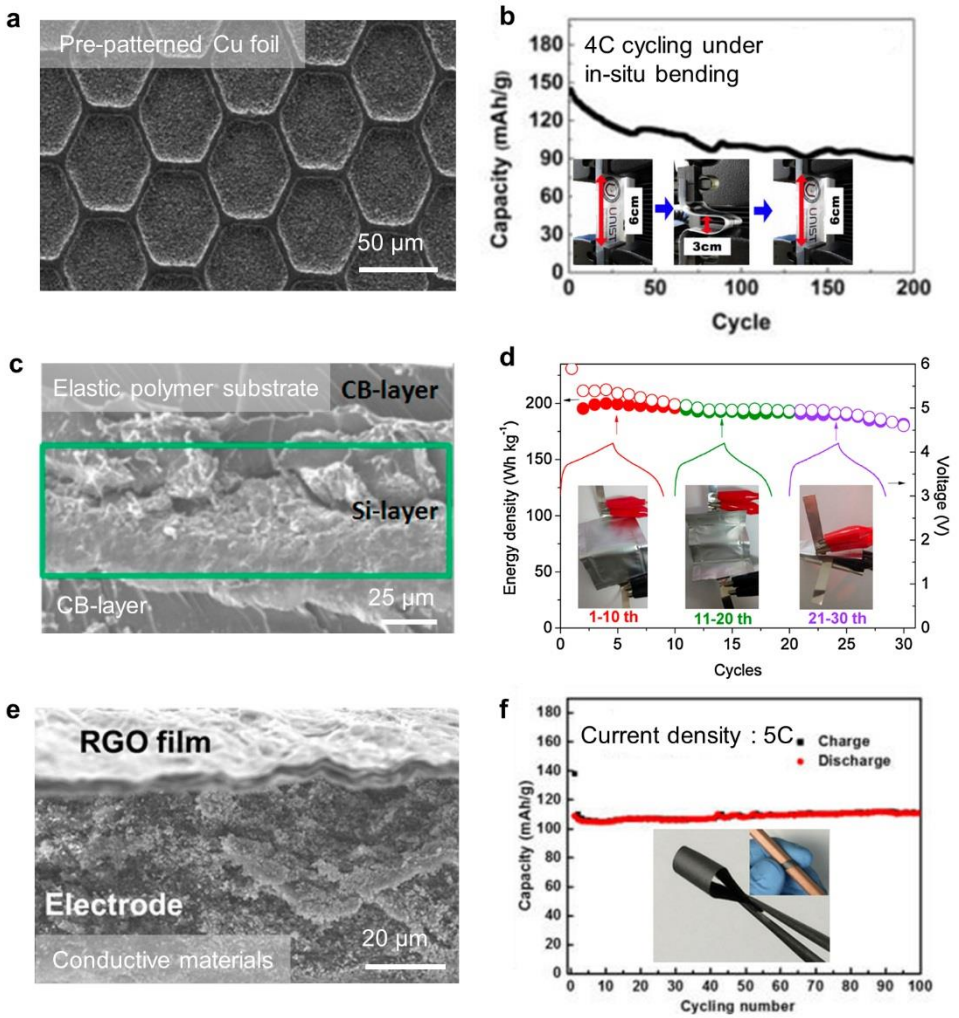

Figure 4. (a) SEM image of pre-patterned Cu foil. (b) Cycle performance of the full cell with pre-patterned VNCM cathode and PNG-AES anode at a discharge rate of 4C under in-situ bending, where the operating voltage range was 3.0−4.3 V. Part a and b are reproduced with permission.[34] Copy right 2014, American Chemical Society. (c) SEM image of the cross section for CB/Si/CB electrode. (d) Cycle performance of the full cell with pre-patterned LCO/CB cathode and CB/Si/CB anode under different folding states, where the operating voltage ranged from 2.9 to 4.2 V. Part c and d are reproduced with permission.[35] Copy right 2017, Elsevier. (e) SEM image of the cross section for RGO/LFP electrode. (f) Cycle performance of the RGO/LFP electrode at a discharge rate of 5C, where the operating voltage range was 2.0−4.5 V. Part e and f are reproduced with permission.[36] Copy right 2016, American Chemical Society.

Current electrodes for the commercial LIBs have been fabricated by a slurry coating method on metal current collectors. The metal foils are commonly used as current collectors due to high electrical conductivity, and they contribute the electron transfer between active materials and external power sources. However, when the cell was deformed, the rigid metal foils usually cause the delamination of active materials. To address this issue, many studies have been reported to improve the flexibility of the conventional metal current collectors. For example, the use of patterned current collectors can enhance the adhesion force between active materials and current collectors.[34, 37-38] Cho et al. reported the honey-comb patterned current collector with conventional aluminum and copper foils by a reactive-ion etching process (Figure 4a).[34] They demonstrated excellent electrochemical performance of flexible LIBs using $LiNi_{0.75}Co_{0.11}Mn_{0.14}O_2$ (VNCM) cathode and composite of amorphous silicon and graphite anode (PNG-AES). The full cell test was carried out under in-situ bending at a speed of 30 mm min^{-1} with cycling at 4C rate, and the cell demonstrated a discharge capacity of ~90 mAh g^{-1} after 200 cycles at a harsh flexing condition (Figure 4b). The author described that the mechanical strength of the electrode was significantly increased by micro-scale patterns. Thus, the active materials could strongly be anchored to the patterns size of ~50 μm, where no detachment of the active materials was observed from the patterned foils. However, the intrinsic rigid property of pre-patterned metal foils and complex patterning process still limited their practical applications.

Alternatively, elastic polymers have been introduced to increase the flexibility of electrodes. A variety of polymers have been studied for current collector, which can be divided as follows: polymer substrates as scaffolds, conductive polymers and composites of a polymer with conducting agents. Cui et al. reported the stretchable electrode by using electrode composed of 3D porous PDMS scaffolds with LTO and LFP.[39] The 3D porous electrode could be stretched up to ~82%, showing good elastic property. Also, the conductive polymers such as polypyrrole and polyaniline derivatives have widely been used for flexible LIBs electrode.[40-41] However, the intrinsic lower conductivity of polymer substrates than conventional metal foils makes it difficult to be applied to the practical applications. Thus, combining polymers with conducting agents has received great attention to obtain both properties of the flexibility of polymers and high electrical conductivity of conducting agents.[42-44] For example, the composite of a polyaniline and carbon blacks (CB) was used as a current collector film by coating it on the both sides of the anode layer, as shown in Figure 4c.[35] This elastic CB layer could act as both flexible current collector layer and buffer layer against the volume expansion of silicon particles. In general, the conventional rigid metal foil current collectors have limited space for accommodating the pressure induced by the volume expansion of silicon particles, thus resulting in high stress to adjacent silicon

particles. However, by using the tri-layer CB/Si/CB electrode structure, the elastic layer could provide enough volume to alleviate the expansion of silicon particles. As a result, the cycle performance of a full cell assembled with LCO cathode was stable under different folding states, maintaining ~90% of the initial discharge capacity (Figure 4d).

Furthermore, there have been increasing volume in the research of carbon-based materials as current collectors. For example, CNTs,[45-47] carbon textiles,[48-51] and graphene derivatives[15, 36, 52] have been mainly reported because their interconnected networks can maintain the high electrical property upon flexing. A variety of hierarchical assemblies of CNTs for flexible LIBs were reported by Volder et al., and they suggested the several possible architectures for CNTs current collectors with high flexibility.[47] The origami battery also showed excellent deformed states under folding, twisting and bending condition by using the CNTs coated paper current collectors with the conventional slurry coating of LCO and LTO active materials.[53] It was revealed that the CNTs current collectors could enhance the mechanical stability and adhesion strength of active materials, as well as wetting property. Carbon textiles have also been used in flexible LIBs to replace rigid, bulky metal foil current collectors. For example, Tong et al. reported the flexible Fe_3O_4 anode and LCO cathode by using a porous carbon cloth as a current collector.[54] They evaluated battery flexibility under different bending states of flat, 45º, and 90º. The change of bent states did not increase the cell resistance and maintained stable discharge capacity of ~0.15 mAh cm^{-2} at a current density of 1.0 mA cm^{-2}. Furthermore, graphene derivatives have been intensively studied for flexible LIB current collectors because of their high electrical conductivity. Hu et al. developed the reduced graphene oxide (RGO) film for flexible LIB current collectors (Figure 4e).[36] The prepared RGO film showed a rough surface and increased surface area. This high surface area could enhance the contact between electrode coating layers and RGO film. For a wetting property test by the slurry ink, the RGO film fabricated with the LFP cathode materials showed the small contact angle of ~15˚ with slurry ink. The value was superior than that of the conventional metal foil of ~48˚, and the CNTs current collector of ~19˚.[55] The better wetting properties of the RGO film could increase adhesion with LFP active materials, showing no cracks or delaminations, when the electrode was wound along a rod with small radius. In addition, the cycle performance of the RGO/LFP electrode was also stable at a high C-rate of 5C, maintaining ~110 mAh g^{-1} (Figure 4f).

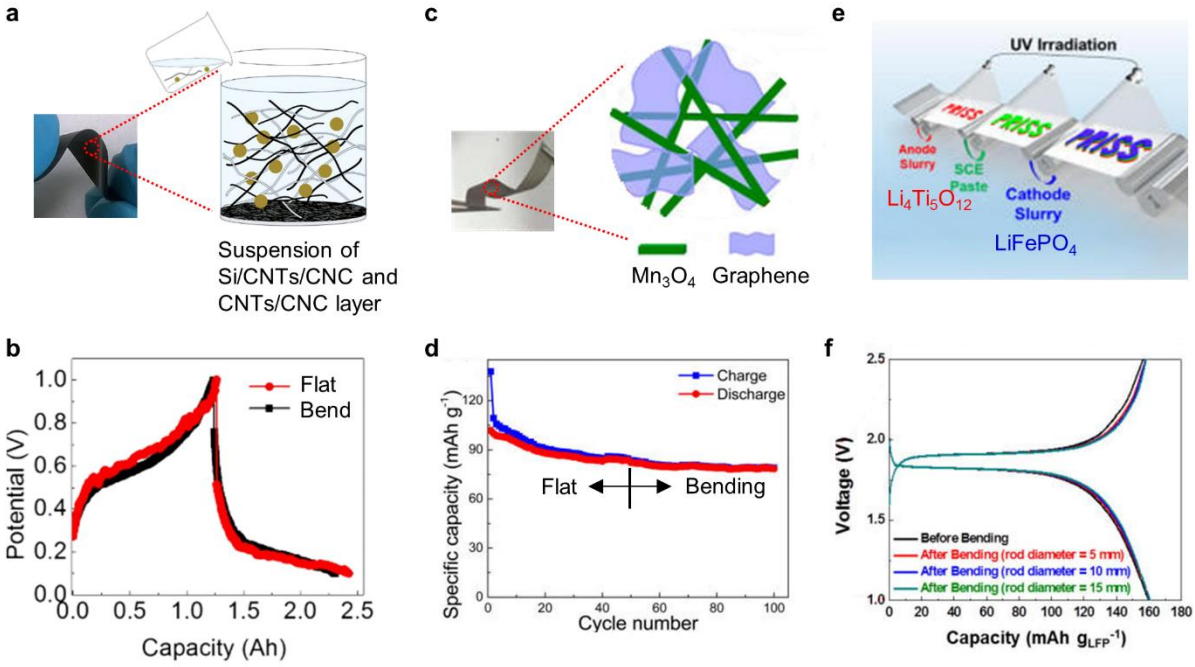

Figure 5. (a) Schematic of a fabricating free-standing electrode with Si/CNTs/CNC composites on a CNTs/CNT layer by a wetting process. (b) Voltage profile of Si/CNTs/CNC electrodes at a current density of 1.18 mA under flat and bending conditions, where the operating voltage ranged from 0.1 to1.0 V. Part a and b are reproduced with permission.[56] Copy right 2015, The Royal Society of Chemistry. (c) Schematic of a free-standing electrode of rGO/Mn_3O_4 by a chemical deposition process. (d) Cycle performance of full cells with rGO/Mn_3O_4 anode and LMO cathode at a current density of 100 mA g^{-1} under flat and bending conditions, where the operating voltage range of 2.0−4.1 V. Part c and d are reproduced with permission.[57] Copy right 2016, American Chemical Society. (e) Schematic of a fabricating free-standing electrode by a printing process. (f) Voltage profile of full cells with LFP cathode and LTO anode at a charge and discharge rate of 0.05C under different bending conditions, where the operating voltage range was 1.0−2.5 V. Part e and f are reproduced with permission.[58] Copy right 2015, American Chemical Society.

More practically, recent studies have focused on free-standing electrodes by incorporating active materials with current collectors. The conventional electrodes of LIBs consist of heterogeneous layers; electrode coating layers are placed on the current collectors. Thus, there are intrinsic problems related to the contact between electrode materials and current collectors when the cell was deformed. To overcome this issue, the free-standing electrodes that can interconnect the components of electrode materials have been studied by using wetting, chemical deposition and printing methods.

A wetting method is one of the simplest way for fabricating free-standing electrodes. The free-standing electrode can be fabricated by pouring a solution containing electrode materials to polymer substrates or conductive materials. This method usually accompanied a vacuum-filtration process which was similar to the paper-making process. Recently, a concept of paper batteries have received great attention due to their simple, cheap fabrication process, providing versatile battery designs.[59-60] Lee et al. reported a paper battery with high energy density, which was one of the outstanding works in terms of an ultra-thick loading of active materials without damaging electrodes upon flexing.[61] Figure 5a shows a free-standing, light weighted silicon paper electrode fabricated with Cladophora nanocellulose fibers (CNC) and CNTs by the wetting method. The prepared Si/CNC/CNTs electrode showed flexible paper-like property as well as mechanical robustness owing to strong adhesion between uniformly distributed silicon nanoparticles and the 3D conductive CNT/CNC networks. The cell with a Si/CNC/CNTs electrode and Li metal as a counter electrode demonstrated a discharge capacity of ~1.25 Ah under the deformed state, showing no discernible capacity loss compared with the flat state (Figure 5b).

For chemical deposition methods, active materials are usually deposited on conductive materials, showing a variety of morphologies such as totally encapsulated structures or well-dispersed nanostructures.[16, 62-64] For example, Edstrom et al. reported encapsulated silicon nanoparticles on a graphene foam as an anode.[65] The electrode was assembled with the LFP cathode. The capacity retention of the full cell was of >90%, under the different geometrical states such as bent or rolled conditions, demonstrating high mechanical strength. The robust, conductive network and hierarchical porous structure of the graphene foam acted as a pillar for active materials, and further enhanced the elastic property. Wei et al. reported the free-standing electrode, showing the well-dispersed nanostructured Mn3O4 on reduced graphene oxides (rGO) by a hydrothermal method (Figure 5c).[57] The strong bond between rGO and Mn_3O_4 not only enabled facile electron transfer but also provided mechanically robust structure. This was demonstrated in the full cell assembled with $LiMn_2O_4$ (LMO) cathode, indicating no degradation of cycle performance under bending states, maintaining the discharge capacity of ~80 mAh g^{-1} (Figure 5d). The author described that the high flexibility was achieved by the absence of the thick, stiff metal foil current collectors, and strong integrity of the free-standing electrode. As a result, the morphology of the folded free-standing electrode was well preserved without cracks, avoiding the

electrode delamination from current collectors.

Painting and printing processes for flexible electrode are also novel, simple fabrication methods for free-standing electrodes.[66-69] A stencil printing method has been usually used, and it have been already considered as a viable technique in a wide range of electronic industry including the LIBs fields. For example, Ajayan et al. studied a paintable battery by a spray painting process through stencil mask, and it attracted significant attention due to its simple approach for flexible batteries.[70] Recently, further advance research about printable LIBs was reported by Lee et al.[58] They fabricated printable solid-state batteries (PRISS) by multistep stencil printing processes of the printable LTO anode, solid-state composite electrolyte, and LFP cathode (Figure 5e). Notably, this printing technique allowed the versatile shapes of the flexible battery, for example, the "PRISS" letter shaped flexible battery was fabricated in this work. To further investigate the mechanical stability, the PRISS was wound along the rods with different diameters such as 5, 10, and 15 mm. The PRISS showed no appreciable deterioration of the discharge capacity, maintaining ~160 mAh g^{-1} under the different rods diameters (Figure 5f).

1.2.2 Design of flexible cell architecture

Along with the development of flexible electrode materials, a great deal of effort has been made to achieve the flexibility by changing the cell designs. When the cells are deformed, the stress is focused on certain areas of the cells. Therefore, to fully realize flexible LIBs, the cell architecture should be considered as well as electrode materials. Recent advances in flexible LIBs have been widely studied by designing novel cell architecture to enhance the mechanical stability, which will be discussed in this section.

The conventional LIB systems have a cofacial configuration of electrodes. Thus, the deformation of the cell give rise to opposite tensile/compressive stress towards cathode and anode coating layer.[71] In addition, this stress could induce friction force among electrodes when the cells were flexed. Choi et al. reported a unique electrode geometry to overcome this problem.[18] The battery showed the coplanar configuration in which $LiNi_{0.8}Co_{0.15}Al_{0.05}O_2$ cathode and graphite anode are placed on the same plane (**Figure 6**a). Since the electrodes were positioned on the same plane, the kinetic of ions transport was slower than conventional configurations. Therefore, the full cell test was performed in a quite low C-rate of 0.16C. For full cell test, the flexible coplanar cell demonstrated high flexibility under the deformed states. There was no capacity fading under the different bending radius of 10, 20 and 30 mm, and it powered the LEDs after 5000 bending cycles with a bending radius of 10 mm (Figure 6b). The coplanar geometry enabled thin, flexible batteries with high flexibility, showing a thickness of <0.5 mm and high voltage of 7.4 V by series connection, powering 6 LEDs under the bent state (Figure 6c).

Cable- and wire-type batteries are different from the conventional flat and rigid batteries, which are considered as feasible cell configuration for wearable systems. Peng's group is the pioneer of the cable-

and wire-type batteries, and they reported several studies about wire-shaped batteries.[19, 72] Their electrochemical performance was reliable under extremely deformed conditions. For example, one of the outstanding studies of this group was shown in the Figure 6d.[73] The LTO and LMO nanoparticles were used as active materials and dispersed with the MWCNT skeleton to form a yarn structure. This structure enabled highly deformable shapes such as different knot structures, maintaining mechanical and electrochemical properties. The full cell showed only 3% of the discharge capacity drop after 1000 bending cycles, indicating high cycling stability. Also, after the yarn electrode was made into a spring structure for a stretchable battery, the high elastic property of the electrode could be realized, powering LEDs under increasing elongations from 0%, 40% and, 100%, and over the 80% of the initial discharge capacity was maintained at the 100% stretched state (Figure 6e). Moreover, a longer wire enabled a large-scale electrode and showed high deformability with twisted structures (Figure 6f). This long, thin structure of the wire battery could decrease the stress concentration on the electrode upon flexing.

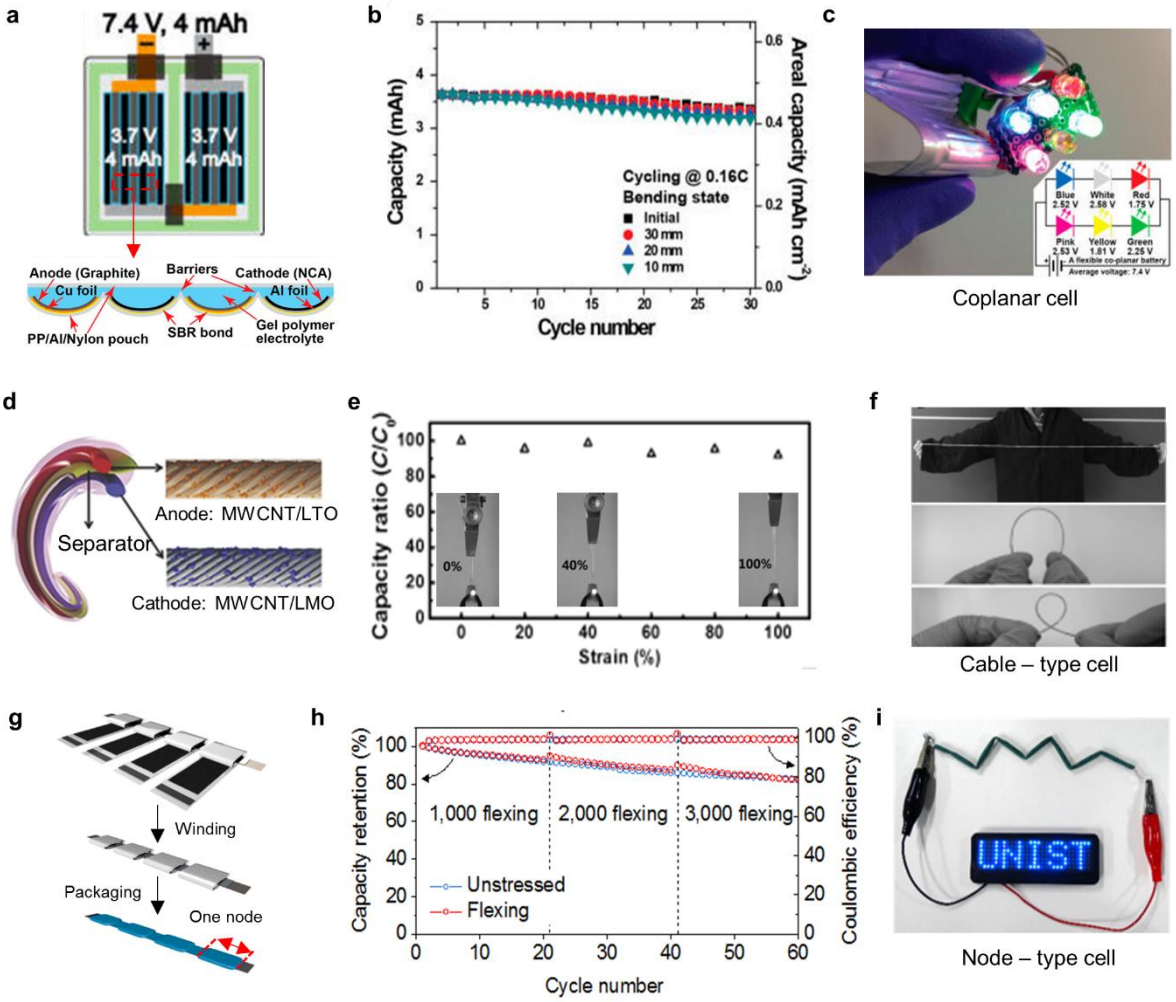

Figure 6. (a) Schematic of a coplanar LIB configuration. (b) Cycle performance of the coplanar cell with NCA cathode and graphite anode at a current density of 0.16C under different bending conditions, where the operating voltage range was 5.0−8.2 V. (c) Photograph of coplanar cell illuminating six LEDs under a bent condition. Part a-c are reproduced with permission.[18] Copy right 2015, American Chemical Society. (d) Schematic of a cable-type LIB. (e) Capacity retention of full cells using LMO cathode and LTO anode with increasing strain from 0% to 100% at a current density of 0.01 mA cm^{-1}, where the operating voltage ranged from 1.5 to 3.2V. (f) Photographs of cable-type cell with high deformability. Part d-f are reproduced with permission.[73] Copy right 2014, Wiley−VCH. (g) Schematic of a node-type LIB. (h) Cycle performance of full cells with LCO cathode and graphite anode at a current density of 1C under intermittent flexing 1000 times per 20 charge/discharge cycles, where the operating voltage ranged from 3.0 to 4.3 V. (i) Photograph of the node-type cell illuminating blue LEDs under the deformed state. Part g-i are reproduced with permission.[22] Copy right 2017, Wiley−VCH.

In addition, island-bridge structures have been studied for flexible LIBs. For instance, Rogers et al. successfully fabricated the stretchable battery by introducing island-bridge design.[74] The cell showed high flexibility because the segments of the electrodes were interconnected with serpentine coil, showing stretchability of >300% and reversibility of >200%. Furthermore, kirigami LIBs was developed by Jiang et al., which showed similar function to the island-bridge design.[75] The electrode was fabricated with conventional electrode coating process and cut to different patterns, providing less stress on deformed sites. It also showed high deformability with 150% of stretchability. More recently, Cho et al. reported the novel cell design of the node-type LIBs by using conventional LCO cathode and graphite anode.[22] After slurry casting on the electrode, the node-type cell was prepared by winding the electrodes on the metal straps (Figure 6g). The one node showed linear capacity of ~6.9 mAh cm^{-1} at 0.5C-rate, and it could increase to ~10 mAh cm^{-1} by increasing mass loading of active materials. Moreover, the energy density was increased as increasing the number of the node, showing a discharge capacity of ~60 mAh at 6 nodes. Importantly, the node-type cell showed stable cycle stability during flexing tests (Figure 6h). The 1000 flexing cycles were repeated before initiating cycles, after 40th and 60th cycles. The electrochemical performance of stressed cell was almost same as unstressed cell, maintaining ~80% of the initial discharge capacity because the flexed part of the battery was the metal straps. Thus, the segmented cells were not damaged by flexing test. For the practical application, the full cell powered the LEDs under deformed state, which were ascribed to the unique cell structure of the node-type cell (Figure 6i).

1.3 Current issues of flexible LIBs

To date, most of the approaches for the development of the flexible batteries have focused on the improvement of their performances. However, a fundamental understanding such as degradation mechanism of cells upon flexing is another important step for the practical applications. The flexing process have accompanied the delamination of electrodes material and crack generation, resulting in partially isolated particles. This issue could accelerate battery degradation by increasing internal resistance between particles and side reaction with electrolyte. Moreover, the currently reported flexible LIBs with novel fabrication methods have not been applied to the practical use because of several critical issues. For example, although they showed good mechanical property and reasonable flexibility, their complicated fabrication methods and low electrochemical performance have not reached commercialization standards of LIBs. In the following section, we will discuss the above-mentioned issues of flexible LIBs for practical applications.

The main purpose of this section is to discuss the failure mechanism of the conventional LIB systems upon flexing, highlighting safety issues. In general, the electrode slurry consists of active materials,

conducting agents and a binder, which was coated on metal foil current collectors. Thus, the contact between the active materials and current collectors could be weakened when a flexing test was repeated, resulting in the delamination of active materials from the current collectors. Durstock et al. studied the failure mechanism of the flexible LIBs by performing a dynamic mechanical test.[76] They repeatedly folded the cell consisting of the LTO anode and LFP cathode every 20 seconds while discharging the cell (**Figure 7**a). Even though the loading level of the active material was relatively low with ~2.0 − 2.5 mg cm^{-2}, severe voltage spikes were observed in the cell, which showed a complete failure after 186 folding. The main reason of the voltage spike originated from the delamination of electrode coating layers from current collectors. Notably, the metal foil current collector cannot accommodate the mechanical stress, causing severe buckling or fracture along the folding line for both LFP cathode and LTO anode (Figure 7b). This process further increased the delamination of the active materials from the current collectors, which was confirmed from the cross-section image of the LFP electrode (Figure 7c). To further understand failure mechanism upon flexing, we performed the bending test by using the electrode with the commercialized loading level, which was ~20 mg cm^{-2} of LCO cathode and ~9.5 mg cm^{-2} of graphite anode (Figure 7d–h). The full cell was flexed for 5000 times and reassembled the cell by dividing bent and non-bent sites, respectively (Figure 7d). The discharge capacity of the non-bent site was maintained with ~15 mAh, however, that of the bent site showed poor capacity retention (Figure 7e,f). We disassembled the cell and analyzed each surface of electrodes. In comparison to non-bent site, a severe contact loss of active materials was observed in the bent site, showing significant capacity fading (Figure 7g,h). The crack and delamination of electrodes could generate partially isolated particles, which eventually give rise to poor electron transfer and ionic transport kinetics with uneven current distribution.[77-78] When this phenomenon is continued, it may trigger the safety issues such as Li plating and thermal runaway under the flammable organic electrolyte.[79]

In general, the conventional LIB systems increase their capacity by increasing the loading level of active materials, which usually increase electrode thickness. In terms of flexible energy storage system, thick electrodes have limited deformation states when folding, bending or stretching the cell. Thus, most researches for flexible LIBs have been carried out under low loading levels of active materials, thus showing low energy density. This low volumetric energy density and limited flexibility should be improved for the current flexible batteries. In addition, in comparison to the conventional LIB manufacturing process, the complicated fabrication processes of currently reported flexible electrodes may cause critical issues for the practical application. For example, facile, simple slurry casting process has been used in the commercialized LIBs. However, recent progress of the flexible electrode prepared by wetting, chemical deposition, or printing method often requires new types of flexible materials and prolonged process time, which hinders the early introduction of the flexible LIBs in the market. Moreover, in terms of cable-type or stretchable LIBs, the additional cell package with improved stability

is needed to maintain the cell structure. For example, the rigid pouch-type package should not be used in the deformable cells; thus, researchers have used the heat-shrinkable tube or PDMS packages. However, these types of cell packages could not completely prevent air diffusion, leading to additional degradation of cell components. Such limitations have hindered commercialization of newly designed flexible batteries until now.

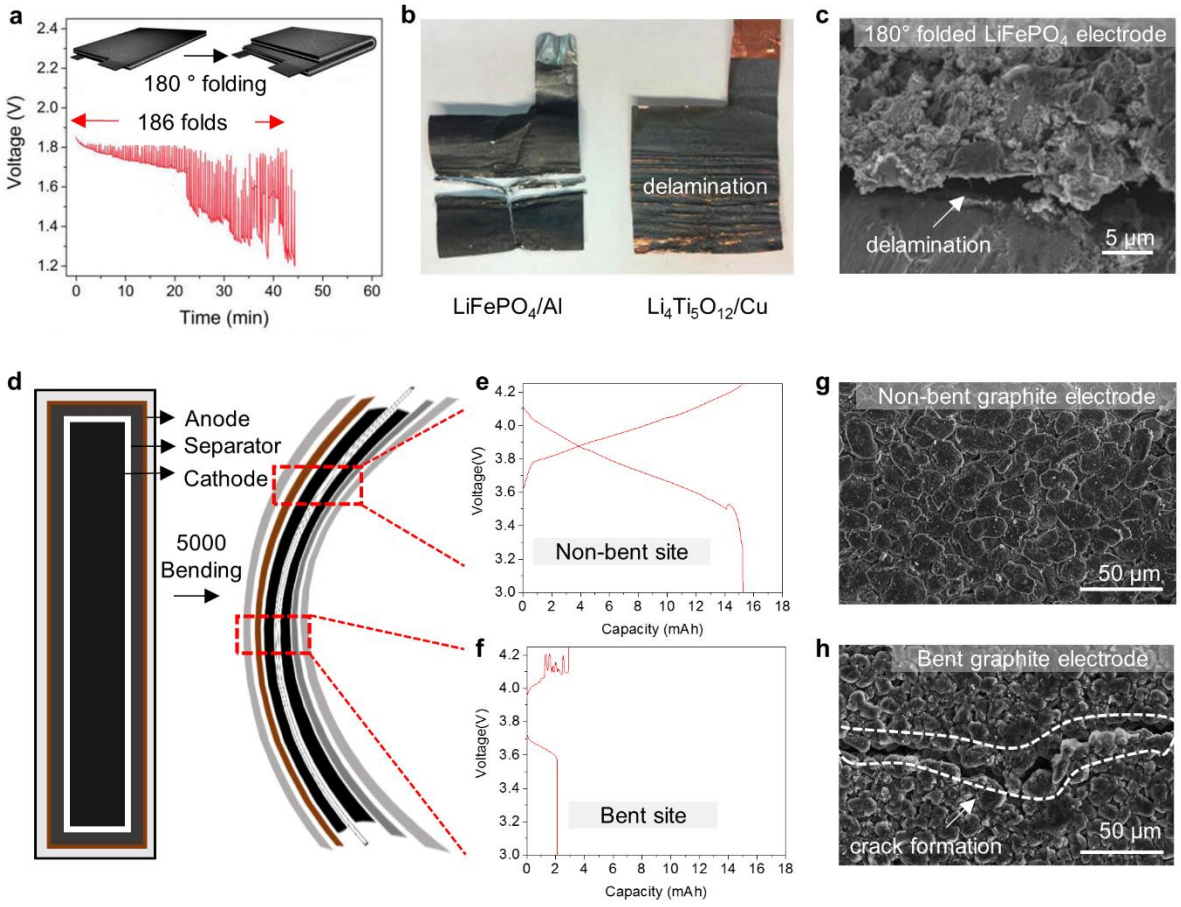

Figure 7. (a) A discharge voltage of a full cell with LTO anode and LFP cathode at a C-rate of C/5 when the cell was repeatedly folded. (b) Photograph of the LFP and LTO electrodes after in-situ folding test. (c) The SEM image of the cross-section for LFP electrode. Part a-c are reproduced with permission.[9] Copy right 2016, American Chemical Society. (d) Schematic of bending state of conventional LIBs. Voltage profiles of the reassembled (e) non-bent and (f) bent site of the full cell after bending 5000 times, where the operating voltage is range was 3.0−4.3 V. SEM image of the (g) non-bent and (h) bent site of graphite electrodes. Part d-h are unpublished results.

1.4 Strategy for future practical application

As mentioned above, the conventional flexible LIBs have a critical problem of delamination of electrode materials with crack formation, leading to safety issues. Also, their electrochemical performances and flexible properties are still limited for the practical use. In this section, we will discuss the strategies for flexible lithium-based batteries based on the conventional LIBs, especially focusing on current challenges.

Conventional LIBs

One simple solution to prevent the delamination of active materials from current collectors is changing the current collector. A variety of methods for the improvement of the flexibility changing current collector have been introduced in the section 2, such as polymer substrates or conductive materials. Although polymer derivatives enhanced the flexibility of the electrodes, the conductive materials would be more beneficial for the electron transfer, achieving the main purpose of the current collectors. Currently, CNTs have been considered as a promising candidate for replacing conventional metal foil current collectors. For example, Arias et al. reported the simple, facile method for the preparation of the flexible electrode (**Figure 8**a).[80] The CNTs film was prepared by spray printing process, followed by the adhesion with LCO as cathode, LTO as anode materials. Although the current collector layer and active material layer were separated, the Van der Waals interaction between CNTs layer and active material films enhanced the adhesion between electrodes. The SEM image of the cross section for CNTs/LTO electrode indicated that thin CNTs layer was well adhered to LTO layer (Figure 8b). This was also demonstrated by the stress-strain curves of the electrode. For example, the LTO electrode showed the tensile strength of ~6.85 MPa, which was an order of magnitude higher value than previously reported value of ~0.12 MPa by Wang et al. The high mechanical strength could contribute the stable cycle performance after flexing test under different bending radius. The cell showed high areal capacity of ~1.0 mAh cm^{-2}, which was maintained even at bending radius under 10 mm (Figure 8c). Notably, there were no crack and delamination of active materials from current collectors after 300 flexing.

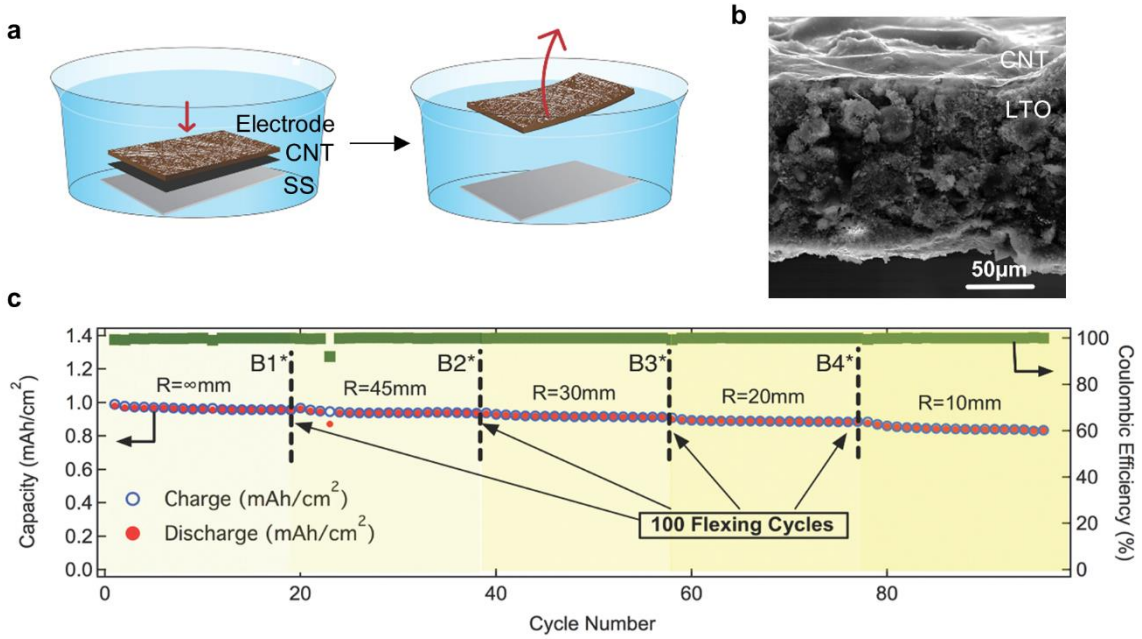

Figure 8. (a) Schematic of fabricating electrodes using CNTs. (b) Cross-section SEM image of the LCO/CNT electrode. (c) Cycle performance of the full cell with LTO anode and LCO cathode at C-rate of C/2 under intermittent 100 flexing between 20 cycles, where the operating voltage ranged from 1.6 to 2.6 V. Part a-c are reproduced with permission.[80] Copy right 2015, Wiley−VCH.

In the next section, we suggested a novel approach for flexible LIBs from the viewpoint of the conventional electrode fabrication process. **Chapter 2** describes a flexible node-type lithium-ion batteries with novel post-patterned electrodes. This concept can be fabricated via simple, one-step process. In addition, the selectively-pressed grid pattern enables a high adhesion property of electrode coating layers, thus resulting in enhanced cycle stability and rate capability. **Chapter 3** reports the *Lego-like* 3D block structure for high energy flexible lithium-ion batteries. This unique structure prevents electrode delamination and layer shifting when the cells were flexed.

Chapter 1 was reproduced from Cha H., Kim J., Lee Y., Cho J., Park M. Issues and challenges facing flexible lithium-ion batteries for practical application. *Small*, accepted (2018)

Chapter 2

Post-patterned electrodes for flexible node-type lithium-ion batteries

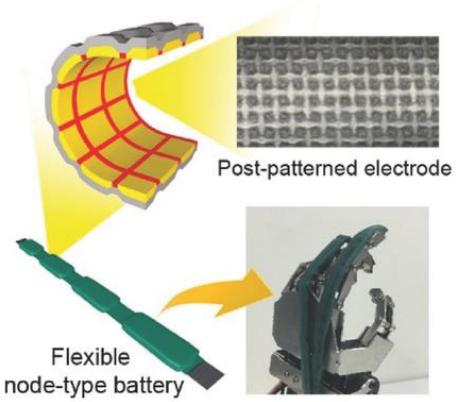

A new design concept is considered as a reliable approach to develop flexible lithium-ion batteries (LIBs), which has been widely studied. However, to meet the high standard of commercial LIBs, their electrochemical performances still lag behind. Here we demonstrate a flexible node-type LIB with novel post-patterned electrodes. The post-patterned electrodes were prepared via a simple, one-step process involving an additional pressing step of conventional electrode in the presence of flattened mesh template. We show that the selectively-pressed grid pattern enables a high adhesion property of electrode coating layer. Notably, a combined experimental and simulation result reveals that this unique structure helps to distribute concentrated-stress when deforming the electrode. Moreover, the node-type LIBs with segment parts for energy storage and mechanical deformation exhibit stable cyclabiliy for 3,000 flexing cycles. Our study on flexible battery suggests that the node-type architecture lends itself to the design of highly deformable energy storage applications.

This chapter has been published.

Reproduced with permission from Park M., Cha H., Lee Y., Hong J., Kim S.Y., Cho J. Postpatterned Electrodes for Flexible Node-Type Lithium-Ion Batteries. *Adv. Mater.*, 29, 1605773 (2017).

2.1 Introduction

As the shapes of wearable and portable electronic devices have become more diverse, there have been increasing demands for flexible energy storage systems.[4] To meet these demands, lithium-ion batteries (LIBs) have been the most intensively studied owing to their high energy density, long-term cycling performance, and verified safety for several decades.[81-83] The study of flexible LIBs can be approached from two distinct perspectives: that of developing deformable electrode materials, and that of improving cell structure designs. In terms of material designs, there are a variety of flexible active materials that use polymeric materials,[28] carbon nanotubes (CNTs),[12, 56, 61, 84-86] and graphene derivatives.[51, 87-88] In addition, various flexible substrates—such as conductive textiles, papers, and fibers—have been fabricated using CNT- and graphene-based materials.[23, 28, 88-91] However, applying these carbon-based nanostructures to the manufacturing process of LIBs is currently a difficult task given constrains regarding mass production and processability.[92] In addition, the electrochemical performance of carbon-based substrates still lags behind that of highly conductive Cu and Al substrates, in that such carbon-based substrates possess low energy densities and poor rate capabilities.[51, 91] Although, each component of the LIB (and the corresponding manufacturing processes) has been widely studied in order to achieve reliable flexibility, the corresponding electrochemical performance is still limited in relation to the high commercial standards of LIBs: (1) high mass loading of active materials for high energy density, (2) good electrical conductivity like metallic substrates, (3) repetitive flexing cycles with stable capacity retention, and (4) simple method readily applicable to roll-to-roll electrode coating process.

With respect to cell designs, unique architectures for LIBs with bendable,[80] stretchable,[73-74, 93] or foldable[53, 75, 91, 94] functions have been reported by using traditional active materials, such as various metal-oxides ($LiCoO_2$, $LiFePO_4$, $Li_4Ti_5O_{12}$, etc.) or graphite. For instance, origami LIBs by adopting commercial $LiCoO_2$ and $Li_4Ti_5O_{12}$ coated CNT papers have demonstrated superior folding and unfolding deformability for 50 flexing cycles.[53] In particular, Rogers' group introduced a novel concept for stretchable LIBs by using small segments of $LiCoO_2$ and $Li_4Ti_5O_{12}$ electrode disks with silicone elastomer packaging.[74] However, the number of flexing cycles during operation is still limited to verify the high flexibility. Another example includes the coplanar cell configuration, wherein graphite anodes and $LiNi_{0.8}Co_{0.15}Al_{0.05}O_2$ cathodes are positioned in the same plane. This structure exhibits considerable bending capability with stable open-circuit voltage (OCV) for 5000 flexing cycles, however, the rate capability at 0.8 C was only 47% of the original capacity.[18] Nevertheless, the advantage of these approaches is that there is no need for additional considerations regarding basic properties of active materials and safety issues, which is not the case in the development of novel materials. More importantly, these kinds of cell configurations do not transform the active material itself; they merely bend or fold certain deformable parts.

A general strategy in deforming LIBs without damaging the electrode is to develop current collectors

with high flexibility and mechanical strength. Recently, several patterned current collectors for use in flexible LIBs have been reported by using photolithography with a wet etching method; such current collectors (e.g., trench- or honeycomb-patterned foils) demonstrate an improved adhesion force between the electrode coating layer and the substrate, along with an enhanced cycle stability, and rate capability, compared to nonpatterned substrates.[34, 92] However, this method is substantially complicated and inappropriate for industrial upscaling. Although great progress has been made, the improvements are still far from addressing the potential problems, such as an irregular loading level of active materials, which arise because of surface roughness and hole structures of the preformed patterns on metal foils.

Herein we developed flexible node-type LIBs by winding the prepared post-patterned positive and negative electrodes on metal straps. Based on the inverse manufacturing concept, the post-pattern electrodes were fabricated by additionally patterning an electrode prepared by conventional slurry coating and pressing process. Importantly, the node-type full cell showed significantly improved cycle stability and rate capability without any electrolyte additives or active materials treatments.

2.2 Experimental detail

Preparation of the post-patterned electrodes.

The positive electrode was prepared by a conventional slurry coating method using cathode material ($LiCoO_2$, Samsung SDI), conductive agent (Super P, TIMCAL), and poly(vinylidene fluoride) binder with the mass ratio of 96:2:2 in N-methyl-2-pyrrolidinone solution. The slurry was homogenized at 7,000 rpm for 30 min. After that, slurry was uniformly coated on the aluminum foil (thickness: 15 μm) with the loading level of ~13.3 mg cm^{-2}, and the electrode was calendared by roll-pressing machine to the loading density of ~3.6 g cc^{-1}. The negative electrode was composed of natural graphite (BTR) as anode material, Super P as conductive agent, and poly(vinylidene fluoride) binder with the mass ratio of 93.5:0.5:6 in N-methyl-2-pyrrolidinone solution, including 0.2 wt% of oxalic acid (Sigma-Aldrich). The slurry was homogenized at 2,000 rpm for 15 min. After that, slurry was uniformly coated on the copper foil (thickness: 18 μm) with the loading level of ~5.5 mg cm^{-2}, and the electrode was calendared to ~1.4 g cc^{-1}. The nickel mesh (40-sized mesh) was used as a template, and it was flattened from 230 to 130-μm-thick by the roll-pressing machine (Figure 9). In case of the pre-patterned electrodes, the Al and Cu foils were firstly patterned by the prepared nickel mesh template, then the same slurry coating process was carried out (Figure 10). For the post-patterning process, the prepared electrodes were placed onto the mesh template, and subsequently pressed by the roll-pressing machine. The gap between two rolls was less than the total thickness of the electrode and nickel mesh, where the gaps were set to 90% in cathode side and 95% in anode side, respectively.

Half-cell test.

The coin-type cell (2032R) was assembled for half-cell test using Li foil as a counter electrode and microporous polyethylene (PE) a separator in 1.15 M $LiPF_6$ in ethylene carbonate (EC)/dimethyl carbonate (DMC)/diethyl carbonate (DEC) (3:4:3 vol%; Panax Starlyte). All cells were prepared in argon-filled globe box. The electrochemical properties were evaluated by a battery cycle tester (WBCS-3000, WonATech Co.) at 25°C. The voltage windows ranged from 3.0 V to 4.45 V with a constant current (CC) mode and maintained at a constant voltage (CV) mode of 4.45 V in $LiCoO_2$ half cells, and from 0.05 V to 1.5 V with CC mode and CV mode of 1.5 V for graphite half cells. The cycle retention tests were performed at 0.5C for both cathode and anode, and rate capability properties were carried out at a fixed charge rate of 0.5C and different discharge rates of 0.2C, 0.5C, 1C, and 2C.

Node-type LIB and its electrochemical test.

Node-type LIBs were assembled by using the post-patterned electrodes with the size of 13 mm × 45 mm cathode and 15mm × 50mm anode (Figure 11), where the N/P ratio was ca. 1.1. Firstly, the post-patterned cathode and anode electrodes were welded on the aluminum strap and nickel strap with an interval of 15 mm, respectively. For example, one node was made by stacking the cell component as following sequence; separator, anode, separator and cathode. Next, the electrode was densely wound on the metal straps in series. The node-type cell was impregnated in the electrolyte of 1.15 M $LiPF_6$ in EC/DMC/ DEC for 24 hours in a pouch. Node-type full-cell for flexing test was prepared by a heat-shrinkable tube with heating gun. The electrochemical properties of node-type full-cell were obtained at the voltage ranging from 3.0 to 4.35 V with CC/CV modes. The cycle data was obtained at a rate of 1C, and rate capability were tested with fixed charge rate of 1C and different discharge rates of 0.5C, 1C, 2C, 3C, and 5C. Direct current internal resistance (DC-IR) results were obtained by using a pulse current from 0.5C to 2.5C rates at SOC 50% condition after 10 seconds duration.

Characterization.

The surface morphology and cross-sectional images of the electrodes were obtained by scanning electron microscopy (SEM, Verios 460, FEI). Adhesion test was tested by universal testing machine (INSTRON Co.) with a constant speed of 50 mm min^{-1}. Firstly, adhesive tape (scotch magic tape 810R, 3M) was applied in each electrode, then it was pulled away from the electrode at 180° to the surface. Tensile strength of electrode was also obtained by an Instron tensile tester, where all electrodes were prepared with the same size of 10 mm × 80 mm. The flexing test of node-type cells was carried out at a bending/stretching speed of one flexing per 8 seconds (150 cm min^{-1}) for 3,000 times. Simulation results representing the deformation and von Mises stress distribution were obtained by commercial

finite element package ABAQUS.

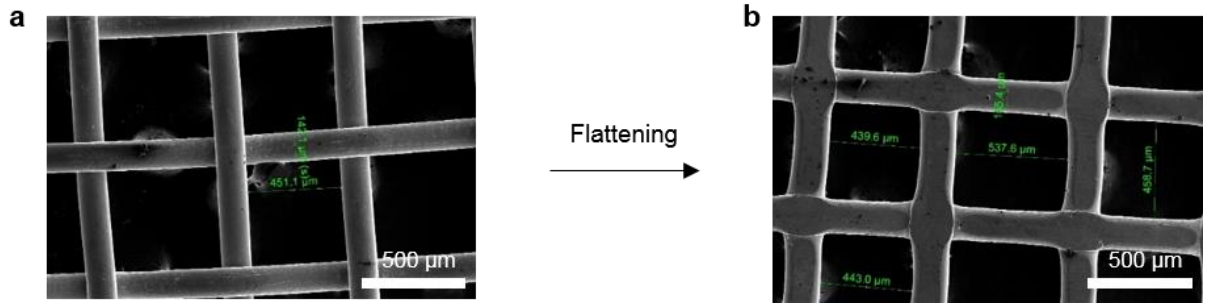

Figure 9. SEM image of **a**) pristine nickel mesh (40-sized mesh), and **b**) flattened nickel mesh as a template.

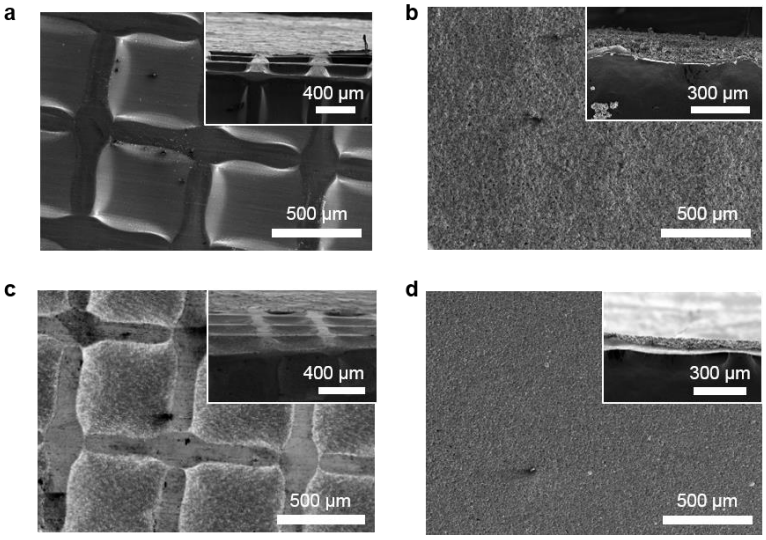

Figure 10. a) SEM image of pre-patterned Al foil, and **b**) its surface morphology showing electrode materials coated onto pre-patterned Al foil. **c**) SEM image of pre-patterned Cu foil, and **d**) its surface morphology showing electrode materials coated onto pre-patterned Cu foil.

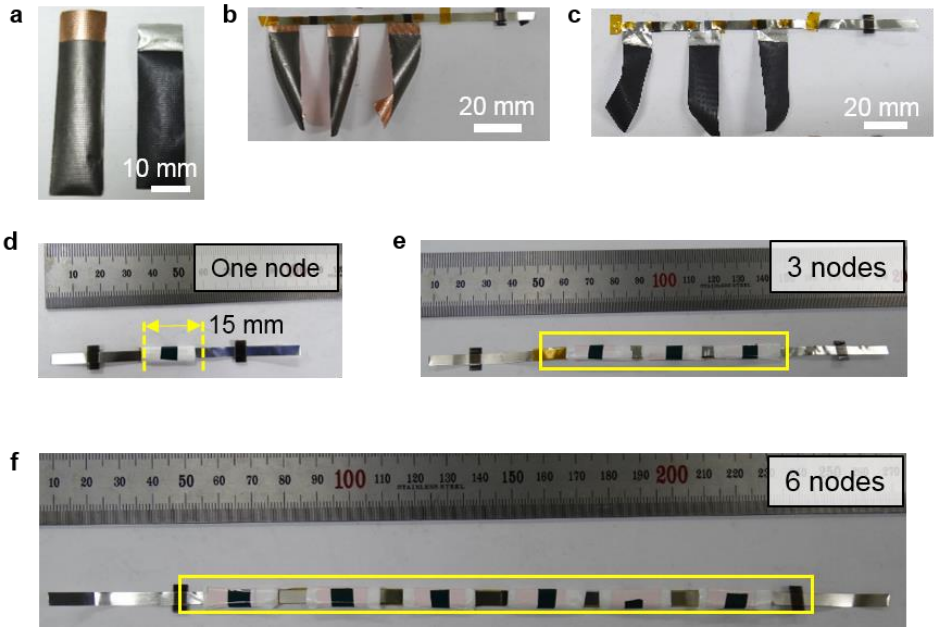

Figure 11. Digital photograph of **a**) post-patterned anode and cathode electrodes the size of 13 mm × 45 mm cathode and 15mm × 50mm anode, **b**) nickel strap welded with post-patterned anodes, **c**) aluminum strap welded with post-patterned cathodes. **d**–**f**) Prepared node-type cells with 1, 3, and 6 nodes.

2.3 Results and discussion

The preparation process of the postpatterned electrodes is different from the previously reported patterning methods, which utilize lithography or chemical etching (referred to as prepatterning methods).[34, 95] Generally, the metal current collectors are initially patterned before slurry coating and pressing. In contrast, the postpatterning process is carried out at the end of the electrode manufacturing process. First, the nickel mesh template (40-sized mesh) was subjected to a flattening process by roll-pressing machine to form square shapes with flat wires (Figure 9). Using this template, we prepared two kinds of patterned electrodes, which were divided into pre- and postpatterned electrodes (Figure 12). As for the prepatterning process, embossing structures were first formed by an elongation of metal foils, which yielded a square with a side length of ≈500 μm with an increased surface area of ≈4.5% (Figure 10a,c). When coating electrode materials onto the prepatterned foils, the loading density of active materials was nonuniform because of the raised pattern with a concave surface compared with a flat substrate (Figure 10b,d).

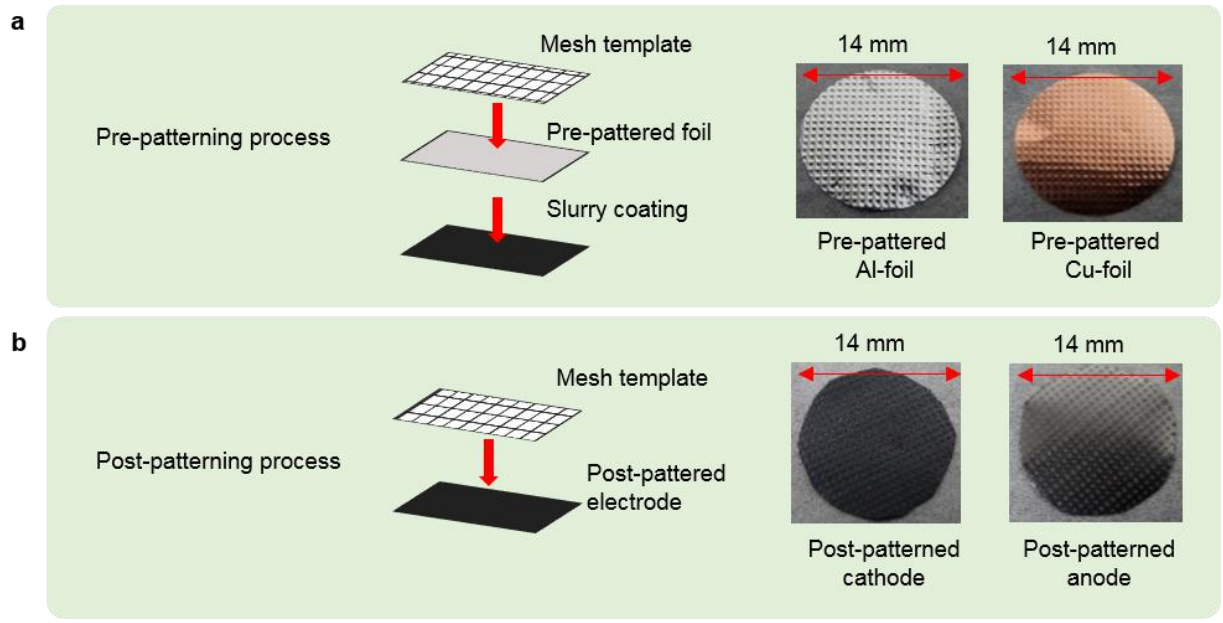

Figure 12. Preparation of **a**) pre-patterned, showing digital photograph of pre-patterned Al- and Cu-foil, and **b**) post-patterned electrode, showing post-patterned cathode and anode electrodes.

By way of contrast, after finishing the conventional electrode preparation process, the postpatterning was performed via a roll-pressing machine using the prepared mesh template, as shown in Figure 13a. At first, cathode and anode were prepared using a conventional electrode manufacturing process. The loading levels of LiCoO2 (LCO) cathode- and graphite anode- active materials were adjusted to about 13.3 and 5.5 mg cm−2. The scanning electron microscopy (SEM) images confirmed uniform coating layers consisting of LCO and graphite particles (Figure 14). In the postpatterning step, we additionally pressed the prepared electrodes using the mesh template, generating the selectively pressed grid patterns. Figure 13b shows the top-view of the postpatterned graphite electrode, wherein the grid pattern with regular square shapes can be observed. Furthermore, a concave cross section confirms that active materials were more densely packed on the grid pattern (Figure 13c,d). The surface morphology of the postpatterned cathode and its cross section are also presented in Figure 15. In both the cathode and anode, the variation of the electrode thickness was observed in the grid pattern (Figure 16a,b); this implies that the mass loading density changed between the pressed and nonpressed parts. This can be explained by the fact that the active materials in the grid pattern were highly pressed by the mesh template, with the rest being moved into the concave area of the nonpressed parts, thus resulting in stably packed coating layers (Figure 16c). We expect that intentionally formed regular grid patterns with high densities can offer increased adhesion force between metal substrates and active materials, which will be further discussed below.

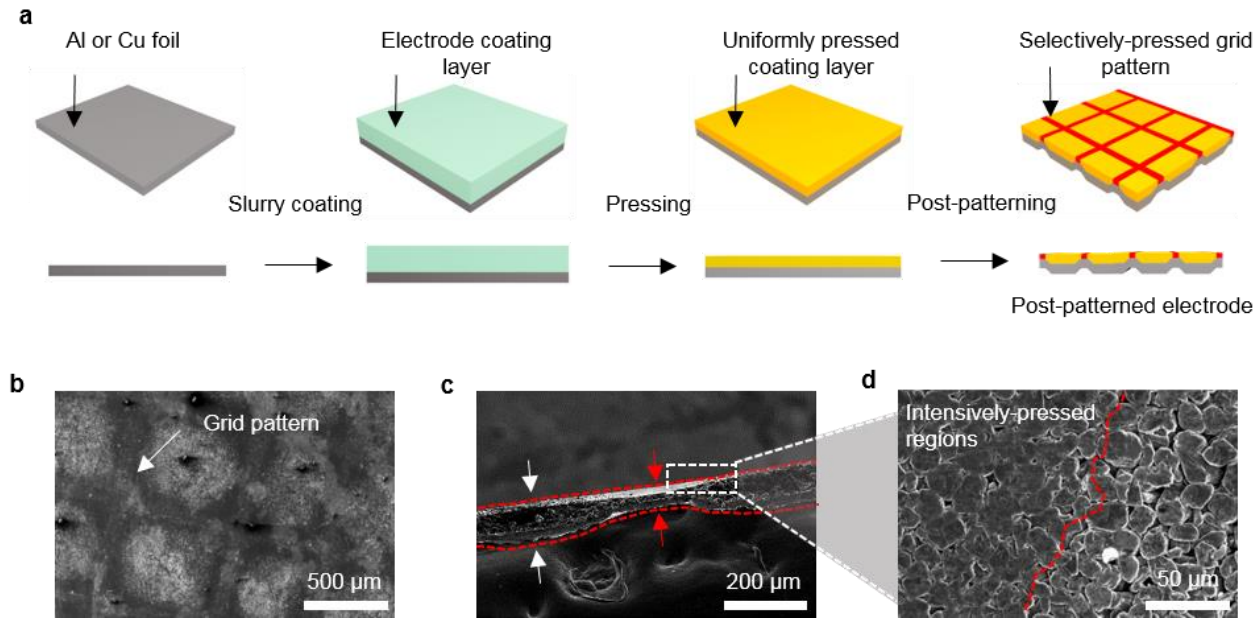

Figure 13. Post-patterning process and microstructure of a graphite anode electrode. (a) Schematic of the fabrication process for the post-patterned electrode. After finishing a conventional electrode manufacturing process (slurry coating and pressing), an additional process is performed by patterning electrode using a 40-sized mesh template. (**b**) SEM image of a surface morphology of the post-patterned anode electrode, showing selectively-pressed grid pattern (indicating white arrow), and (**c**) its cross-section, where red arrows indicate the pressed region. (**d**) Magnified top-view of the post-patterned anode, showing a distinctive boundary of pressed graphite-anode materials.

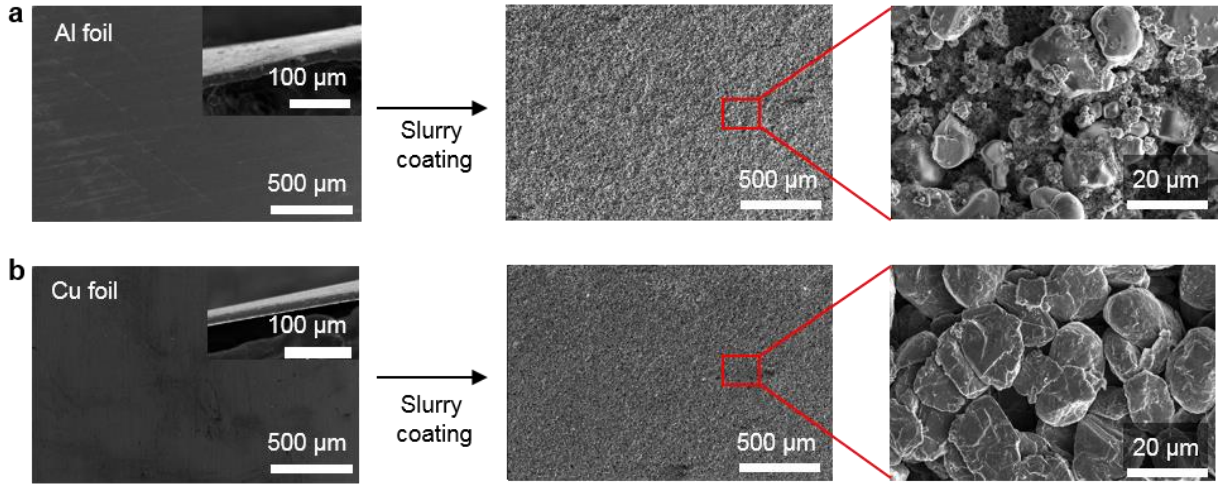

Figure 14. a) SEM image of pristine Al foil, and it surface morphology showing $LiCoO_2$-cathode active materials with its magnified image. **b**) SEM image of pristine Cu foil, and it surface morphology showing natural graphite-anode active materials with its magnified image.

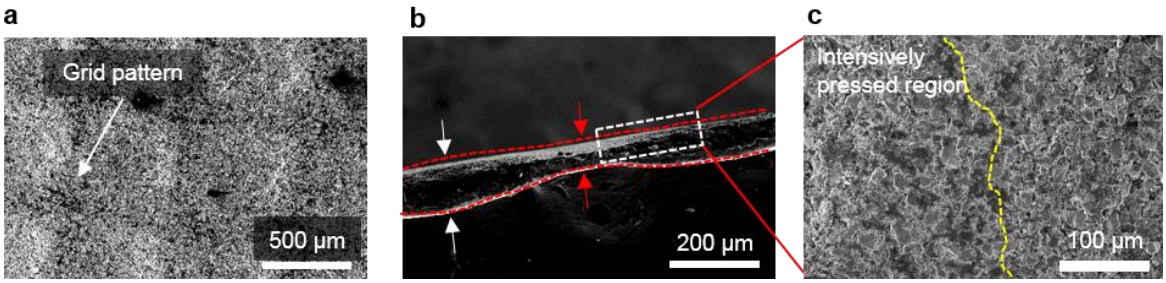

Figure 15. a) SEM image of a surface morphology of the post-patterned cathode electrode, showing selectively-pressed grid pattern (indicating white arrow), and b) its cross-section, where red arrows indicate the pressed region. (c) Magnified top-view of the post-patterned cathode, showing a distinctive boundary of pressed active materials (LCO).

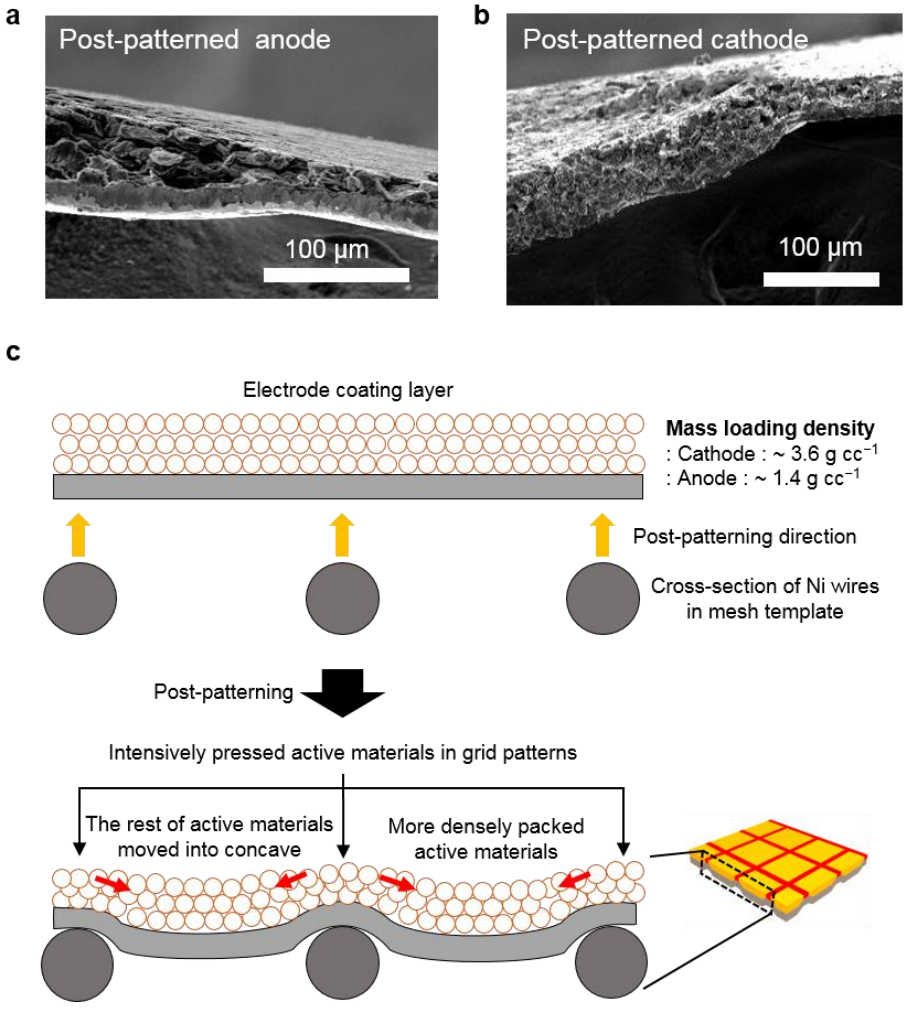

Figure 16. a) SEM image of a cross-section view showing a morphology of the post-patterned anode electrode. b) SEM image of a cross-section view showing a morphology of the post-patterned cathode electrode. c) Schematic of post-patterning process, explaining that active materials can be moved by post-patterning process.

After postpatterning the electrodes, the physical characteristics of the slurry-coated metal foils were investigated by a universal testing machine (UTM). At first, the adhesion forces between the electrode coating layer and metal substrate were measured after applying adhesive tape onto the electrode surface and pulling away from the electrode at 180° to the surface at a constant rate of 50 mm min−1 (Figure 17a,b; Figure 18). As shown in Figure 17c, the postpatterned anode exhibited highly improved adhesion with a maximum peak of ≈0.4 N; compare this value to the peak of the nonpatterned anode (≈0.08 N). This behavior was consistent with the results of the cathode side (Figure 17d). The maximum peak in adhesion force for the postpatterned cathode represented an improvement of ≈23% compared to the nonpatterned cathode. In addition, the adhesion force during the peeling test was on average higher in the postpatterned electrodes compared to the nonpatterned and prepatterned electrodes (Figure 17c,d; Figure 19). After adhesion tests, the electrode coating layer was easily peeled-off in the nonpatterned electrodes, exposing metal foils with minimal electrode residue (Figure 20). By way of contrast, in the case of the postpatterned electrodes, the peeled-off electrode with unique grid patterns remained on the adhesive tape, resulting in increased amounts of electrode residue on the metal foils. Thus, it is evident that intentionally formed regular grid patterns on the electrode surface can increase the adhesion properties between the metal substrate and electrode coating layer. This also implies that the cycle stability and rate capability can be improved from the point of view of active materials contact and electrical resistance between particles. In addition, the tensile strength of each electrode was also measured, and the postpatterned electrodes showed comparable ultimate tensile strength in both Cu and Al foils, compared to the non- and pre-patterned electrodes (Figure 21).

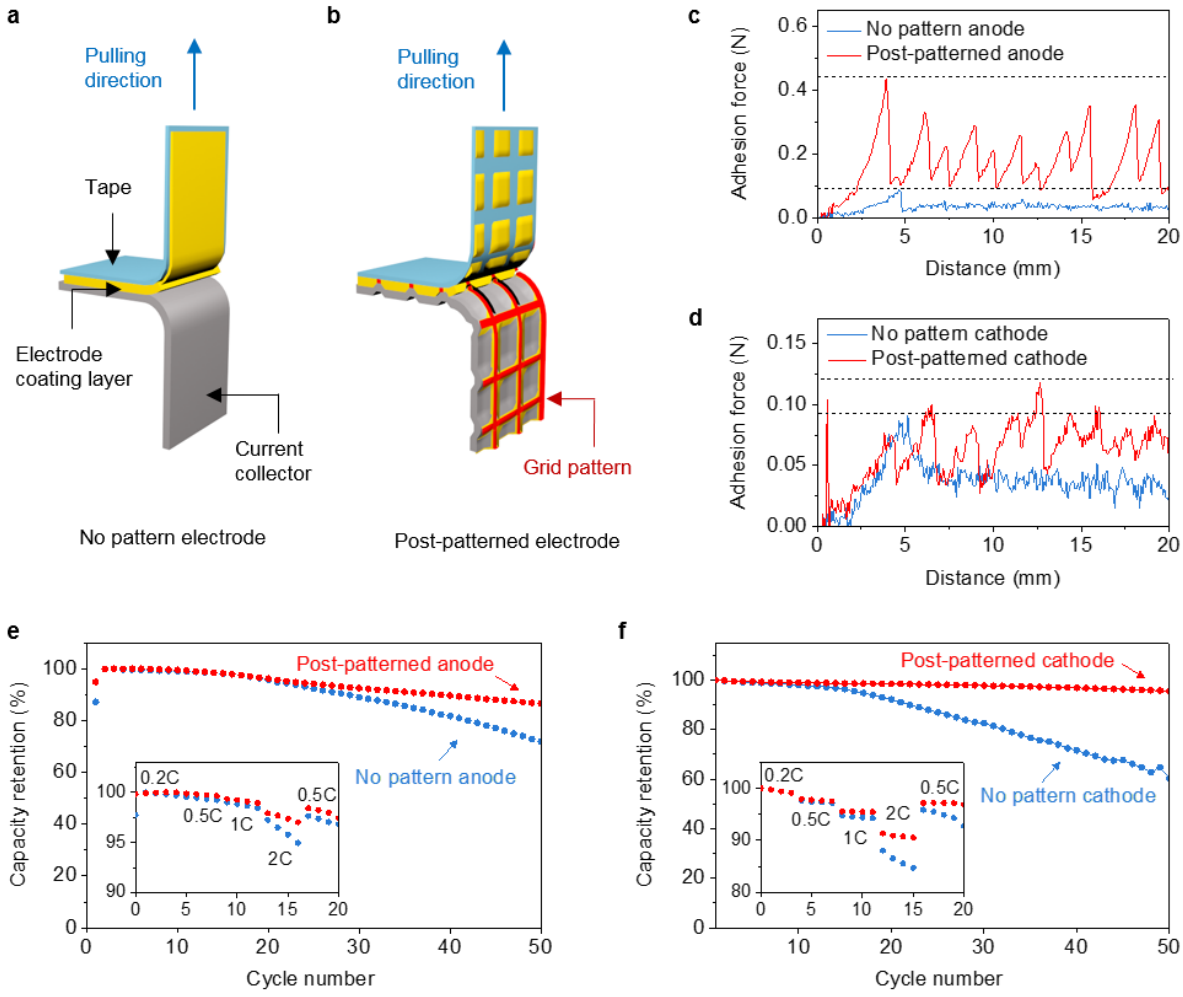

Figure 17. Adhesion force measurements and electrochemical tests. Schematic of 180° peel test applied to (a) no pattern and (b) post-patterned electrodes at a rate of 50 mm min^{-1}. Adhesion force curves for (c) graphite anode and (d) LCO cathode without and with the post-patterning process. Cycle performance of (e) anode and (f) cathode without and with post-pattern, showing discharge capacity retentions reported from 1 to 50 cycles at 0.5C rate. Insets shows the rate capabilities at different C-rates from 0.2 to 2C.

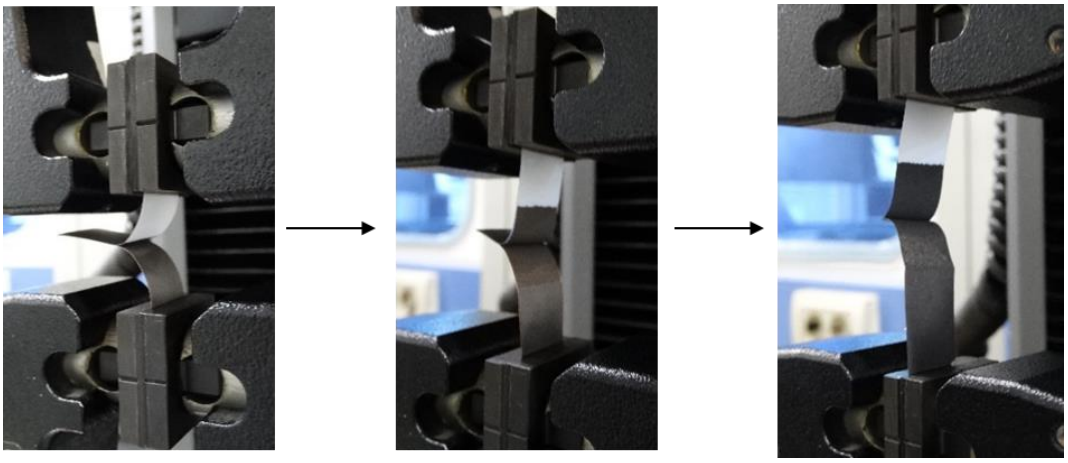

Figure 18. Digital photograph showing adhesion test, where 3M tape was applied onto electrode surface, and it was pulled away from the electrode at 180° to the surface with a speed of 50 mm min^{-1}.

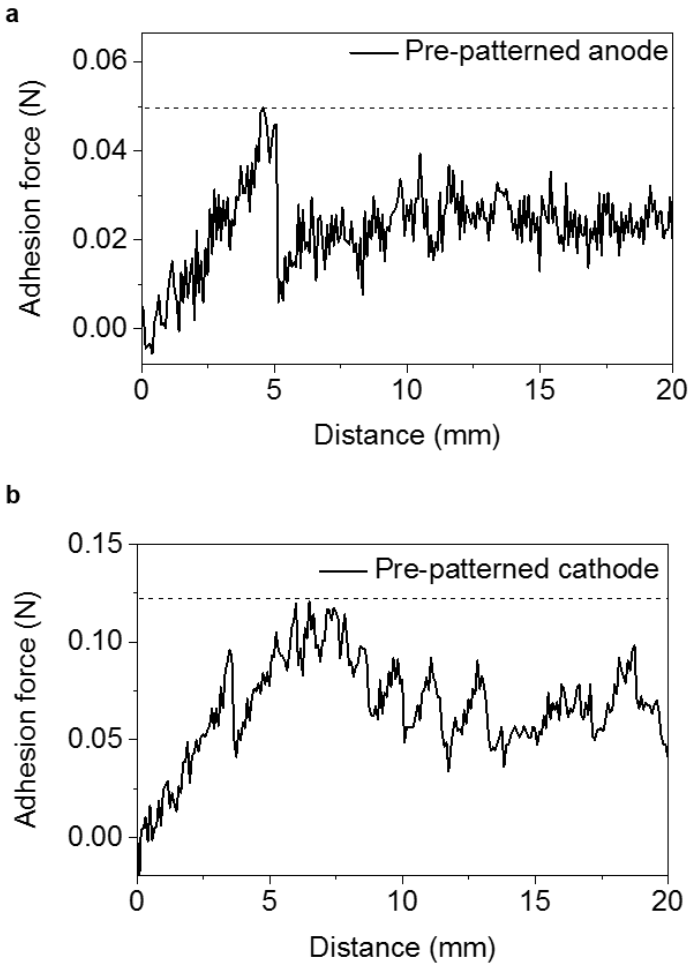

Figure 19. Adhesion force curves for **a**) pre-patterned graphite anode and (**b**) pre-patterned LCO cathode.

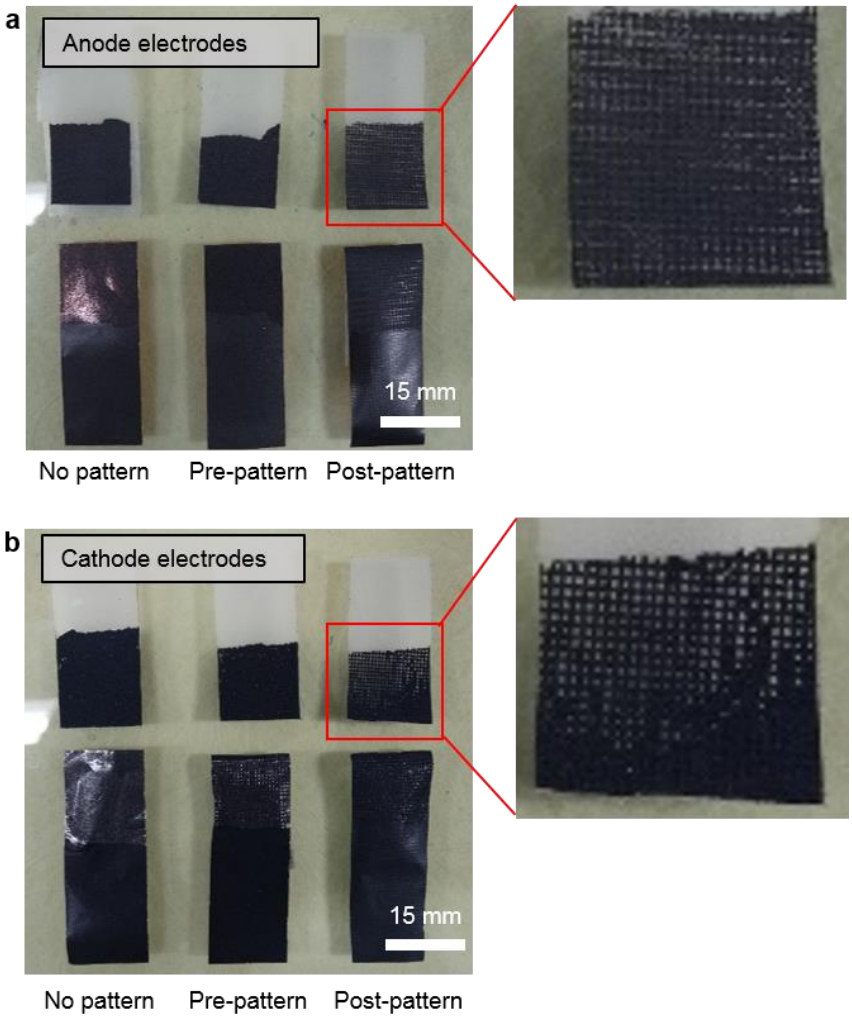

Figure 20. Digital photographs including no pattern, pre-patterned, and post-patterned **a**) anode and **b**) cathode electrodes after adhesion test, where a magnified image represents the peeled-off electrode with unique grid patterns remained on adhesive tape.

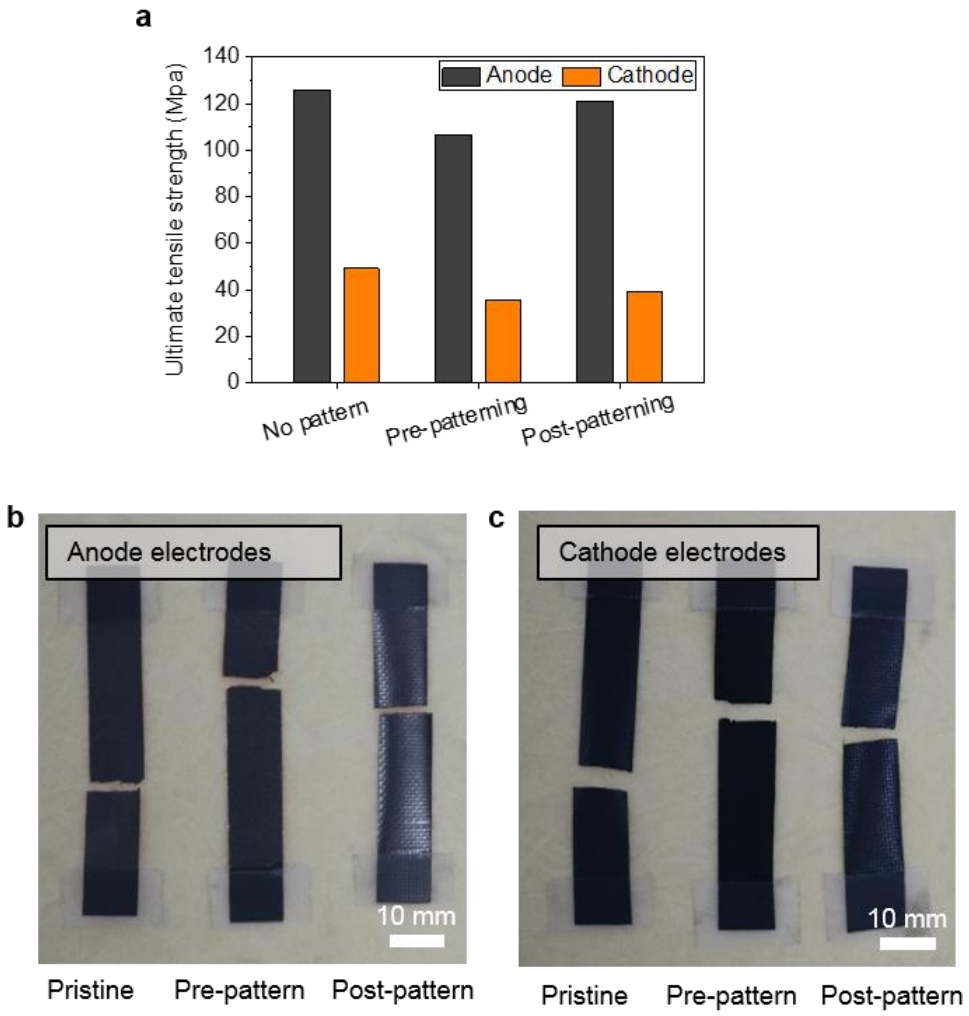

Figure 21. a) Ultimate tensile strength of no pattern, pre-patterned, and post-patterned anode and cathode electrodes, and digital photographs of b) anode and c) electrode after the test.

To investigate the effect of the postpatterning on graphite and LCO electrodes, the electrochemical performance was tested using a half-cell with Li metal as a counter electrode. The initial voltage profile of the postpatterned anode from 0.05 to 1.5 V was similar to that of other samples, exhibiting a discharge capacity of ≈350 mAh g−1 during the first cycle (Figure 22a). The postpatterned cathode also showed a well-defined voltage profile from 3.0 to 4.45 V, and the initial discharge curve (≈183 mAh g−1 during the first cycle) matched the results obtained from the nonpatterned and prepatterned cathodes (Figure 22b). However, as the number of cycles increased, the gap in discharge capacity retention between the postpatterned electrode and other samples gradually increased, with a stable cycle performance emerging in both the anode (≈86%) and cathode (≈95%) after 50 cycles (Figure 17e,f). Moreover, the rate capability of the postpatterned electrode substantially improved as the C-rate increased from 0.2 to 2 C. However, the prepatterned electrodes showed poor electrochemical performance (Figure 23). Overall, the capacity retention upon cycling was proportional to the adhesiveness of the prepared electrodes, thereby demonstrating that the intensively pressed grid pattern can improve the cycle stability and rate capability. These results may be attributed to the increased contact area between active materials and current collectors, as well as the reduced interparticle distances between particles after postpatterning.

The porosity of electrode is closely related to the electronic conduction and mass transport kinetics in LIBs.[96] For instance, as the electrode mass loading density increases, the electrical conductivity improves owing to increased particle- to-particle contact, resulting in the decrease of overall cell resistance. However, a high mass loading density of electrodes with a low porosity can cause poor electrolyte wettability, thus decreasing the ionic conductivity.[97] Notably, with respect to rate capability, the postpatterning method engenders a synergistic effect between the two above-mentioned parameters that are the inversely proportional relationship. In the postpatterned electrode, interparticle distances in the intensively pressed grid region decreased, as shown in Figure 15a,b. On the other hand, the active materials in the nonpatterned concave parts still maintained a high porosity, thus allowing the electrolyte to easily penetrate into the empty spaces (Figure 15c). Accordingly, we suggest that the selectively pressed grid pattern (with densely packed active materials) lends itself to current distribution on the electrode surface at a high rate, while the nonpatterned parts (with a porous structure) engender the electrolyte wetting property that results in efficient Li-ion transport.

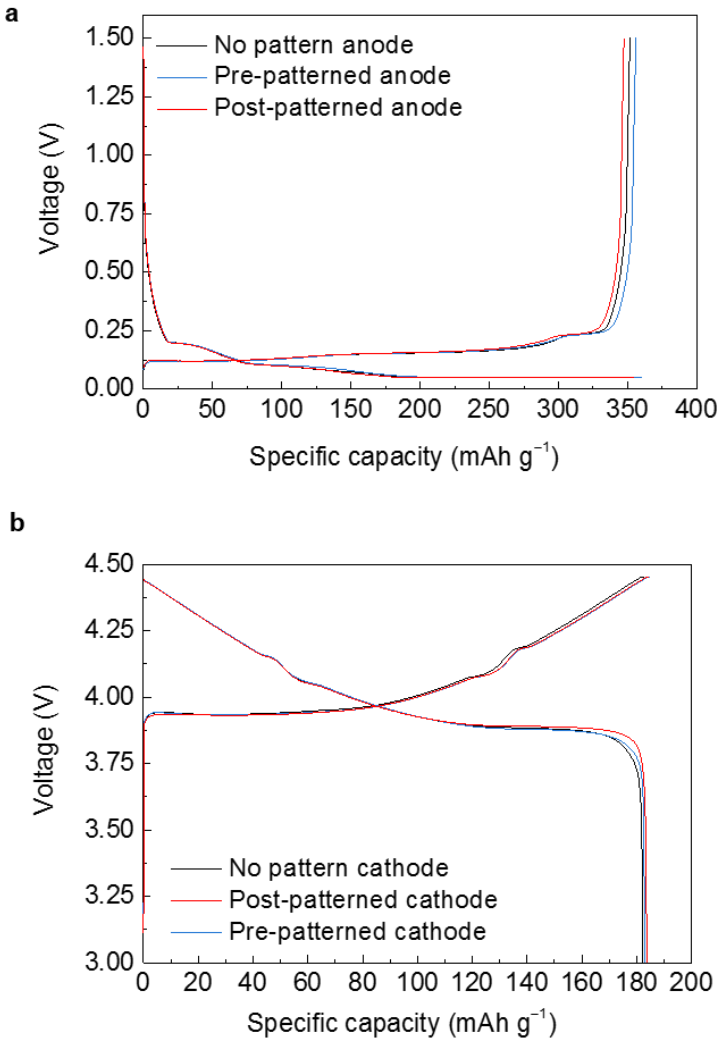

Figure 22. Voltage profiles of no pattern, pre-patterned, and post-patterned **a**) anode and **b**) cathode electrodes at a current rate of 0.5C.

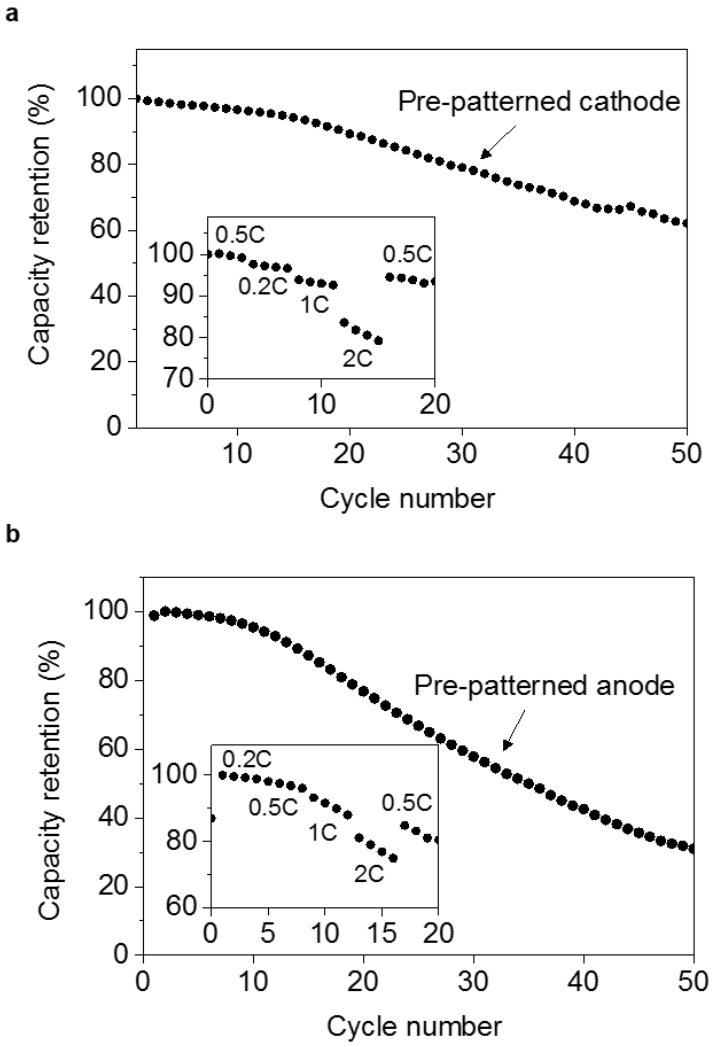

Figure 23. Cycle performance of the pre-patterned (**a**) cathode and (**b**) anode, showing discharge capacity retentions reported from 1 to 50 cycles at 0.5C rate. Insets shows the rate capabilities at different C-rates from 0.2 to 2C.

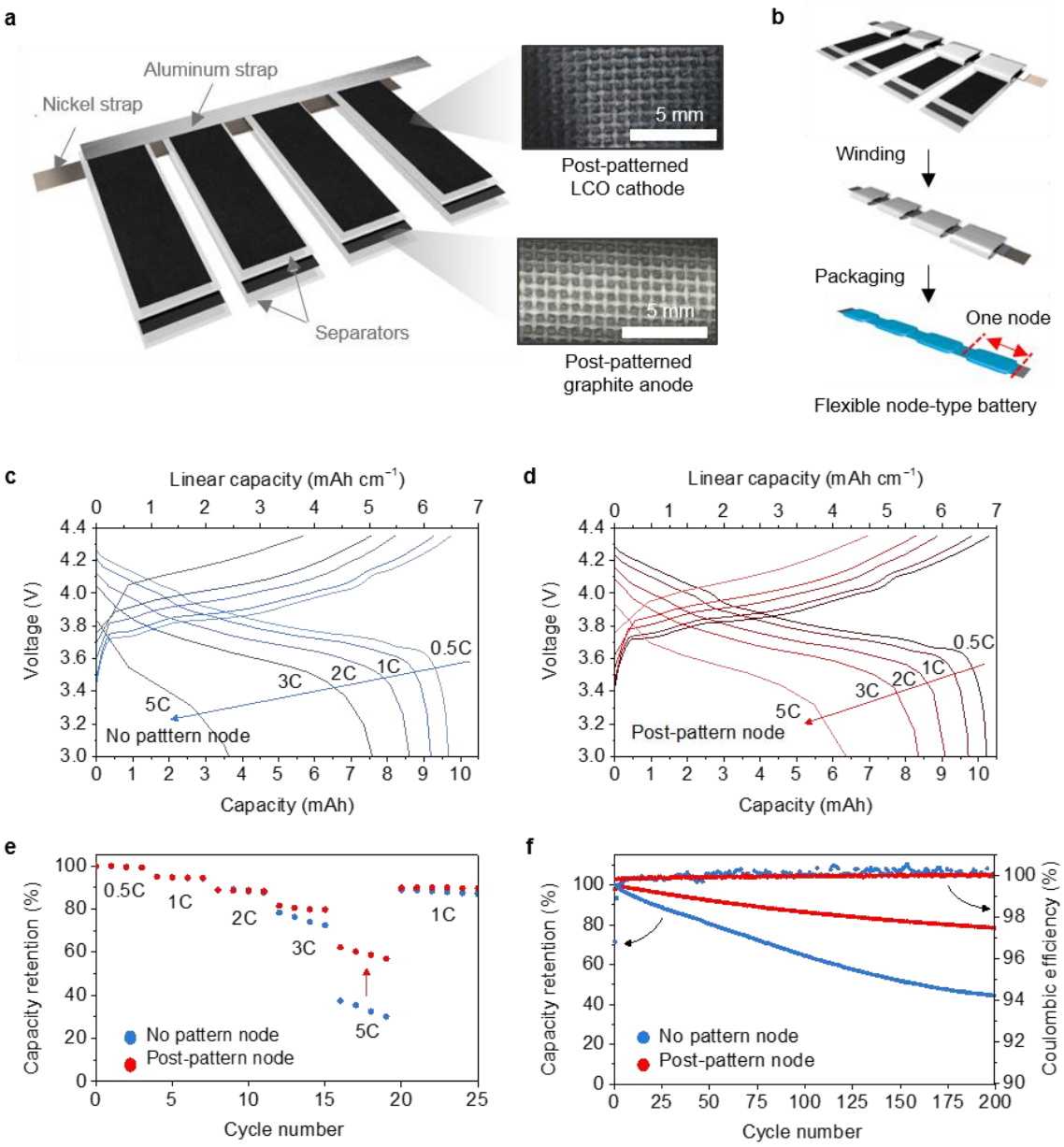

Figure 24. Node-type cell assembly and full-cell performance. (a) Schematic of the node-type LIBs components, showing digital photographs of the post-patterned LCO and graphite electrodes, respectively, and (**b**) cell-assembly process, showing that each planar electrode can be wound and packaged as a node cell. (**c, d**) Voltage profiles of the node-type cell with and without post-patterned electrodes at different rates from 0.5 to 5C. (**e**) Rate capability of the node-type cell with and without post-patterned electrodes, showing charge capacity retention at different rates from 0.5C to 5C, and (**f**) their long-term stability test over 200 cycles at a rate of 1C.

We constructed node-type LIBs (see Figure 24a,b), using postpatterned LCO cathodes and graphite anodes, where each electrode showed apparent grid patterns. These electrodes were carefully welded and densely wound on metal straps in series (Figure 11). It should be noted that we divided the battery into energy storage sections and deformable sections; and this approach was similar to island-bridge design concepts.[98] When intensely winding and folding the electrodes, the electrode coating layers can easily become delaminated from the metal substrates, resulting in severe capacity loss.[53, 80] However, in the postpatterned electrodes, it is expected that a stable cycle performance can be possibly achieved owing to the intensively pressed grid pattern with its improved adhesion force. For comparison, we prepared node-type full cells with and without postpatterning process; the initial voltage profiles were almost identical (Figure 25). At various C-rates ranging from 0.5 to 5 C, the postpatterned node provided a better rate capability compared to the nonpatterned node (Figure 24c,d). The node-type LIBs achieved high energy density per unit length (derived from length of a node). The linear capacities of the postpatterned node were ≈6.9 and 4.2 mAh cm−1 at 0.5 and 5 C rates, respectively. As shown in Figure 24e, the postpatterned node was capable of preserving a discharge capacity retention of ≈80% at a 3 C rate and even ≈60% at a 5 C rate because of the effective current distribution on the grid pattern. Figure 24f shows the cycle performance and Coulombic efficiency (CE) for 200 cycles at a rate of 1 C. It should be noted that we did not use any electrolyte additives or pretreated active materials. As shown in Figure 24f, there was severe capacity fading in the nonpatterned node with unstable CE values. This result could be ascribed to a weakened adhesion force between the coating layer and current collector. Moreover, the increased contact distances between active materials that result from volume expansion upon cycling could cause a capacity degradation because of increased internal cell resistance.[99] However, the discharge capacity of the postpatterned node was more stable for 200 cycles (≈79% of the original capacity) than that of the nonpatterned node (≈45% of the original capacity) at a 1 C rate, and the CE remained stable with good reversibility (>99.5%). This enhanced cycle stability can be explained in terms of the mechanically stable electrode coating layer on metal substrate that results from the postpatterning process.

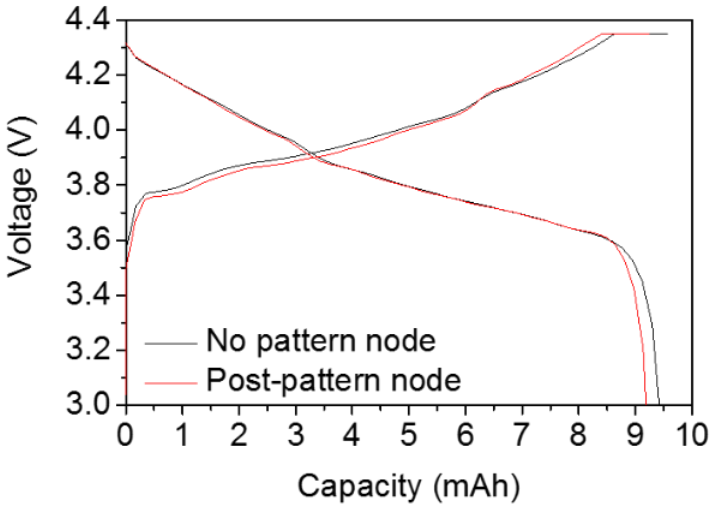

Figure 25. Voltage profiles of the node-type cell with and without post-patterned electrodes during the first cycle at 0.5C rate.

To gain a better understanding of the internal resistance, the node-type full cells were subjected to a direct current internal resistance (DCIR) measurement as the pulse current was increased for 10 s (Figure 26). The DCIR values before cycling and after 150 cycles were summarized in Table 1. Although the initial DCIR values were similar with non- and postpatterned nodes, a large difference was observed after 150 cycles. The nonpatterned node showed highly increased DCIR values from 3.68 (3.56) to 11.76 Ω (12.76 Ω) during the charge (discharge) process; this increasing cell resistance could deteriorate the long-term cycle performance. On the other hand, the DCIR values of the postpatterned node increased from 3.17 (3.14) to 5.56 Ω (5.98 Ω) during the charge (discharge) process, which was much lower than that of the nonpatterned node. The improved cycle stability and rate capability of the postpatterned node can be attributed to the unique grid patterns on the electrodes, which are associated with a high adhesion force and low internal resistance, and will be discussed in detail later in the paper.

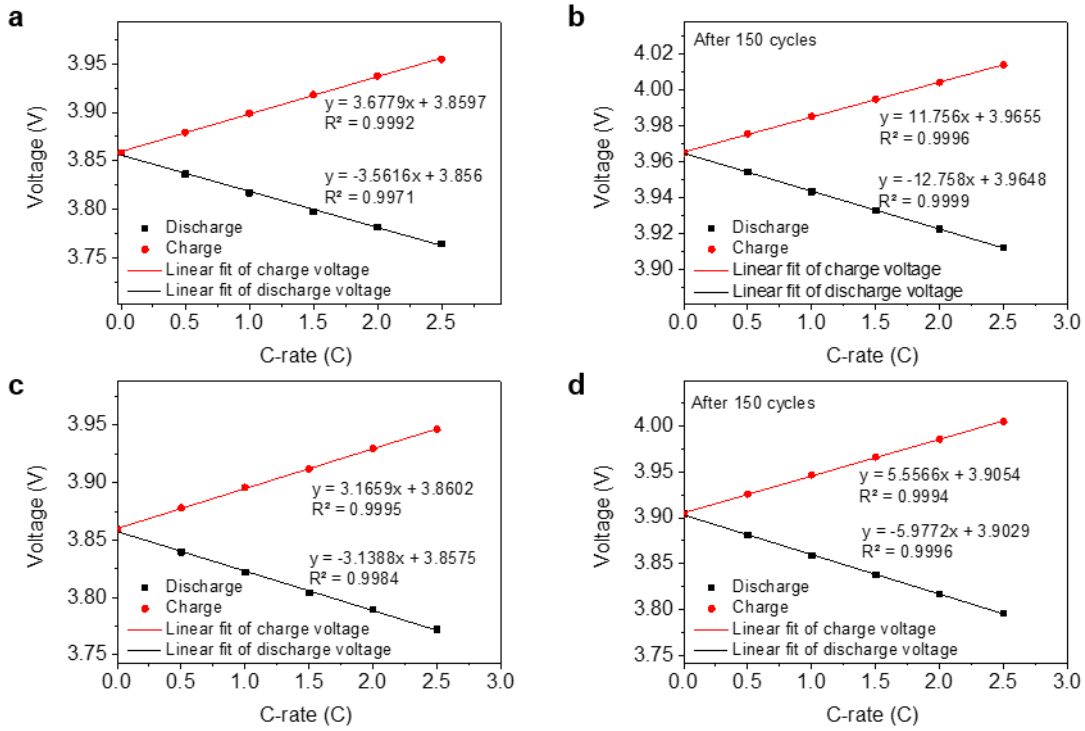

Figure 26. Plot of the voltage vs C-rate for no-pattern node a) before cycling and b) after 150 cycles. Plot of the voltage vs C-rate for post-patterned node a) before cycling and b) after 150 cycles. Pulse current was applied as increasing the current rate from 0.5C to 2.5C at state of charge (SOC) of 50 %, and pulse duration was10 seconds.

Table 1. Summary of DC-IR values obtained at Figure 26.

	DCIR [Ω]			
	Before cycling		After 150 cycles	
	Charge	Discharge	Charge	Discharge
No pattern node	3.68	3.56	11.76	12.76
Post-patterned node	3.17	3.14	5.56	5.98

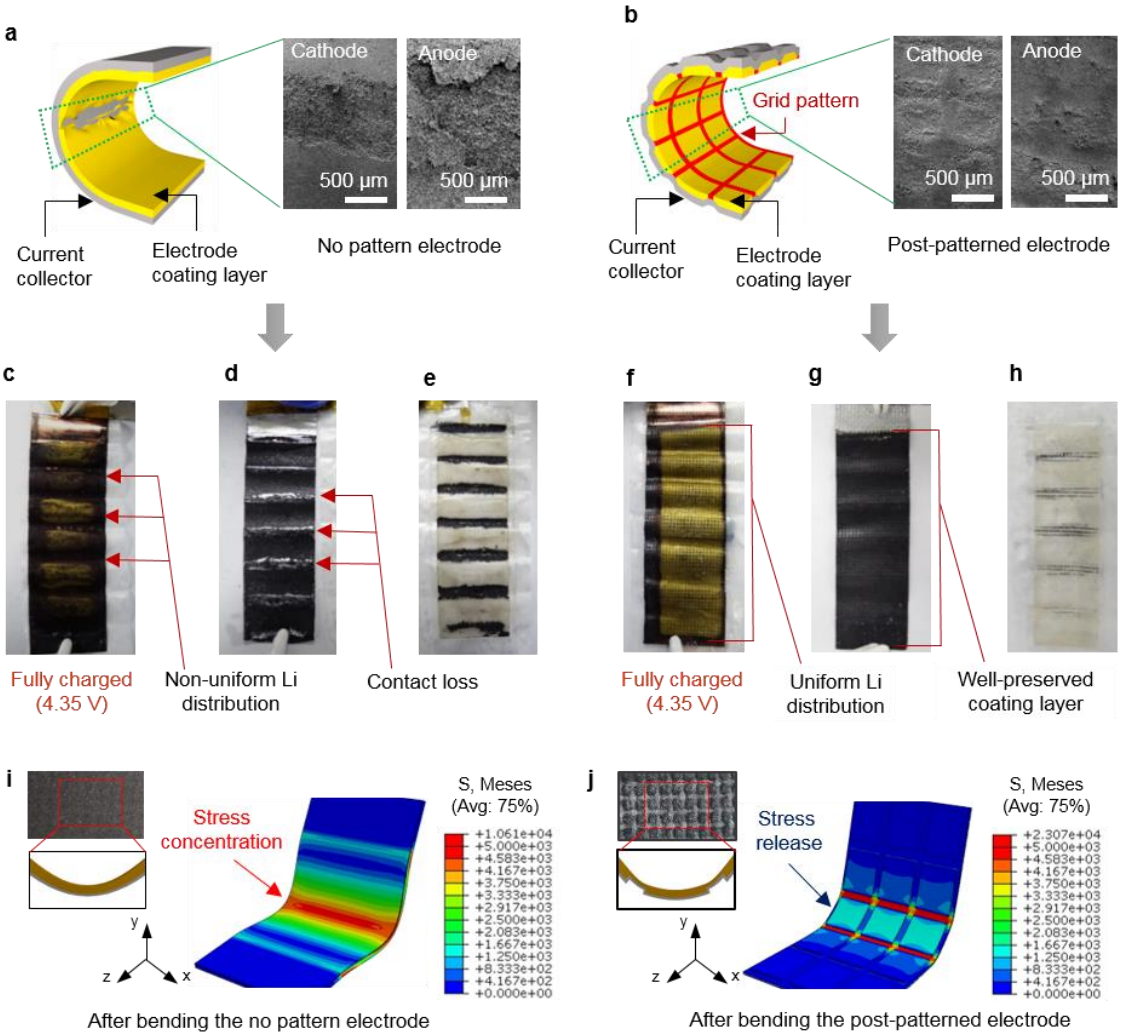

Figure 27. Node-type cell disassembly and finite element analysis (FEA). Schematic of the deformed electrodes of (a) no pattern and (b) post-patterned electrodes, showing their SEM image of the LCO and graphite coating layer after 200 cycles. Disassembled no-pattern node cell after fully charged to 4.35 V, showing (c) anode, (d) cathode, and (e) separator, respectively. Disassembled post-pattern node cell after fully charged to 4.35 V, showing (f) anode, (g) cathode, and (h) separator, respectively. (i, j) FEA results representing the deformation and von Mises stress distribution, where the photographs show the target symmetry without and with post-patterning, respectively.

To provide further insight into the effect of the postpatterning on the electrochemical performance, the node-type LIBs were disassembled after 200 cycles. When electrodes were intensively wound on the metal strap as a node, a high stress could be concentrated on the edges (almost folded state). As shown in Figure 27a, the bent surface of the nonpatterned node exhibited delaminated active materials in both the LCO cathode and graphite anode. However, an intact surface morphology with grid pattern was observed in the postpatterned node (Figure 27b). Further, the node-type LIBs were fully charged to 4.35 V to investigate the surface states of lithiated graphite (LiC6), which could reveal the information regarding capacity loss after cycling.[100] Figure 27c shows the anode surface of the nonpatterned node, wherein a nonuniform Li distribution was observed. This implied that the (de-)lithiation pathway was considerably interrupted during cycling, which may have been caused by external stress and gradual volume expansion of the cell.[99] In addition, the cathode active materials were easily detached from the separator (Figure 27d,e). Compared to these results, a clear gold color with fully lithiated graphite was confirmed from the postpatterned node, and lithium plating on the graphite anode was not observed (Figure 27f). Cathode materials were also well preserved on the current collector with little residue in the separator (Figure 27g,h). These results suggest that the postpatterning can mitigate the stress concentration by distributing tension, resulting in the stable adhesion of the electrode coating layers after long-term cycling.

This hypothesis is also supported by finite element analysis (FEA), which was performed using the commercial package ABAQUS. The target shape and area for the simulation after the deformation of electrodes with and without postpatterning are presented in Figure 27i,j, respectively. Additionally, the von Mises stress distribution (normalized by the Young's modulus) is mapped onto the deformed electrode surface. When applying a load on the nonpatterned electrode, the stress was focused on a bending-center site, which may induce the delamination of the electrode coating layer. By way of contrary, at the same deformation state, the stress on the postpatterned electrode was apparently distributed and released across the grid patterns. The preformed checkerboard network in which densely packed active materials exist can possibly bind an electrode coating layer, thus resulting in the improved cycle stability. Accordingly, this indicates that the postpatterning process is advantageous in distributing the stress concentration when winding or folding electrodes, which agrees well with the experimental data.

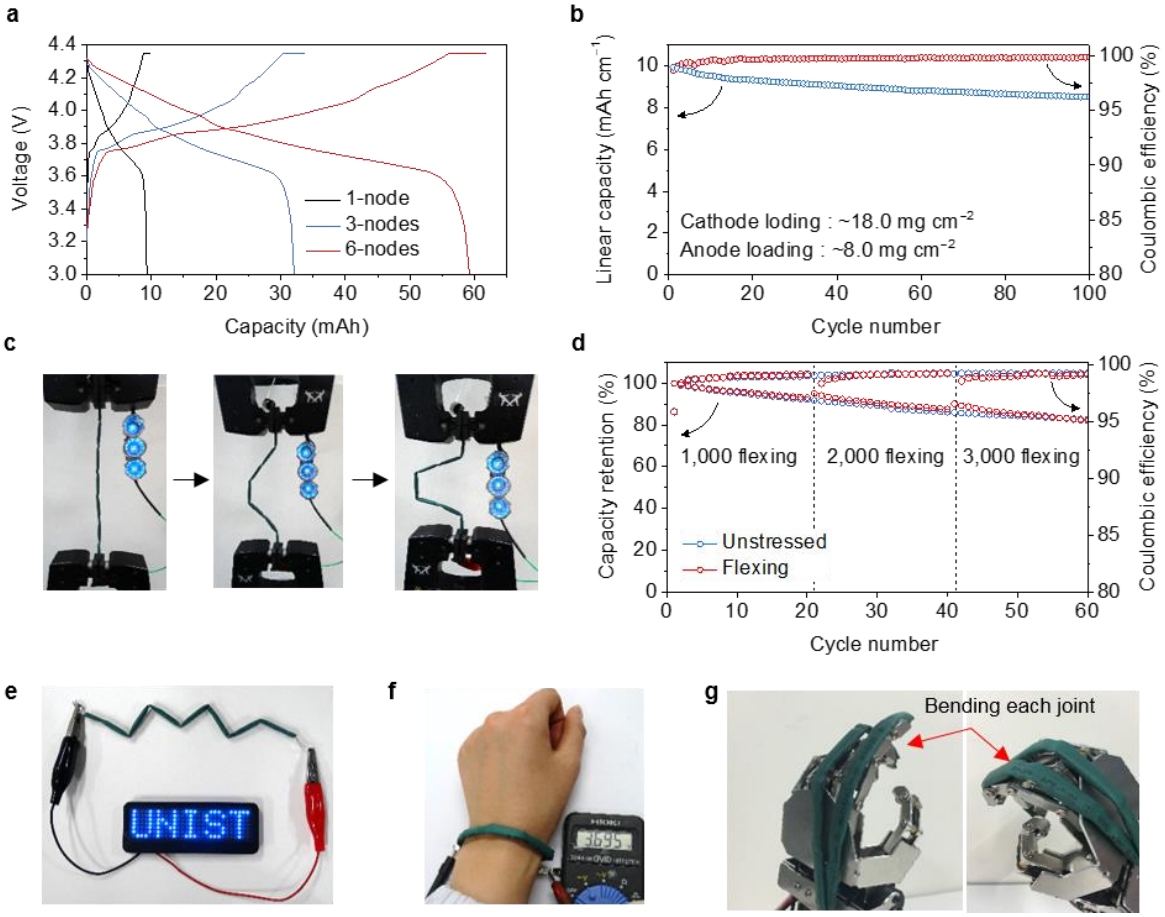

Figure 28. Application of the node-type LIBs. (a) Voltage profiles of the node-type LIBs with the different number of node from 1 to 6. (b) Effect of the post-patterning on high loading level electrodes with cathode and anode loading level of ~18.0 and ~8.0 mg cm^{-2}, respectively, showing linear capacity and its Coulombic efficiency (CE) for 100 cycles. (c) Photographs of a flexing test with powering blue light-emitting diodes (LEDs). (d) Comparison of discharge capacity retention in unstressed and flexing conditions, where the cell was flexed 1,000 times per 20 cycles. Photograph of the flexible node-type LIBs under different deformable conditions, (e) lighting up a blue LED panel in zig-zag state, (f) wearing on the wrist maintaining open circuit voltage (OCV) of ca. 3.7 V, and (g) embedding it on each joint in the robotic hand.

To demonstrate the practical applications of the node-type LIBs, we report on a variety of shapes and deformable states of the batteries. First, we increased the number of nodes to 1, 3, and 6 to verify the linear increase in cell capacity. As expected, the discharge capacities increased proportionally as the number of nodes increased. The initial discharge capacity of the six-node battery was almost two times higher than that of the three-node battery (Figure 28a); these batteries showed a reliable cycle performance for 100 cycles (Figure 29). Next, we applied the postpatterning method to electrodes with a high mass loading, where the cathode and anode loading levels increased from ≈13.3 and ≈5.5 to ≈18.0 and ≈8.0 mg cm−2, respectively. Notably, the node-type battery with high mass loading showed a stable capacity retention for 100 cycles, and its CE was ≈100% (Figure 28b). This cell also showed a volumetric discharge capacity of ≈154 mAh cm−3cell during the first cycle (Figure 30). This result suggests that even at high loading levels, the postpatterning could improve the cycle stability without any chemical treatments. As shown in Figure 28c, the node-type battery with six nodes powering blue light-emitting diodes (LEDs) was subjected to the flexing test. As a result of using segmented cells on the metal strap, the battery provided a high flexibility, allowing the blue LEDs to remain lit constantly. The electrochemical properties of the node-type LIBs with and without flexing cycles appear in Figure 28d. For comparison, the battery was flexed 1000 times before initiating the cycling, as well as after the 40th and 60th electrochemical cycles, at a speed of one flexing cycle per 8 s. Remarkably, the results show no discernible capacity loss after 3000 flexing cycles. By exploiting this capacity for deformation, the present flexible node-type LIBs can be operated under severe bending states, as evidenced by the blue LED panel in Figure 28e. The segmented design of our node-type LIBs was targeted toward wearable and portable electronics. When worn on the wrist, the open circuit voltage (OCV) of the node-type battery can be successfully maintained at ≈3.7 V, as shown in Figure 28f. In particular, the same battery could be embedded in a humanoid robotic hand, which allows it to be flexed along with the bending motion of joints (Figure 28g). By installing the node-type batteries at unused spaces, the room for energy storage devices can be significantly increased in existing electronic devices.

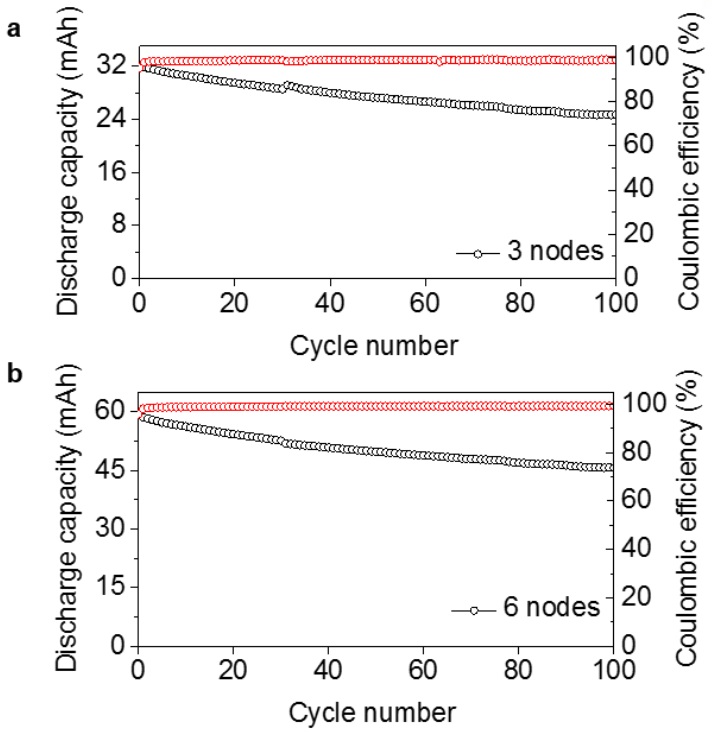

Figure 29. Cycle performance of **a**) 3-nodes and **b**) 6-nodes battery, showing discharge capacity and Coulombic efficiency for 100 cycles at 1C rate.

a

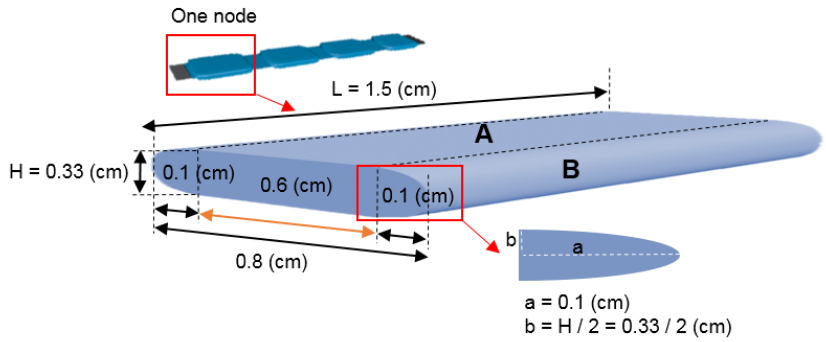

Volume of A;

= H * 0.6 (cm) * L = 0.6 (cm) * 0.33 (cm) * 1.5 (cm) = 0.297 (cm^3)

Volume of two B;

= (π * a * b; area of an ellipse) * L = π * 0.1 (cm) * 0.33 / 2 (cm) * 1.5 (cm) ≒ 0.078 (cm^3)

Total volume

= Volume of A + Volume of two B ≒ 0.375 (cm^3)

b

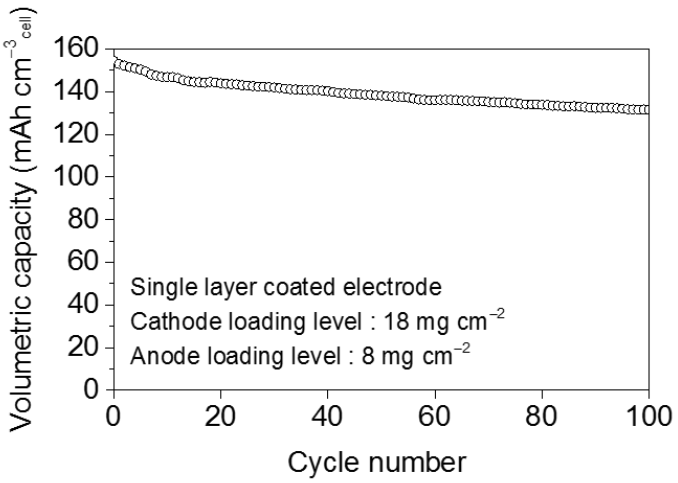

Figure 30. a) Process of calculating a volume of node cell, where the node was simply divided into two sections of A and B. We assumed that height (H) and length (L) of node were 0.33 and 1.5 cm, respectively, and the width of section A was 0.6 cm. The rest of the parts, section B, was calculated by assuming an elliptical boundary. **b**) Cycle performance representing volumetric discharge capacity of the post-pattern node with cathode and anode loading level of ~18.0 and ~8.0 mg cm^{-2}, respectively.

2.4 Summary

We demonstrated flexible node-type LIBs by winding postpatterned electrodes on a metal strap, resulting in a significant improvement in the electrochemical and mechanical properties. After postpatterning, the graphite anode and LCO cathode exhibited excellent adhesion property between the metal current collector and the coating layer, which guaranteed the structural integrity of the node-type cells. The selectively pressed grid pattern enabled a high adhesion force of the electrode coating layers upon battery cycling, thus resulting in enhanced cycle stability and rate capability. In particular, the node-type LIBs with individual segments for the energy storage and the mechanical deformation showed stable electrochemical performance after 3000 flexing cycles. We demonstrated the node-type battery with six nodes in this stage.

In terms of the scale-up, increasing the number of node in series may cause the increase of internal cell resistance. Thus, careful consideration is required before scaling-up for the future application. Furthermore, the postpatterning process may not be limited to graphite or LCO electrodes, and could in fact be readily applied to other electrode materials, such as silicon or germanium anodes. We therefore believe that this study will provide new insights into the design of flexible energy storage devices.

Chapter 3

Lego-like structure for high energy flexible lithium-ion batteries

3.1 Introduction

Rechargeable lithium-ion batteries (LIBs) have been widely recognized as an ideal flexible energy storage medium because of their high volumetric energy density and long cycle life. However, the current LIBs show prismatic or cylindrical shape with rigid encapsulation. These shape is difficult to be applied in the portable and wearable devices. Furthermore, the components of current LIBs electrode such as active materials and metal foil current collector have several limitations for the flexible electronics because of their intrinsic rigid property. When a cell was flexed, traditional active materials such as $LiCoO_2$ (LCO), $LiFePO_4$ (LFP), graphite or $Li_4Ti_5O_{12}$ (LTO) can be delaminated from the metal foil current collector, generating cracks on the electrode surfaces. This eventually causes particle isolation and increases internal cell resistance.

Herein, our unique *Lego-like* 3D block battery was designed to enhance the contact area and adhesion force between cathode and anode with commercialized active materials. The $LiCoO_2$ and graphite electrodes were prepared by slurry coating method with a high loading level of ~20 mg cm^{-2} and 9.5 mg cm^{-2}. Then, the electrodes were stacked with polyethylene separator by conventional cell fabrication process, followed by additional pressing process which yielded a *Lego-like* configuration of the cathode and anode. The square shape patterns with a length of ~500 μm were generated on the both side of the electrodes with opposite direction. This pattern increased the contact area between cathode and anode, demonstrating better cycle performance compared to non-patterned full cell. Furthermore, the *Lego-like* cell was flexed under the fully charged state to investigate the self-discharge behavior. Notably, the *Lego-like* cell showed no appreciable voltage drop of ~30 mV during flexing 5000 times. On the other hand, the non-patterned cell showed severe voltage drop of ~80 mV. For the practical application, the flexible *Lego-like* battery powered the LEDs under the highly deformed state, which was ascribed to the unique cell structure of the *Lego-like* battery. The strongly anchored active materials in the patterns of the counter electrodes prevented the detachment of the active materials and electrode crack, leading to the noticeable electrochemical performance and flexibility.

3.2 Experimental detail

Experimental Section

Preparation of electrodes

Cathode electrode was prepared by casting slurry with 96 wt% active material ($LiCoO_2$, Samsung SDI), 2 wt% super P (TIMCAL) as a conductive agent, and 2 wt% poly(vinylidene fluoride) binder in *N*-methyl-2-pyrrolidione. The slurry was uniformly mixed by homogenizer at 7000rpm for 30min and casted onto the aluminum current collector (15um) with the loading level of 20 mg cm^{-2}. The electrode was calendared to the loading density of ≈ 3.6 g cc^{-1} by a roll-pressing machine. Anode electrode was composed of 93.5 wt% natural graphite (BTR) as the active material, 0.5 wt% Super P (TIMCAL), 6wt% poly(vinylidene fluoride) binder, and 0.2 wt% oxalic acid(Sigma-Aldrich) in *N*-methyl-2-pyrrolidione. The slurry was uniformly mixed at 1500rpm for 20min and casted onto the copper current collector (18um) with the loading level of 9.5 mg cm^{-2}. The electrode was calendared to the loading density of ≈1.6g cc^{-1}.

Lego-like 3D battery fabrication

For fabrication of the *Lego-like* battery, the pouch-type full cells were designed with the N/P ratio ≈1.1. The cathode and anode size were 8mm × 78mm and 10mm × 80mm, respectively. First, the electrodes and polyethylene separator (Celgard) were stacked in the following order: Anode, PE separator, and cathode. The flattened nickel mesh (40-sized mesh) was placed under the assembled cell components. In sequence, One-step 3D patterning process was performed by using the flattened nickel mesh as a template to fabricate the *Lego-like* shape. The gap of the roll-pressing machine was set to be 30um smaller than the total thickness of the assembled cell components and the nickel mesh template. The organic electrolyte of 1.15M $LiPF_6$ in EC/EMC/DMC (2:4:4 vol%) + 2% VC was used.

Electrochemical Measurements

All electrochemical properties were carried out in the voltage window between 3.0 and 4.35V at a 1C rate using a battery cycler (WBCS-3000, WonATech.). Electrochemical impedance spectroscopy (EIS) measurements were evaluated before and after flexing by a potentiostat (VSP-300, BioLogic).

Characterization

The adhesion test of the electrodes was conducted using a universal testing machine (INSTRON Co) with a constant speed of 150 mm min^{-1} to measure the adhesion strength of the coating layer and a current collector. The electrode was attached to the adhesive tape (3M tape) with the same size of 18mm × 35mm. After that, the adhesive tape was removed at an angle of 180°. The mechanical flexing test

was performed at a flexing speed ≈ 10 times min-1 and a 25 radius of curvature using a universal testing machine. In-situ flexing test was also tested while evaluating the voltage of the battery at a 0.1C discharge rate and a flexing speed ≈ 2 times min^{-1}. The surface morphology of the electrodes was investigated using SEM (Verious 460, FEI). The cross-section of the electrodes was prepared using ion-milling system (IM4000, HITACHI).

3.3 Results and discussion

Our unique 3D block cell was designed to enhance contact area and adhesion force between cathode and anode by conventional cell fabrication process, followed by additional pressing process. First, the nickel mesh template was flattened by roll-pressing machine to form square shapes size of ~500 μm (Figure 31). The $LiCoO_2$ (LCO) and graphite electrodes were prepared by a slurry coating method with a loading level of ~20 mg cm^{-2} and 9.5 mg cm^{-2}. The full cells were prepared by stacking prepared electrodes with polyethylene separator, which is conventional full cell assembly process. Finally, the patterning process was carried out at the end of the full cell assembly process via a roll-pressing machine using a prepared mesh template, resulting in a *Lego-like* configuration of the cell (Figure 32, 33a). After patterning, the graphite anode and $LiCoO_2$ cathode showed oppositely pressed grid patterns. As the patterning process was performed at the cathode side, the concave grid patterns were generated on the cathode surface. By way of contrast, the convex grid patterns were shown in the anode surface (Figure 33b, c). The scanning electron microscopy (SEM) images confirmed clear grid patterns on both the electrodes and separators (Figure 33d-f). When the nickel mesh pressed the pre-assembled cell, the surface area could be divided by non-pressed region and intensively pressed region. The SEM images of the selectively pressed cell components were shown in the Figure 34 d-f. Accordingly, the cross-sectional morphology of the electrodes shown in Figure 34 indicates that the loading density was nonuniform because of the grid patterns. The loading density for the intensively pressed region of the cathodes and anodes is of ~ 3.9 g/cc and ~ 1.6 g/cc. Furthermore, we constructed the *Lego-like* full cell which was patterned towards anode direction (Figure 36). The cell could not exhibit its capacity because of the delaminated active materials for the anode (Figure 37). The disassembled full cell after the formation process showed highly delaminated graphite active materials, resulting in blocked pores of the separator. Generally, the patterning process enhances the adhesion force. To demonstrate the physical property of the patterned electrodes, adhesion force was measured by a universal testing machine. The 3M tape was applied on the electrode, where all electrodes were prepared with the same size of 18 mm x 35 mm. The tape was then pulled away from the electrodes at an angle of 180 ° with a constant speed of 150 mm min^{-1} (Figure 37). The regularly patterned electrode lead to an enhanced adhesion force, showing the maximum peak of ~ 0.016 N for the cathode and ~0.045 N for the anode

(Figure 39). This behavior was also consistent with the digital image of the tape after peeling test. The amount of peeled-off electrode coating layer was considerable in the non-patterned electrode compared to patterned electrodes (Figure 40).

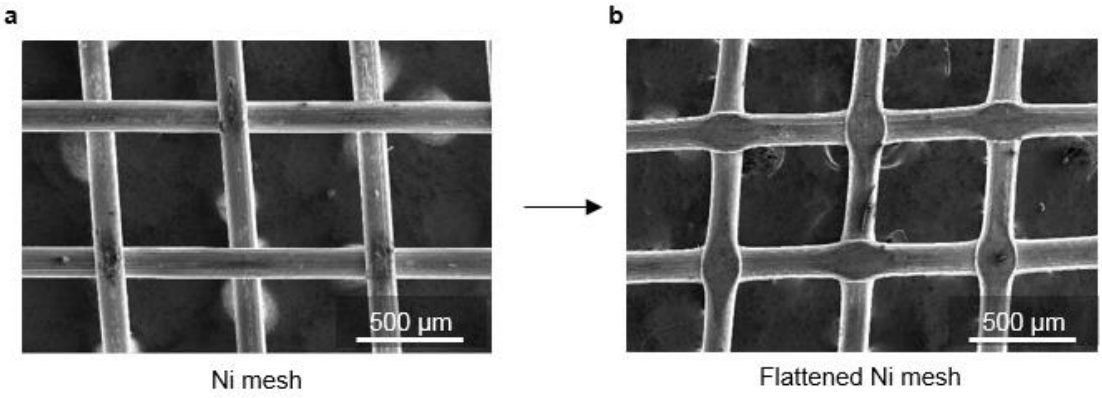

Figure 31. Scanning electron microscopy (SEM) images of a) pristine nickel mesh (40-sized mesh), and b) a flattened nickel mesh as a template.

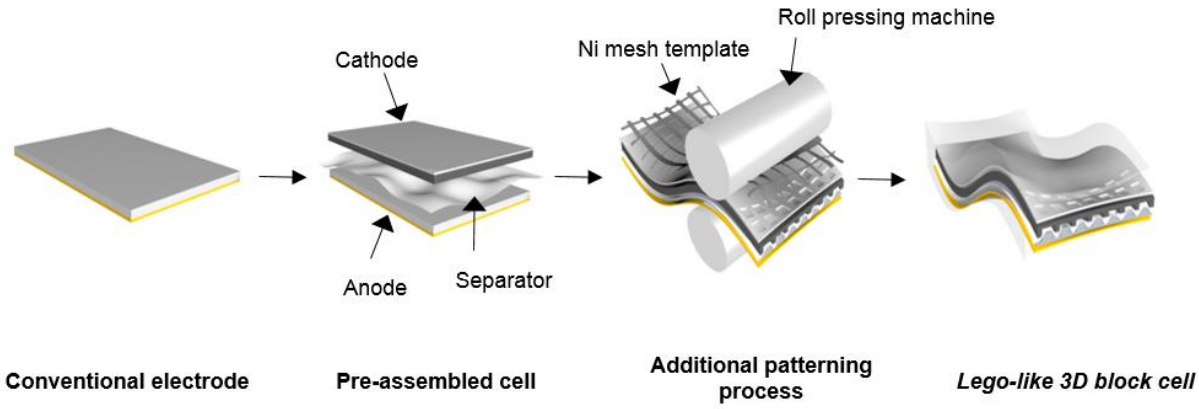

Figure 32. Schematic of the fabrication process for the *Lego-like* 3D block cell.

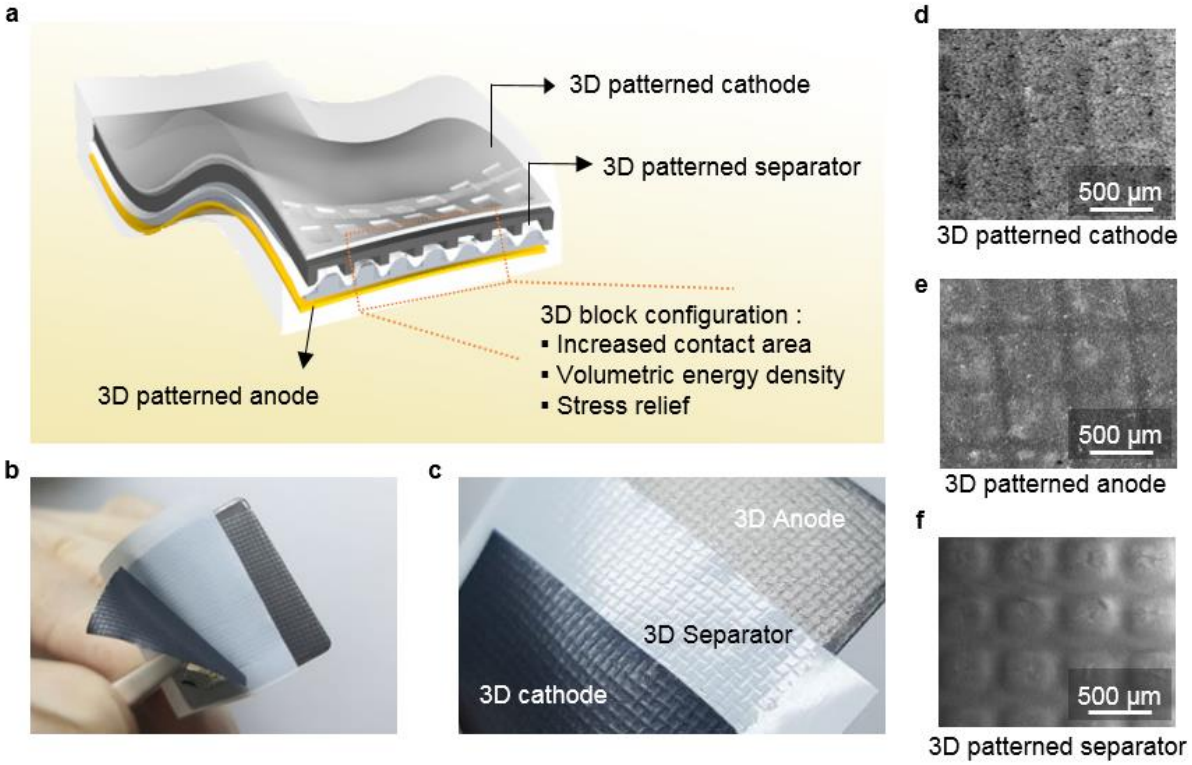

Figure 33. a) A conceptual illustration of the *Lego-like* 3D block battery showing the characteristics of its configuration. Digital photographs of the b) 3D block cell and c) its major components. The scanning electron microscopy (SEM) images of the selectively pressed d) cathode, e) anode and f) separator after patterning process. The graphite anode and $LiCoO_2$ cathode showed oppositely pressed grid patterns.

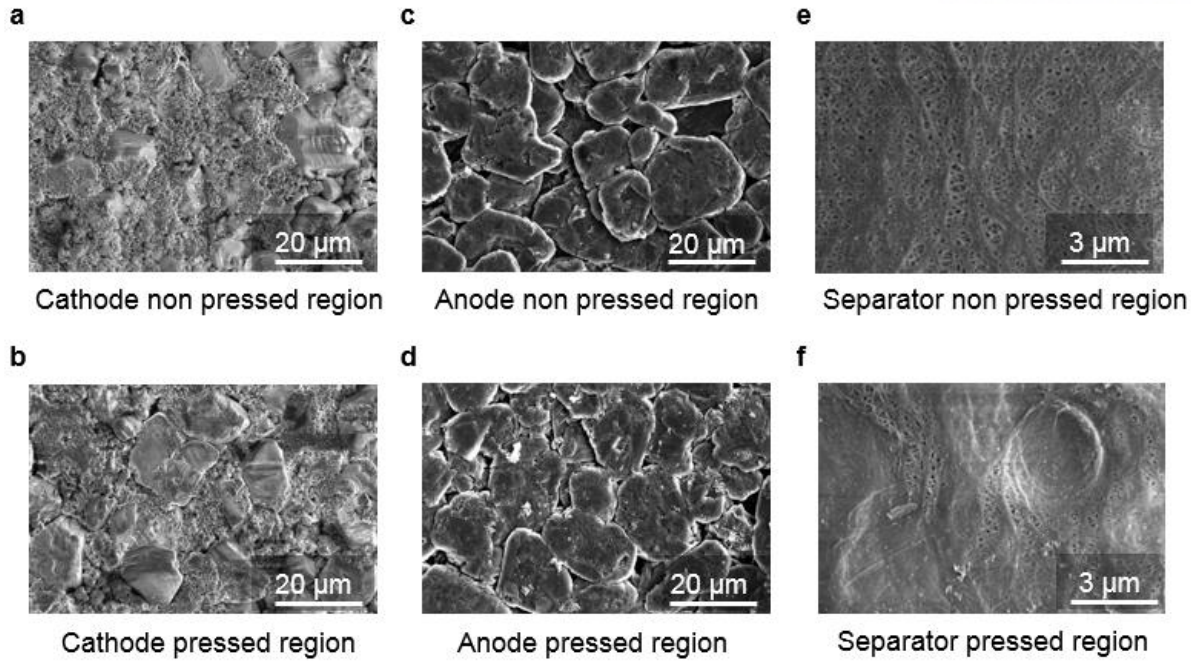

Figure 34. SEM images of a surface morphology of a) non pressed cathode, b) intensively pressed cathode, c) non pressed anode, d) intensively pressed anode, e) non pressed separator and f) intensively pressed separator**.**

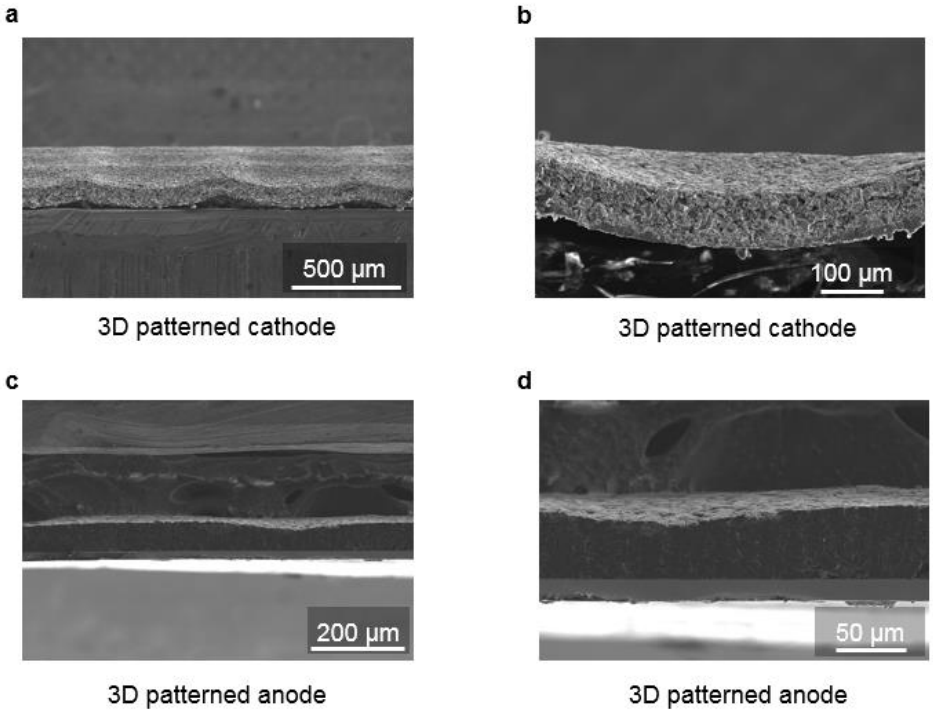

Figure 35. Cross-sectional SEM images of the a) 3D patterned cathode, b) its magnified view, c) 3D patterned anode, and d) its magnified view, showing the selectively pressed grid pattern.

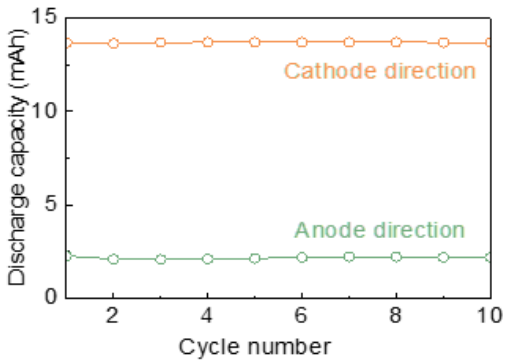

Figure 36. Cycle performance of the *Lego-like* full cell which was patterned towards anode direction and cathode direction.

Figure 37. Digital photograph of the *Lego-like* full cell which was patterned towards anode direction. The delaminated active materials for the anode.

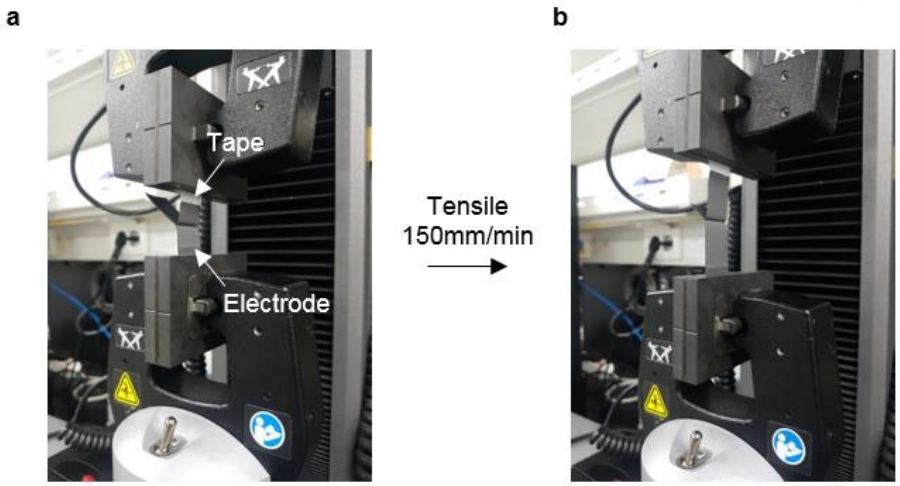

Figure 38. Adhesion force measurements. The tape was then pulled away from the electrodes at an angle of 180 ° with a constant speed of 150 mm min^{-1} using a universal testing machine.

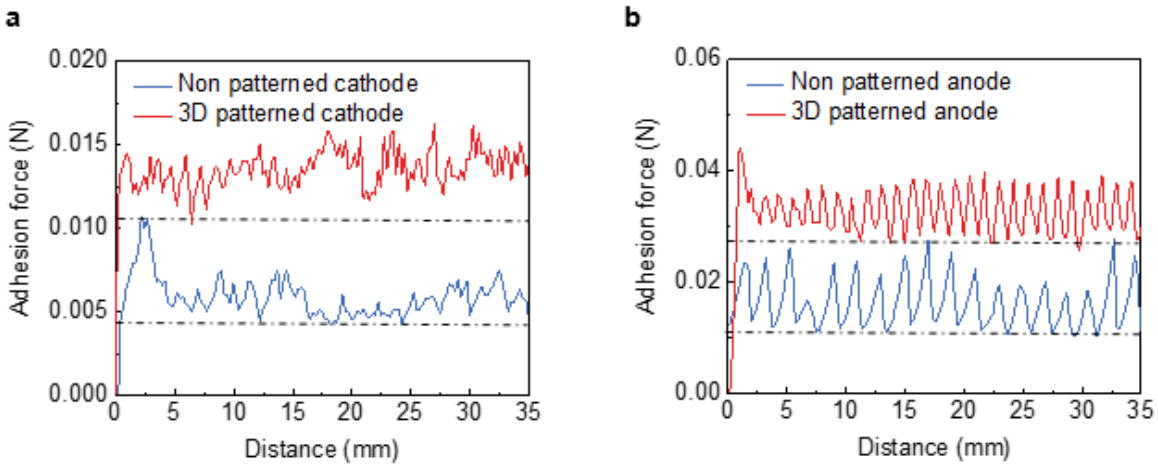

Figure 39. Adhesion force measurement for a) non patterned and 3D patterned cathode and b) anode.

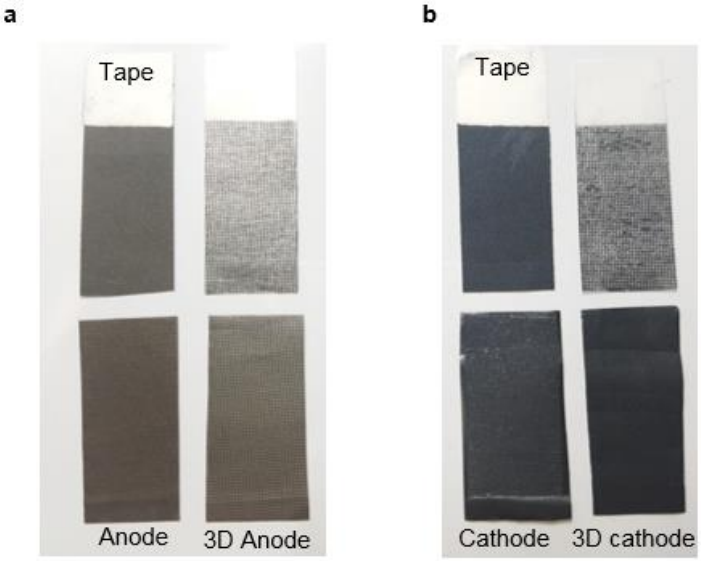

Figure 40. Digital photographs of a) anode and b) cathode electrode after the adhesion test.

The conventional LIB cell consists of stacked electrodes and separator; thus, each component has different mechanical strength. As a result, the crack formation and contact loss could be generated upon repeated flexing test, leading to degradation of the cell. The rigid configuration of *Lego-like* 3D block cell could prevent such issues where the cathode and anode hold each other tightly. The oppositely formed grid pattern on the electrode well distributed the stress and mitigated the delamination of electrode coating layers from the current collectors. The improved mechanical strength of the cell was also explained by the excellent electrochemical performances. The electrodes were prepared with a high loading level to reveal the degradation mechanism clearly under the mechanical stress. To investigate the effect of the 3D block electrode configuration, the non-patterned cell with traditional full cell configuration was also fabricated simultaneously. Both cells were charged galvanostatically to 4.35 V for the formation cycle at a rate of 0.1 C. The voltage profile of 3D block cell and the non block cell was same without showing capacity fading and overpotential (Figure 41). After the formation cycle, each cell was subjected to the long-term cycle test for 200 cycles, where the charge and discharge rates were 1C and 1C. The 3D block cell retained 10% higher discharge capacity than the non-patterned cell presented in Figure 42c. In addition, lower overpotentials were observed in the 3D block cell from the voltage profiles (Figure 42d). This improved cycle performance was ascribed to the excellent adhesion between cell components, such as cathode from anode, electrode coating layers from the current collectors, resulting from the patterning process. In general, patterning increases the surface area and adhesion force between electrode materials. However, rough surface causes the decrease of contact area between anode and cathode. Against this negative effect of general patterning process, our *Lego-like*

3D block cell configuration achieved the increased contact area between the electrodes owing to oppositely formed grid patterns. The patterning process to the pre-assembled cell increased both surface area and the contact area of ~ 4.5% compared to the non-patterned electrode.

To further confirm the cycle stability under the mechanical stress, the flexing test was conducted with a universal testing machine (Figure 42e). The 3D block cell was attached to the PVC substrate to maintain constant flexing radius of ~ 25 mm and the speed of ~ 10 times min−1. The 1000 times flexing was repeated in the intervals of 20 cycles, where the charge and discharge rates were 1C and 1C. The capacity retention for the *Lego-like* 3D battery after 4000 times flexing and 100 cycles was ~ 80%, and the non-patterned cell was ~ 50% (Figure 42f). This result demonstrates the *Lego-like* 3D block structure was well maintained without shifting of electrodes or contact loss between materials upon flexing.

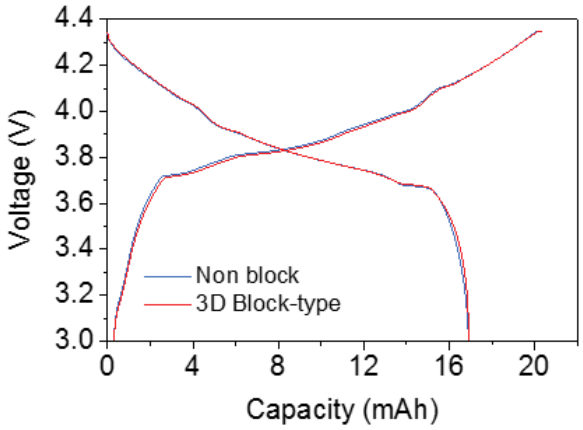

Figure 41. Voltage profiles of the cell with and without 3D patterned electrodes during the first cycle at 0.1C rate.

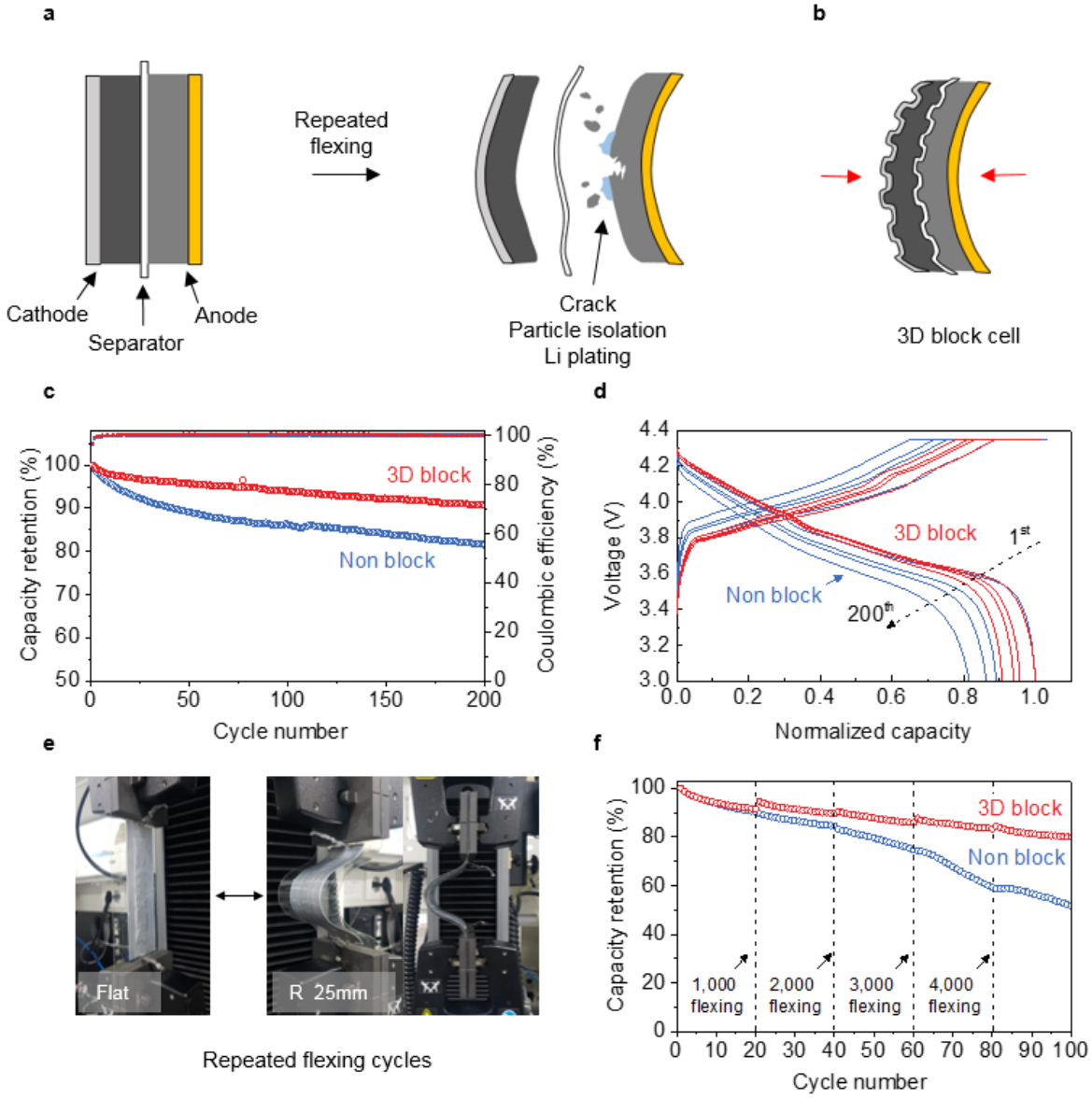

Figure 42. Electrochemical performance and mechanical flexing tests. Schematic of a) the non block cell and b) 3D block cell under mechanical stress. and c) their long term cycle stability over 200 cycles at a 1C rate and voltage window from 3.0 to 4.35 V. d) Voltage profiles showing normalized discharge capacities of the non block cell and the 3D block cell from 1, 50, 100 and 200th cycles. e) Digital photograph of mechanical flexing tests with a flexing radius of ~25 mm. f) Discharge capacity retention of the non block and 3D block cell, where the cell was flexed 1000 times in the intervals of 20 cycles.

To better understand the excellent cycle performance and flexibility, electrochemical impedance spectroscopy (EIS) was conducted with respect to the various charge states for non-patterned cell and *Lego-like* cell. The 5000 times flexing at the state of charge (SOC) for 0, 50, 100% was conducted before and after 20 cycles of electrochemical cycling. The capacity retention for the non-patterned cell was 82%, 57% and 45% when the cell was flexed at SOC 0, 50, 100% (Figure 43a). The results indicated that the degradation of the cell severely occurs as the SOC condition becomes higher. However, the noticeable results were shown in the *Lego-like* cell. The *Lego-like* 3D block cell demonstrated excellent mechanical and electrochemical properties regardless of the state of charge (Figure 43b). The 3D block cell showed no discernable capacity loss although the flexing was conducted at the SOC 100%, maintaining 90% of initial discharge capacity.

To provide further insight into the effect of the *Lego-like* 3D block structure, the full cell was disassembled after 5000 flexing. The EIS tests were carried out after disassembled electrodes were reassembled to half-cell, as presented in Figure 43c-d. The noticeable increase of resistance was not observed for the cathode and anode of 3D block cell. Interestingly, there were no significant changes in the cathode upon flexing regardless of patterning. However, both SEI resistance and charge transfer resistance were increased with the SOC condition while flexing (Figure 43d). The reason for increased internal resistance is the exposure of the new surface and contact loss due to the delamination of electrode materials and crack generation during the repeated mechanical flexing. Such problem could arise the formation of new SEI, depletion of electrolyte and Li plating which can be result in degradation of battery performance.

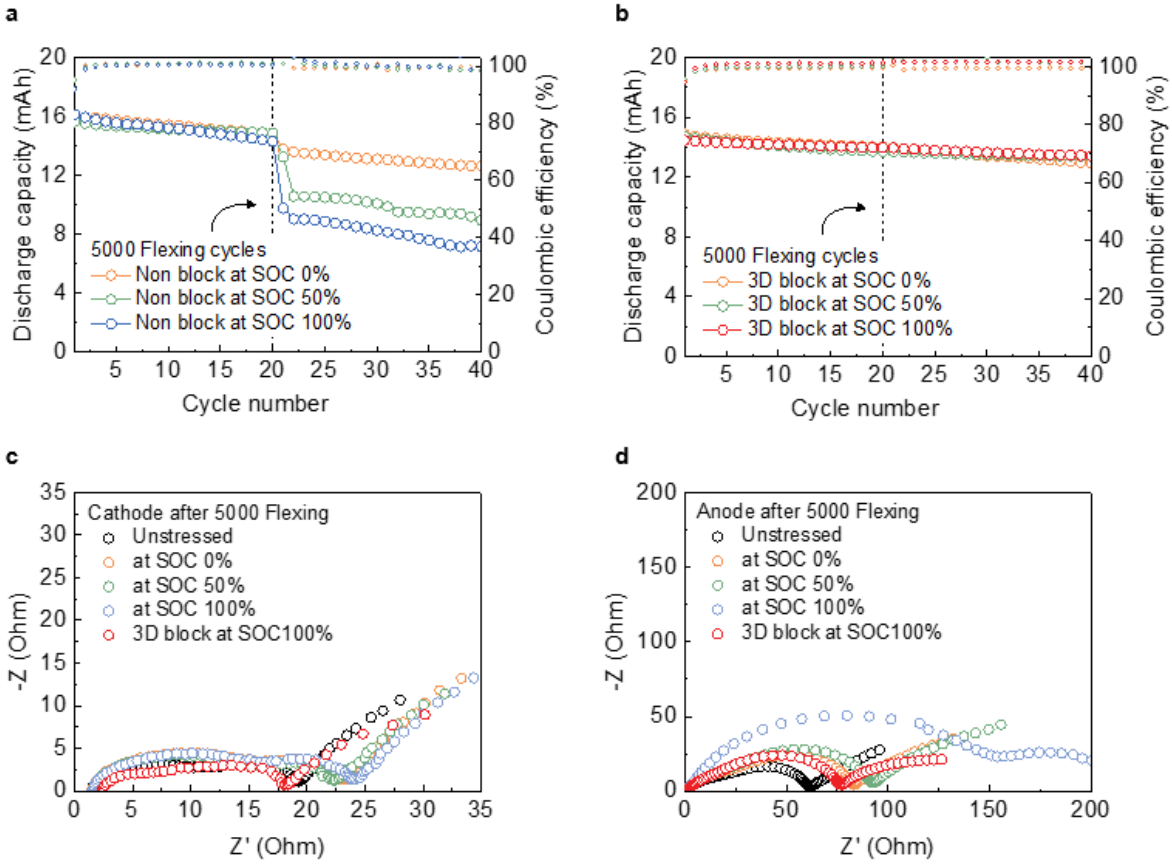

Figure 43. Cycle performance of a) the non block cell and b) the 3D block cell after 5000 times flexing at 0, 50, 100% state of charge (SOC) conditions. Electrochemical impedance spectroscopy (EIS) profiles of c) cathode and d) anode in coin cells of the unstressed sample and samples after 5000 times flexing at 0, 50, 100% SOC conditions.

Table 2. Electrochemical impedance spectroscopy (EIS) results of the disassembled electrodes after 5000 times flexing at 0, 50, 100% state of charge (SOC) conditions.

a

Cathode	Unstressed	at SOC 0%	at SOC 50%	at SOC 100%	3D block at SOC100%
R_s (Ω)	1.59	1.59	1.65	1.53	2.20
R_{film} (Ω)	5.66	10.65	10.27	10.12	5.73
R_{CT} (Ω)	14.84	16.44	19.01	18.74	13.51

b

Anode	Unstressed	at SOC 0%	at SOC 50%	at SOC 100%	3D block at SOC100%
R_s (Ω)	1.69	1.64	1.73	1.98	1.85
R_{film} (Ω)	10.23	10.62	11.15	79.83	10.55
R_{CT} (Ω)	40.85	51.63	58.86	174.27	47.88

Such results indicate that the increased EIS resistance is dominated by the degradation of the anode electrode. To further understand the effect of mechanical stress on the electrodes, we disassembled the non block and 3D block cell which were fully charged to 4.35 V after 5000 times flexing. In figure 44a, the photograph of the non block anode presents the inhomogeneous reaction of lithium on the flexing region. The top-view and cross-sectional SEM image exhibited the delaminated active materials in graphite anode, generating cracks on the electrode surface (Figure 44b-c). This eventually causes particle isolation and increased cell resistance, which could contribute to the formation of lithium plating and lithium dendritic growth at the cracked site. On the other hand, a clear gold color with fully lithiated graphite (LiC_6) was confirmed from 3D block anode homogeneous current distribution (Figure 44d). After flexing tests, the well-preserved coating layer of the 3D block anode can mitigate the stress concentration, resulting in stable adhesion of electrode coating layers.

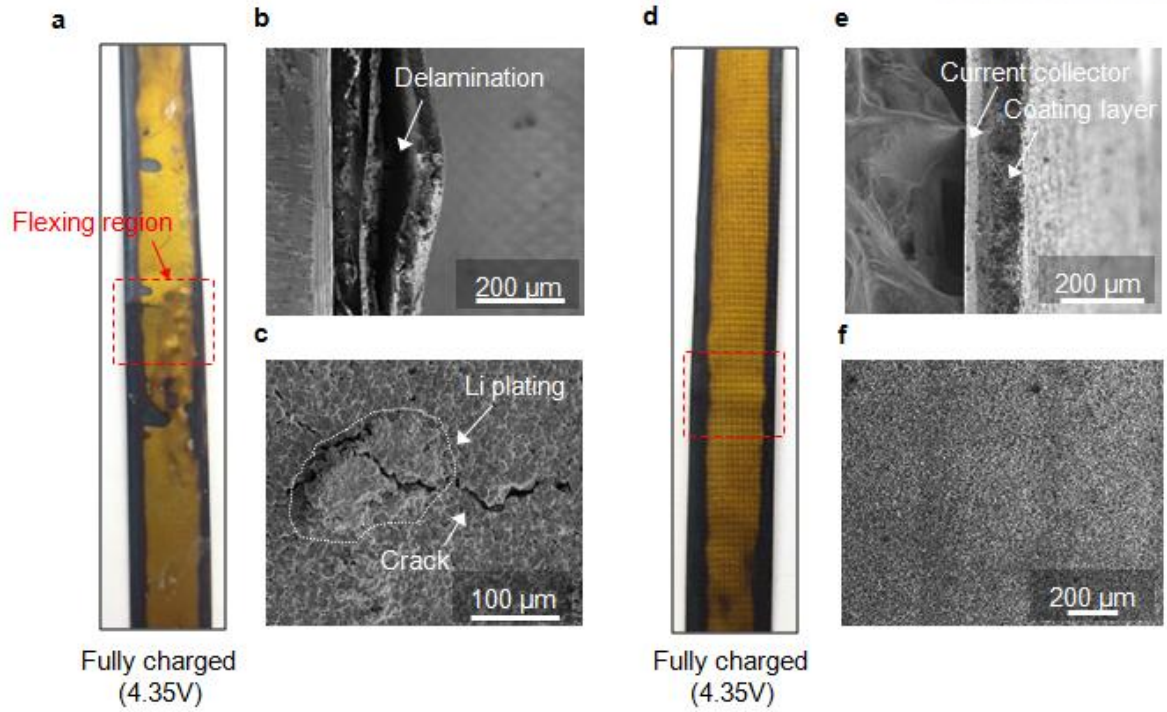

Figure 44. Photographs of the disassembled non block and 3D block anode electrode. a) The non block anode showing nonuniform lithium distribution on the flexing region. Cross-sectional and top view SEM images of b) the non block anode, showing delamination of electrode materials, and c) crack and lithium plating generation on the electrode surface after 5000 times flexing. d) The well-preserved electrode coating layer of the 3D block anode with fully lithiated graphite. e) Cross-sectional and f) top view SEM images of 3D block anode after 5000 times flexing.

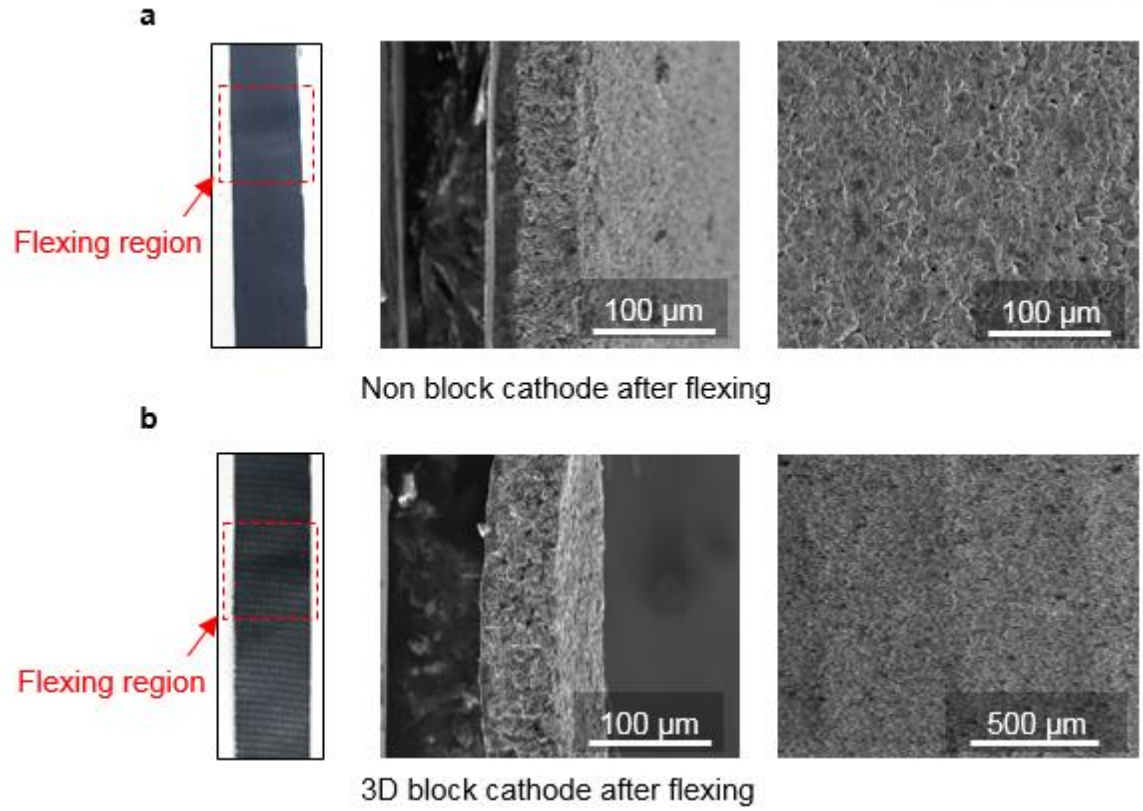

Figure 45. Photographs of the disassembled a) non block and b) 3D block cathode electrode.

Usually, the lithiated graphite electrode suffers from the voltage decay and poor efficiency, however, we found that our rigid *Lego-like* 3D block structure significantly mitigated the voltage decay. Such property was further evaluated by flexing test with 3D block cell and non block cell which were fully charged to 4.35 V (Figure 46a). The voltage was measured during the flexing at a speed of 2 times min^{-1} with the flexing radius of 25 mm. For the comparison, the voltage of the non block cell without mechanical stress was measured at the same time, and it showed little voltage decay from 4.35 V to 4.32 V (black line). Interestingly, the *Lego-like* 3D block cell (red line) demonstrated similar voltage decay with unstressed cell. On the contrary, the non block cell under mechanical stress showed severe voltage decay from 4.35 V to 4.27 V (blue line). [99, 101-102]

To demonstrate the practical application of the Lego-like 3D block battery, *In-situ* flexing tests of the non block cell and 3D block cell were performed during discharge at a 0.1 C rate (Figure 46b). The discharge voltage profiles of the non block cell (blue line) exhibited severe voltage fluctuation during the repetitive flexing cycles with the flexing rate of ~10 times min^{-1} and the discharge process (inset of Figure 46b). Moreover, the Cu current collector was fractured after only 300 times flexing cycles. This implied that the stress was concentrated on the bent site of the non block cell, resulting in a damage. On the other hand, the 3D block cell (red line) and unstressed cell (black line) were similar without showing

voltage fluctuation under the harsh flexing condition. This result can be attributed to the unique *Lego-like* 3D block structure, preventing of the shifting between electrodes and separator upon flexing. Notably, the grid pattern on the 3D patterned electrodes can substantially alleviate the mechanical stress of the cell upon flexing. Additionally, the improved adhesion force of the 3D patterned electrodes contributes to enhance the long-term cycle stability and mitigate the particle isolation and delamination upon flexing cycles.

We designed the blue neon signs for the Ulsan National Institute of Science and Technology (UNIST) to verify the potential in flexible applications. The *Lego-like* 3D block battery powered the blue neon signs after 5000 flexing cycles under deformable conditions (Figure 46c). Furthermore, Figure 46d shows lighted three white lighting the light-emitting diode (LED) connected to the 3D block cell encapsulated with PDMS worn on the wrist. To further demonstrate its flexibility, the twisting properties of the 3D block cell were tested by measuring the voltage drop. As shown in Figure 46e-f, the Lego-like 3D block battery maintained the open circuit voltage (OCV) even under more strict conditions with a radius of curvature, given r = 25, 15, 8 mm. This result implies that the *Lego-like* 3D battery is suitable for constructing flexible electronics according to customer's requirements.

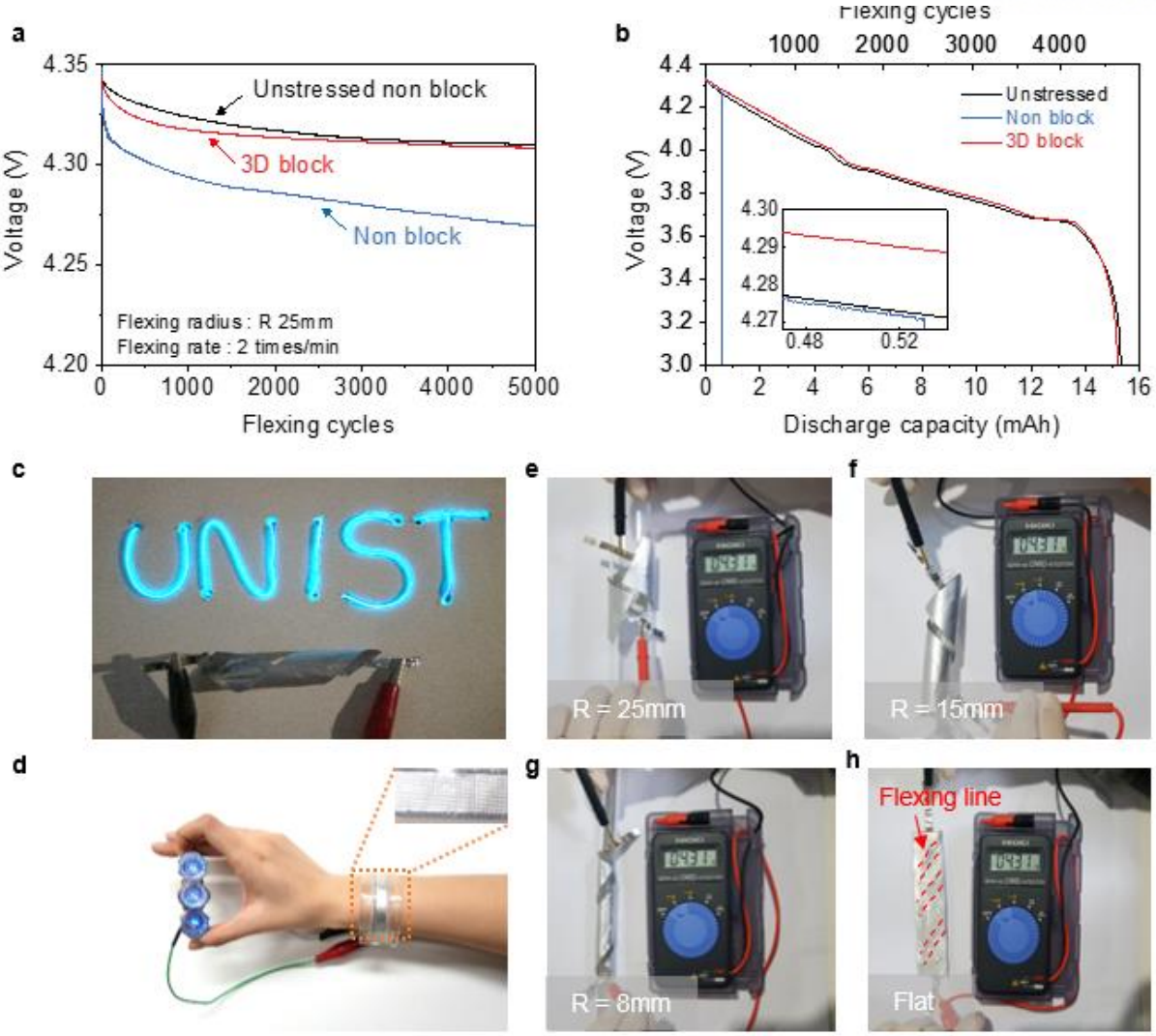

Figure 46. *In situ* flexing test and applications of the *Lego-like* flexible 3D block battery. a) Voltage decay of the unstressed non block cell, the non block cell, and the 3D block cell during flexing test with flexing radius of ~25 mm and the speed of ~2 times min^{-1}. b) Discharge voltage profiles of the non block and 3d block cell during flexing cycles and the discharge process at a 0.1C rate. The inset shows voltage fluctuation of non block cell (blue line) during flexing cycles. and c) it powered the blue LEDs after 5000 flexing cycles with a flexing radius of 15 mm. d) Lighting up three white lighting-emitting diodes (LEDs) worn on the wrist. e-f) Voltage output of flexible 3D block battery under different flexing radius of 25, 15, 8 mm, flat conditions.

3.4 Summary

In conclusion, we designed and fabricated a *Lego-like* flexible 3D block battery by a simple additional pressing process. The 3D block architecture can significantly enhance the cycle stability in conjunction with voltage stability during *In-situ* flexing test under the harsh condition for the practical application. Additionally, the Lego-like 3D block battery can be produced by using cost-effective methods and conventional electrodes fabrication process. Moreover, the 3D patterned electrodes showed increased the contact area and the adhesion force between the electrode coating layer. The 3D block structure can significantly mitigate the stress concentration by distributing tension, resulting in stable adhesion of electrode coating layers after repetitive flexing. More importantly, the lego-like flexible 3D block battery demonstrated successful operation under various flexing conditions. This results show that the *Lego-like* 3D block battery is an ideal candidate as flexible energy storage systems for practical application in flexible devices.

Chapter 4

Outlook for flexible lithium-ion batteries

We have addressed the recent progress and challenges in the flexible LIBs for the practical application with respect to electrode materials and cell designs, and important parameters are systematically summarized in **Figure 47**. The issues about the electrode delamination and crack generation are key parameters to achieve stable electrochemical performance of flexible LIBs. In an effort to improve the electrode integrity, several approaches such as the modification of the active materials and current collectors have been proposed from the stage of the materials development. For example, the morphological changes of the active materials from the spherical shaped particle to the nano-sized and porous structures ensured the internal contact of the electrode materials during the flexing tests. Moreover, the modification of the conventional current collector exploiting the additional patterning process, polymer composite and conducting carbon allowed intact structure even after flexible tests, maintaining the high electrical conductivity of the current collector. Unfortunately, the limitations about the delamination between the current collector and electrode coating layer encourages the researchers to turn the spotlight into the free-standing electrode with an integrated structure. This structure could significantly decrease the electrode thickness, facilitating the ionic and electronic transport. In addition, the absence of the current collector completely prevented the delamination between the current collector and slurry, allowing unprecedented electrochemical performance. With respect to the cell structure, the cable-, node-type, and coplanar configuration have been reported for the flexible lithium-based batteries with bendable, foldable, or stretchable characteristics. These modifications of the cell structures based on conventional pouch/cylindrical cells could avoid additional considerations towards safety issue because the conventional active materials could be used.

However, the overlooked point is that these approaches such as the modification of the electrode materials or cell designs do not satisfy the requirements for the commercial viability in terms of the industrial upscaling and process time. For example, they require the change of manufacturing process such as the electrode fabrication, electrolyte injection and cell packaging. Moreover, complex synthetic processes for flexible nano-sized and porous electrode materials may require much longer synthetic time than the conventional electrode materials.

Furthermore, the battery safety during flexing test should be taken into account on the basis of the industrial electrode condition for the practical use of the flexible lithium-based batteries. The delamination and crack generation in the electrode during the flexing test give rise to the increase of contact resistance of the electrode materials, which could contribute to the formation of lithium plating

and lithium dendritic growth at the cracked site. More importantly, it should be emphasized that the metallic lithium depositions in the electrode eventually lead to the cell failure, which significantly deteriorates the battery safety. In this regard, it is of importance to mitigate the formation of dendritic lithium metal by exploiting proper electrode materials and cell structures that have commercial potential, maintaining the high energy density under industrial electrode manufacturing condition. Finally, on the basis of this review, we believe that in-depth understanding towards the current challenges of the flexible lithium-based batteries can provide further insight into the development of better flexible electronics.

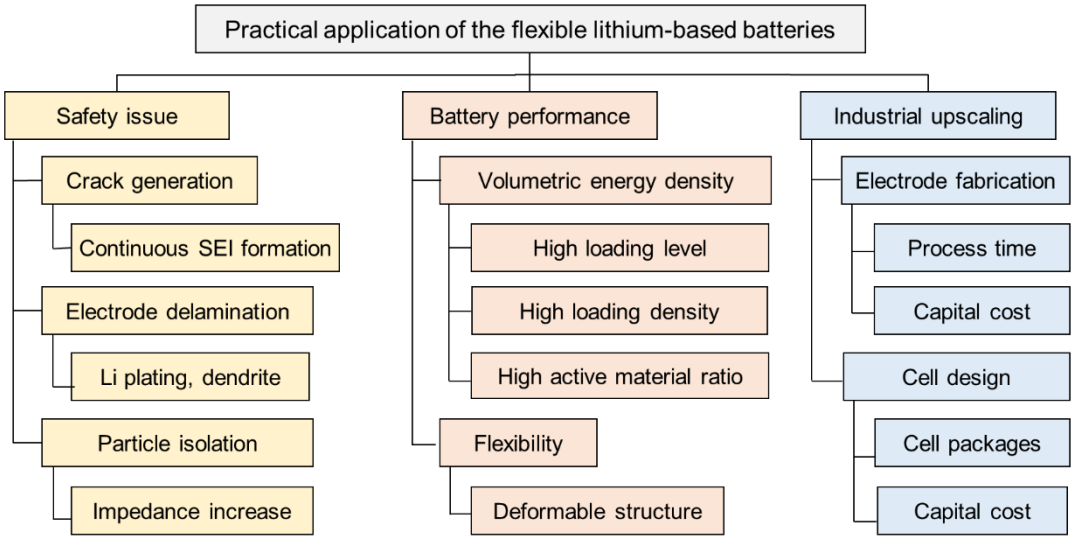

Figure 47. Requirements and considerations for practical application of flexible batteries.

References

1. Tarascon, J. M.; Armand, M., Issues and challenges facing rechargeable lithium batteries. *Nature* **2001,** *414* (6861), 359-67.

2. Dunn, B.; Kamath, H.; Tarascon, J.-M., Electrical Energy Storage for the Grid: A Battery of Choices. *Science* **2011,** *334* (6058), 928-935.

3. Roy, P.; Srivastava, S. K., Nanostructured anode materials for lithium ion batteries. *Journal of Materials Chemistry A* **2015,** *3* (6), 2454-2484.

4. Nishide, H.; Oyaizu, K., Toward flexible batteries. *Science* **2008,** *319* (5864), 737-738.

5. Li, L.; Wu, Z.; Yuan, S.; Zhang, X.-B., Advances and challenges for flexible energy storage and conversion devices and systems. *Energy & Environmental Science* **2014,** *7* (7), 2101-2122.

6. Stoppa, M.; Chiolerio, A., Wearable electronics and smart textiles: a critical review. *Sensors* **2014,** *14* (7), 11957-11992.

7. Armand, M.; Tarascon, J.-M., Building better batteries. *Nature* **2008,** *451* (7179), 652-657.

8. Choi, N. S.; Chen, Z.; Freunberger, S. A.; Ji, X.; Sun, Y. K.; Amine, K.; Yushin, G.; Nazar, L. F.; Cho, J.; Bruce, P. G., Challenges facing lithium batteries and electrical double-layer capacitors. *Angewandte Chemie International Edition* **2012,** *51* (40), 9994-10024.

9. Blake, A. J.; Kohlmeyer, R. R.; Drummy, L. F.; Gutiérrez-Kolar, J. S.; Carpena-Núñez, J.; Maruyama, B.; Shahbazian-Yassar, R.; Huang, H.; Durstock, M. F., Creasable Batteries: Understanding Failure Modes through Dynamic Electrochemical Mechanical Testing. *ACS applied materials & interfaces* **2016,** *8* (8), 5196-5204.

10. Huang, Q.; Wang, D.; Zheng, Z., Textile-Based Electrochemical Energy Storage Devices. *Advanced Energy Materials* **2016,** *6* (22), 1600783.

11. Fu, K. K.; Cheng, J.; Li, T.; Hu, L., Flexible batteries: from mechanics to devices. *ACS Energy Letters* **2016,** *1* (5), 1065-1079.

12. Wen, L.; Li, F.; Cheng, H. M., Carbon nanotubes and graphene for flexible electrochemical energy storage: from materials to devices. *Advanced Materials* **2016,** *28* (22), 4306-4337.

13. Xiao, H.; Pender, J. P.; Meece-Rayle, M. A.; de Souza, J. P.; Klavetter, K. C.; Ha, H.; Lin, J.; Heller, A.; Ellison, C. J.; Mullins, C. B., Reduced-Graphene Oxide/Poly (acrylic acid) Aerogels as a Three-Dimensional Replacement for Metal-Foil Current Collectors in Lithium-Ion Batteries. *ACS Applied Materials & Interfaces* **2017,** *9* (27), 22641-22651.

14. Lee, H.; Yoo, J. K.; Park, J. H.; Kim, J. H.; Kang, K.; Jung, Y. S., A Stretchable Polymer–Carbon Nanotube Composite Electrode for Flexible Lithium-Ion Batteries: Porosity Engineering by Controlled Phase Separation. *Advanced Energy Materials* **2012,** *2* (8), 976-982.

15. Mo, R.; Rooney, D.; Sun, K.; Yang, H. Y., 3D nitrogen-doped graphene foam with encapsulated germanium/nitrogen-doped graphene yolk-shell nanoarchitecture for high-performance flexible Li-ion battery. *Nature communications* **2017,** *8*.

16. Jiang, T.; Bu, F.; Feng, X.; Shakir, I.; Hao, G.; Xu, Y., Porous Fe2O3 Nanoframeworks Encapsulated within Three-Dimensional Graphene as High-Performance Flexible Anode for Lithium-Ion Battery. *ACS nano* **2017,** *11* (5), 5140-5147.

17. Chu, S.; Zhong, Y.; Cai, R.; Zhang, Z.; Wei, S.; Shao, Z., Mesoporous and Nanostructured TiO2 layer with Ultra-High Loading on Nitrogen-Doped Carbon Foams as Flexible and Free-Standing Electrodes for Lithium-Ion Batteries. *Small* **2016,** *12* (48), 6724-6734.

18. Kim, J.-S.; Ko, D.; Yoo, D.-J.; Jung, D. S.; Yavuz, C. T.; Kim, N.-I.; Choi, I.-S.; Song, J. Y.; Choi, J. W., A half millimeter thick coplanar flexible battery with wireless recharging capability. *Nano letters* **2015,** *15* (4), 2350-2357.

19. Weng, W.; Sun, Q.; Zhang, Y.; Lin, H.; Ren, J.; Lu, X.; Wang, M.; Peng, H., Winding aligned carbon nanotube composite yarns into coaxial fiber full batteries with high performances. *Nano letters* **2014,** *14* (6), 3432-3438.

20. Kwon, Y. H.; Woo, S.-W.; Jung, H.-R.; Yu, H. K.; Kim, K.; Oh, B. H.; Ahn, S.; Lee, S.-Y.; Song, S.-W.; Cho, J.; Shin, H.-C.; Kim, J. Y., Cable-Type Flexible Lithium Ion Battery Based on Hollow Multi-Helix Electrodes. *Advanced Materials* **2012,** *24* (38), 5192-5197.

21. Lin, H.; Weng, W.; Ren, J.; Qiu, L.; Zhang, Z.; Chen, P.; Chen, X.; Deng, J.; Wang, Y.; Peng, H., Twisted Aligned Carbon Nanotube/Silicon Composite Fiber Anode for Flexible Wire-Shaped Lithium-Ion Battery. *Advanced Materials* **2014,** *26* (8), 1217-1222.

22. Park, M.; Cha, H.; Lee, Y.; Hong, J.; Kim, S. Y.; Cho, J., Postpatterned Electrodes for Flexible Node-Type Lithium-Ion Batteries. *Advanced Materials* **2017**, 1605773.

23. Gwon, H.; Hong, J.; Kim, H.; Seo, D.-H.; Jeon, S.; Kang, K., Recent progress on flexible lithium rechargeable batteries. *Energy & Environmental Science* **2014,** *7* (2), 538-551.

24. Hu, Y.; Sun, X., Flexible rechargeable lithium ion batteries: advances and challenges in materials and process technologies. *Journal of Materials Chemistry A* **2014,** *2* (28), 10712-10738.

25. Yousaf, M.; Shi, H. T. H.; Wang, Y.; Chen, Y.; Ma, Z.; Cao, A.; Naguib, H. E.; Han, R. P. S., Novel Pliable Electrodes for Flexible Electrochemical Energy Storage Devices: Recent Progress and Challenges. *Advanced Energy Materials* **2016,** *6* (17), 1600490.

26. Liu, J.; Song, K.; van Aken, P. A.; Maier, J.; Yu, Y., Self-supported Li4Ti5O12–C nanotube arrays as high-rate and long-life anode materials for flexible Li-ion batteries. *Nano letters* **2014,** *14* (5), 2597-2603.

27. Deng, Z.; Jiang, H.; Hu, Y.; Liu, Y.; Zhang, L.; Liu, H.; Li, C., 3D Ordered Macroporous

MoS2@ C Nanostructure for Flexible Li-Ion Batteries. *Advanced Materials* **2017,** *29* (10).

28. Wu, H.; Meng, Q.; Yang, Q.; Zhang, M.; Lu, K.; Wei, Z., Large-Area Polyimide/SWCNT Nanocable Cathode for Flexible Lithium-Ion Batteries. *Advanced Materials* **2015,** *27* (41), 6504-6510.

29. Jung, M. S.; Seo, J. H.; Moon, M. W.; Choi, J. W.; Joo, Y. C.; Choi, I. S., A Bendable Li-Ion Battery with a Nano-Hairy Electrode: Direct Integration Scheme on the Polymer Substrate. *Advanced Energy Materials* **2015,** *5* (1).

30. Sun, Y.; Wang, C.; Xue, Y.; Zhang, Q.; Mendes, R. G.; Chen, L.; Zhang, T.; Gemming, T.; Rümmeli, M. H.; Ai, X., Coral-inspired nanoengineering design for long-cycle and flexible lithium-ion battery anode. *ACS applied materials & interfaces* **2016,** *8* (14), 9185-9193.

31. Lui, G.; Li, G.; Wang, X.; Jiang, G.; Lin, E.; Fowler, M.; Yu, A.; Chen, Z., Flexible, three-dimensional ordered macroporous TiO 2 electrode with enhanced electrode–electrolyte interaction in high-power Li-ion batteries. *Nano Energy* **2016,** *24*, 72-77.

32. Ren, J.; Li, L.; Chen, C.; Chen, X.; Cai, Z.; Qiu, L.; Wang, Y.; Zhu, X.; Peng, H., Twisting Carbon Nanotube Fibers for Both Wire-Shaped Micro-Supercapacitor and Micro-Battery. *Advanced Materials* **2013,** *25* (8), 1155-1159.

33. Wu, H.; Yang, Q.; Meng, Q.; Ahmad, A.; Zhang, M.; Zhu, L.; Liu, Y.; Wei, Z., A polyimide derivative containing different carbonyl groups for flexible lithium ion batteries. *Journal of Materials Chemistry A* **2016,** *4* (6), 2115-2121.

34. Park, M.-H.; Noh, M.; Lee, S.; Ko, M.; Chae, S.; Sim, S.; Choi, S.; Kim, H.; Nam, H.; Park, S.; Cho, J., Flexible High-Energy Li-Ion Batteries with Fast-Charging Capability. *Nano Letters* **2014,** *14* (7), 4083-4089.

35. Li, C.; Shi, T.; Yoshitake, H.; Wang, H., A flexible high-energy lithium-ion battery with a carbon black-sandwiched Si anode. *Electrochimica Acta* **2017,** *225*, 11-18.

36. Chen, Y.; Fu, K.; Zhu, S.; Luo, W.; Wang, Y.; Li, Y.; Hitz, E.; Yao, Y.; Dai, J.; Wan, J.; Danner, V. A.; Li, T.; Hu, L., Reduced Graphene Oxide Films with Ultrahigh Conductivity as Li-Ion Battery Current Collectors. *Nano Letters* **2016,** *16* (6), 3616-3623.

37. Choi, S.; Kim, T. H.; Lee, J. I.; Kim, J.; Song, H. K.; Park, S., General Approach for High-Power Li-Ion Batteries: Multiscale Lithographic Patterning of Electrodes. *ChemSusChem* **2014,** *7* (12), 3483-3490.

38. Kim, S. W.; Yun, J. H.; Son, B.; Lee, Y. G.; Kim, K. M.; Lee, Y. M.; Cho, K. Y., Graphite/silicon hybrid electrodes using a 3D current collector for flexible batteries. *Advanced Materials* **2014,** *26* (19), 2977-2982.

39. Liu, W.; Chen, Z.; Zhou, G.; Sun, Y.; Lee, H. R.; Liu, C.; Yao, H.; Bao, Z.; Cui, Y., 3D Porous Sponge-Inspired Electrode for Stretchable Lithium-Ion Batteries. *Advanced Materials* **2016,** *28* (18),

3578-3583.

40. Liu, J.; Zhou, W.; Lai, L.; Yang, H.; Lim, S. H.; Zhen, Y.; Yu, T.; Shen, Z.; Lin, J., Three dimensionals α-Fe 2 O 3/polypyrrole (Ppy) nanoarray as anode for micro lithium ion batteries. *Nano Energy* **2013,** *2* (5), 726-732.

41. Wang, K.; Wu, H.; Meng, Y.; Wei, Z., Conducting polymer nanowire arrays for high performance supercapacitors. *Small* **2014,** *10* (1), 14-31.

42. Chen, Z.; To, J. W.; Wang, C.; Lu, Z.; Liu, N.; Chortos, A.; Pan, L.; Wei, F.; Cui, Y.; Bao, Z., A Three-Dimensionally Interconnected Carbon Nanotube–Conducting Polymer Hydrogel Network for High-Performance Flexible Battery Electrodes. *Advanced Energy Materials* **2014,** *4* (12).

43. Cao, S.; Feng, X.; Song, Y.; Xue, X.; Liu, H.; Miao, M.; Fang, J.; Shi, L., Integrated fast assembly of free-standing lithium titanate/carbon nanotube/cellulose nanofiber hybrid network film as flexible paper-electrode for lithium-ion batteries. *ACS applied materials & interfaces* **2015,** *7* (20), 10695-10701.

44. Rao, J.; Liu, N.; Li, L.; Su, J.; Long, F.; Zou, Z.; Gao, Y., A high performance wire-shaped flexible lithium-ion battery based on silicon nanoparticles within polypyrrole/twisted carbon fibers. *RSC Advances* **2017,** *7* (43), 26601-26607.

45. Yehezkel, S.; Auinat, M.; Sezin, N.; Starosvetsky, D.; Ein-Eli, Y., Bundled and densified carbon nanotubes (CNT) fabrics as flexible ultra-light weight Li-ion battery anode current collectors. *Journal of Power Sources* **2016,** *312*, 109-115.

46. Fu, K.; Yildiz, O.; Bhanushali, H.; Wang, Y.; Stano, K.; Xue, L.; Zhang, X.; Bradford, P. D., Aligned carbon nanotube-silicon sheets: A novel nano-architecture for flexible lithium ion battery electrodes. *Advanced Materials* **2013,** *25* (36), 5109-5114.

47. Ahmad, S.; Copic, D.; George, C.; De Volder, M., Hierarchical Assemblies of Carbon Nanotubes for Ultraflexible Li-Ion Batteries. *Advanced Materials* **2016,** *28* (31), 6705-6710.

48. Wang, T.; Li, H.; Shi, S.; Liu, T.; Yang, G.; Chao, Y.; Yin, F., 2D Film of Carbon Nanofibers Elastically Astricted MnO Microparticles: A Flexible Binder-Free Anode for Highly Reversible Lithium Ion Storage. *Small* **2017,** *13* (20).

49. Wang, X.; Li, G.; Seo, M. H.; Lui, G.; Hassan, F. M.; Feng, K.; Xiao, X.; Chen, Z., Carbon-Coated Silicon Nanowires on Carbon Fabric as Self-Supported Electrodes for Flexible Lithium-Ion Batteries. *ACS applied materials & interfaces* **2017,** *9* (11), 9551-9558.

50. Tjandra, R.; Li, G.; Wang, X.; Yan, J.; Li, M.; Yu, A., Flexible high performance lithium ion battery electrode based on a free-standing TiO2 nanocrystals/carbon cloth composite. *RSC Advances* **2016,** *6* (42), 35479-35485.

51. Gao, Z.; Song, N.; Zhang, Y.; Li, X., Cotton-textile-enabled, flexible lithium-ion batteries with

enhanced capacity and extended lifespan. *Nano letters* **2015,** *15* (12), 8194-8203.

52. Zhang, H.; Jing, S.; Hu, Y.; Jiang, H.; Li, C., A flexible freestanding Si/rGO hybrid film anode for stable Li-ion batteries. *Journal of Power Sources* **2016,** *307*, 214-219.

53. Song, Z.; Ma, T.; Tang, R.; Cheng, Q.; Wang, X.; Krishnaraju, D.; Panat, R.; Chan, C. K.; Yu, H.; Jiang, H., Origami lithium-ion batteries. *Nature Communications* **2014,** *5*, 3140.

54. Balogun, M.-S.; Qiu, W.; Lyu, F.; Luo, Y.; Meng, H.; Li, J.; Mai, W.; Mai, L.; Tong, Y., All-flexible lithium ion battery based on thermally-etched porous carbon cloth anode and cathode. *Nano Energy* **2016,** *26*, 446-455.

55. Wang, K.; Luo, S.; Wu, Y.; He, X.; Zhao, F.; Wang, J.; Jiang, K.; Fan, S., Super-aligned carbon nanotube films as current collectors for lightweight and flexible lithium ion batteries. *Advanced Functional Materials* **2013,** *23* (7), 846-853.

56. Wang, Z.; Xu, C.; Tammela, P.; Huo, J.; Strømme, M.; Edström, K.; Gustafsson, T.; Nyholm, L., Flexible freestanding Cladophora nanocellulose paper based Si anodes for lithium-ion batteries. *Journal of Materials Chemistry A* **2015,** *3* (27), 14109-14115.

57. Wang, J.-G.; Jin, D.; Zhou, R.; Li, X.; Liu, X.-r.; Shen, C.; Xie, K.; Li, B.; Kang, F.; Wei, B., Highly flexible graphene/Mn3O4 nanocomposite membrane as advanced anodes for Li-ion batteries. *ACS nano* **2016,** *10* (6), 6227-6234.

58. Kim, S.-H.; Choi, K.-H.; Cho, S.-J.; Choi, S.; Park, S.; Lee, S.-Y., Printable Solid-State Lithium-Ion Batteries: A New Route toward Shape-Conformable Power Sources with Aesthetic Versatility for Flexible Electronics. *Nano Letters* **2015,** *15* (8), 5168-5177.

59. Hu, L.; Wu, H.; La Mantia, F.; Yang, Y.; Cui, Y., Thin, Flexible Secondary Li-Ion Paper Batteries. *ACS Nano* **2010,** *4* (10), 5843-5848.

60. Guo, J.; Zhu, H.; Sun, Y.; Tang, L.; Zhang, X., Flexible foams of graphene entrapped SnO 2– Co 3 O 4 nanocubes with remarkably large and fast lithium storage. *Journal of Materials Chemistry A* **2016,** *4* (41), 16101-16107.

61. Cho, S. J.; Choi, K. H.; Yoo, J. T.; Kim, J. H.; Lee, Y. H.; Chun, S. J.; Park, S. B.; Choi, D. H.; Wu, Q.; Lee, S. Y., Hetero-Nanonet Rechargeable Paper Batteries: Toward Ultrahigh Energy Density and Origami Foldability. *Advanced Functional Materials* **2015,** *25* (38), 6029-6040.

62. Li, M.; Pan, F.; Choo, E. S. G.; Lv, Y.; Chen, Y.; Xue, J., Designed construction of a graphene and iron oxide freestanding electrode with enhanced flexible energy-storage performance. *ACS applied materials & interfaces* **2016,** *8* (11), 6972-6981.

63. Kong, D.; Li, X.; Zhang, Y.; Hai, X.; Wang, B.; Qiu, X.; Song, Q.; Yang, Q.-H.; Zhi, L., Encapsulating V2O5 into carbon nanotubes enables the synthesis of flexible high-performance lithium ion batteries. *Energy & Environmental Science* **2016,** *9* (3), 906-911.

64. Xia, L.; Wang, S.; Liu, G.; Ding, L.; Li, D.; Wang, H.; Qiao, S., Flexible SnO2/N-Doped Carbon Nanofiber Films as Integrated Electrodes for Lithium-Ion Batteries with Superior Rate Capacity and Long Cycle Life. *Small* **2016,** *12* (7), 853-859.

65. Ma, Y.; Younesi, R.; Pan, R.; Liu, C.; Zhu, J.; Wei, B.; Edström, K., Constraining Si Particles within Graphene Foam Monolith: Interfacial Modification for High-Performance Li+ Storage and Flexible Integrated Configuration. *Advanced Functional Materials* **2016,** *26* (37), 6797-6806.

66. Gaikwad, A. M.; Arias, A. C.; Steingart, D. A., Recent Progress on Printed Flexible Batteries: Mechanical Challenges, Printing Technologies, and Future Prospects. *Energy Technology* **2015,** *3* (4), 305-328.

67. Milroy, C. A.; Jang, S.; Fujimori, T.; Dodabalapur, A.; Manthiram, A., Inkjet-Printed Lithium–Sulfur Microcathodes for All-Printed, Integrated Nanomanufacturing. *Small* **2017,** *13* (11).

68. El Baradai, O.; Beneventi, D.; Alloin, F.; Bongiovanni, R.; Bruas-Reverdy, N.; Bultel, Y.; Chaussy, D., Microfibrillated cellulose based ink for eco-sustainable screen printed flexible electrodes in lithium ion batteries. *Journal of Materials Science & Technology* **2016,** *32* (6), 566-572.

69. Kang, K.-Y.; Lee, Y.-G.; Shin, D. O.; Kim, J.-C.; Kim, K. M., Performance improvements of pouch-type flexible thin-film lithium-ion batteries by modifying sequential screen-printing process. *Electrochimica Acta* **2014,** *138*, 294-301.

70. Singh, N.; Galande, C.; Miranda, A.; Mathkar, A.; Gao, W.; Reddy, A. L. M.; Vlad, A.; Ajayan, P. M., Paintable Battery. *Scientific Reports* **2012,** *2*, 481.

71. Koo, M.; Park, K.-I.; Lee, S. H.; Suh, M.; Jeon, D. Y.; Choi, J. W.; Kang, K.; Lee, K. J., Bendable Inorganic Thin-Film Battery for Fully Flexible Electronic Systems. *Nano Letters* **2012,** *12* (9), 4810-4816.

72. Zhang, Y.; Bai, W.; Cheng, X.; Ren, J.; Weng, W.; Chen, P.; Fang, X.; Zhang, Z.; Peng, H., Flexible and stretchable lithium-ion batteries and supercapacitors based on electrically conducting carbon nanotube fiber springs. *Angewandte Chemie International Edition* **2014,** *53* (52), 14564-14568.

73. Ren, J.; Zhang, Y.; Bai, W.; Chen, X.; Zhang, Z.; Fang, X.; Weng, W.; Wang, Y.; Peng, H., Elastic and wearable wire-shaped lithium-ion battery with high electrochemical performance. *Angewandte Chemie* **2014,** *126* (30), 7998-8003.

74. Xu, S.; Zhang, Y.; Cho, J.; Lee, J.; Huang, X.; Jia, L.; Fan, J. A.; Su, Y.; Su, J.; Zhang, H., Stretchable batteries with self-similar serpentine interconnects and integrated wireless recharging systems. *Nature communications* **2013,** *4*, ncomms2553.

75. Song, Z.; Wang, X.; Lv, C.; An, Y.; Liang, M.; Ma, T.; He, D.; Zheng, Y.-J.; Huang, S.-Q.; Yu, H.; Jiang, H., Kirigami-based stretchable lithium-ion batteries. **2015,** *5*, 10988.

76. Blake, A. J.; Kohlmeyer, R. R.; Drummy, L. F.; Gutiérrez-Kolar, J. S.; Carpena-Núñez, J.;

Maruyama, B.; Shahbazian-Yassar, R.; Huang, H.; Durstock, M. F., Creasable Batteries: Understanding Failure Modes through Dynamic Electrochemical Mechanical Testing. *ACS Applied Materials & Interfaces* **2016,** *8* (8), 5196-5204.

77. Ostfeld, A. E.; Gaikwad, A. M.; Khan, Y.; Arias, A. C., High-performance flexible energy storage and harvesting system for wearable electronics. *Scientific Reports* **2016,** *6*, 26122.

78. Gaikwad, A. M.; Arias, A. C., Understanding the Effects of Electrode Formulation on the Mechanical Strength of Composite Electrodes for Flexible Batteries. *ACS Applied Materials and Interfaces* **2017,** *9* (7), 6390-6400.

79. Yang, H.; Bang, H.; Amine, K.; Prakash, J., Investigations of the exothermic reactions of natural graphite anode for Li-ion batteries during thermal runaway. *Journal of the Electrochemical Society* **2005,** *152* (1), A73-A79.

80. Gaikwad, A. M.; Khau, B. V.; Davies, G.; Hertzberg, B.; Steingart, D. A.; Arias, A. C., A High Areal Capacity Flexible Lithium-Ion Battery with a Strain-Compliant Design. *Advanced Energy Materials* **2015,** *5* (3), 1401389.

81. Zhou, G.; Li, F.; Cheng, H.-M., Progress in flexible lithium batteries and future prospects. *Energy & Environmental Science* **2014,** *7* (4), 1307-1338.

82. Wang, X.; Jiang, K.; Shen, G., Flexible fiber energy storage and integrated devices: recent progress and perspectives. *Materials Today* **2015,** *18* (5), 265-272.

83. Vlad, A.; Singh, N.; Galande, C.; Ajayan, P. M., Design Considerations for Unconventional Electrochemical Energy Storage Architectures. *Advanced Energy Materials* **2015,** *5* (19), 1402115.

84. Fang, X.; Shen, C.; Ge, M.; Rong, J.; Liu, Y.; Zhang, A.; Wei, F.; Zhou, C., High-power lithium ion batteries based on flexible and light-weight cathode of LiNi0.5Mn1.5O4/carbon nanotube film. *Nano Energy* **2015,** *12* (Supplement C), 43-51.

85. Zhu, J.; Chen, L.; Xu, Z.; Lu, B., Electrospinning preparation of ultra-long aligned nanofibers thin films for high performance fully flexible lithium-ion batteries. *Nano Energy* **2015,** *12* (Supplement C), 339-346.

86. Pushparaj, V. L.; Shaijumon, M. M.; Kumar, A.; Murugesan, S.; Ci, L.; Vajtai, R.; Linhardt, R. J.; Nalamasu, O.; Ajayan, P. M., Flexible energy storage devices based on nanocomposite paper. *Proceedings of the National Academy of Sciences* **2007,** *104* (34), 13574-13577.

87. Raccichini, R.; Varzi, A.; Passerini, S.; Scrosati, B., The role of graphene for electrochemical energy storage. *Nat Mater* **2015,** *14* (3), 271-279.

88. Li, N.; Chen, Z.; Ren, W.; Li, F.; Cheng, H.-M., Flexible graphene-based lithium ion batteries with ultrafast charge and discharge rates. *Proceedings of the National Academy of Sciences* **2012,** *109* (43), 17360-17365.

89. Hu, L.; Choi, J. W.; Yang, Y.; Jeong, S.; La Mantia, F.; Cui, L.-F.; Cui, Y., Highly conductive paper for energy-storage devices. *Proceedings of the National Academy of Sciences* **2009,** *106* (51), 21490-21494.

90. Liu, B.; Zhang, J.; Wang, X.; Chen, G.; Chen, D.; Zhou, C.; Shen, G., Hierarchical Three-Dimensional ZnCo2O4 Nanowire Arrays/Carbon Cloth Anodes for a Novel Class of High-Performance Flexible Lithium-Ion Batteries. *Nano Letters* **2012,** *12* (6), 3005-3011.

91. Cheng, Q.; Song, Z.; Ma, T.; Smith, B. B.; Tang, R.; Yu, H.; Jiang, H.; Chan, C. K., Folding Paper-Based Lithium-Ion Batteries for Higher Areal Energy Densities. *Nano Letters* **2013,** *13* (10), 4969-4974.

92. Choi, S.; Lee, J.-I.; Park, S., Patterning of electrodes for mechanically robust and bendable lithium-ion batteries. *Journal of Materials Chemistry* **2012,** *22* (42), 22366-22369.

93. Weng, W.; Sun, Q.; Zhang, Y.; He, S.; Wu, Q.; Deng, J.; Fang, X.; Guan, G.; Ren, J.; Peng, H., A Gum-Like Lithium-Ion Battery Based on a Novel Arched Structure. *Advanced Materials* **2015,** *27* (8), 1363-1369.

94. Kim, J.-S.; Lee, Y.-H.; Lee, I.; Kim, T.-S.; Ryou, M.-H.; Choi, J. W., Large area multi-stacked lithium-ion batteries for flexible and rollable applications. *Journal of Materials Chemistry A* **2014,** *2* (28), 10862-10868.

95. Liu, X.; Jung, H.-G.; Kim, S.-O.; Choi, H.-S.; Lee, S.; Moon, J. H.; Lee, J. K., Silicon/copper dome-patterned electrodes for high-performance hybrid supercapacitors. *Scientific Reports* **2013,** *3*, 3183.

96. Chen, Y. H.; Wang, C. W.; Zhang, X.; Sastry, A. M., Porous cathode optimization for lithium cells: Ionic and electronic conductivity, capacity, and selection of materials. *Journal of Power Sources* **2010,** *195* (9), 2851-2862.

97. Orikasa, Y.; Gogyo, Y.; Yamashige, H.; Katayama, M.; Chen, K.; Mori, T.; Yamamoto, K.; Masese, T.; Inada, Y.; Ohta, T.; Siroma, Z.; Kato, S.; Kinoshita, H.; Arai, H.; Ogumi, Z.; Uchimoto, Y., Ionic Conduction in Lithium Ion Battery Composite Electrode Governs Cross-sectional Reaction Distribution. *Scientific Reports* **2016,** *6*, 26382.

98. Wen, L.; Li, F.; Cheng, H.-M., Carbon Nanotubes and Graphene for Flexible Electrochemical Energy Storage: from Materials to Devices. *Advanced Materials* **2016,** *28* (22), 4306-4337.

99. Cannarella, J.; Arnold, C. B., Stress evolution and capacity fade in constrained lithium-ion pouch cells. *Journal of Power Sources* **2014,** *245* (Supplement C), 745-751.

100. Wang, X.-L.; An, K.; Cai, L.; Feng, Z.; Nagler, S. E.; Daniel, C.; Rhodes, K. J.; Stoica, A. D.; Skorpenske, H. D.; Liang, C., Visualizing the chemistry and structure dynamics in lithium-ion batteries by in-situ neutron diffraction. *Scientific reports* **2012,** *2*, 747.

101. Barai, A.; Guo, Y.; McGordon, A.; Jennings, P. In *A study of the effects of external pressure on the electrical performance of a lithium-ion pouch cell*, Connected Vehicles and Expo (ICCVE), 2013 International Conference on, IEEE: 2013; pp 295-299.

102. Liu, D.; Wang, Y.; Xie, Y.; He, L.; Chen, J.; Wu, K.; Xu, R.; Gao, Y., On the stress characteristics of graphite anode in commercial pouch lithium-ion battery. *Journal of Power Sources* **2013,** *232*, 29-33.